

ABSTRACT

Title of Dissertation: MECHANICAL ADAPTABILITY OF
 OVARIAN CANCER TUMOR SPHEROIDS

 Christina Barber Conrad, Doctor of Philosophy,
 2021

Dissertation directed by: Associate Professor, Giuliano Scarcelli, Ph.D.
 Fischell Department of Bioengineering

A major obstacle in ovarian cancer treatment is the onset of ascites, an abnormal build-up of fluid in the peritoneal cavity. Using in vitro perfusion models, ascitic flow has been shown to drive epithelial-mesenchymal-transition (EMT) biomarker expression, promote epidermal growth factor receptor (EGFR) downstream signaling, and upregulate chemoresistance. Given the close ties between cell mechanics and behaviors, it is of interest to establish if mechanotransduction serves a role in cell signaling dysfunction. Here, we identified the mechanical behavior of tumor spheroids subjected to flow using Brillouin confocal microscopy, a non-contact optical method based on the interaction between incident light and microscopic mechanical waves within matter. We validated this technique by establishing a relationship with the traditionally derived Young's modulus measured using atomic force microscopy and a parallel-plate compression device. Following characterization, we used Brillouin confocal microscopy to map mechanical properties of tumor spheroids embedded in a

microfluidic chip and found that continuous flow for 7 days caused a decreased Brillouin shift (i.e., stiffness) compared to tumors in a static condition.

Another physical phenomenon related to ascites is dysregulated osmolality. Maintaining cell water homeostasis is driven by the transport of water to balance solute concentration and can have direct consequences on mechanics and biochemical signaling in cells. Recently, it was demonstrated in single cells that cell volume correlated with mechanical properties; but the effects in tumor spheroids which exhibit multi-cellular interfaces has remained unclear. Here, we derived relationships between osmolality and nuclear volume, tumor cell density, and Young's modulus, and found the correlations in spheroids resembled single cell relationships previously described in literature. Additionally, we looked at the impact of osmotic shocks on E-cadherin junctions and found aggregates formed with a unique timescale compared to morphology. Lastly, we observed reversibility of the mechanical, morphological, and molecular properties which showed the tumor's dynamic ability to respond to physical cues. Altogether, this work demonstrated how flow and osmosis associated with ovarian cancer ascites can trigger phenotype transformations. These findings warrant future investigations into how the regulation of mechanotransduction pathways can be harnessed to prevent chemoresistance and signaling dysfunction.

MECHANICAL ADAPTABILITY OF OVARIAN CANCER TUMOR
SPHEROIDS

by

Christina Barber Conrad

Dissertation submitted to the Faculty of the Graduate School of the
University of Maryland, College Park, in partial fulfillment
of the requirements for the degree of
Doctor of Philosophy
2021

Advisory Committee:

Professor Giuliano Scarcelli, Chair

Professor Imran Rizvi

Professor William J. Polacheck

Professor Kimberly M. Stroka

Professor Huang Chiao Huang

Professor Peter Kofinas, Dean's Representative

© Copyright by
Christina Barber Conrad
2021

Acknowledgements

First to my advisor, Dr. Giuliano Scarcelli, thank you for making research enjoyable, helping me pivot when research (and life) went a different direction in 2020, and always having an open-door/Zoom policy. Thank you for helping me design a PhD project I was passionate about, keeping me on track, and motivating me when I needed it. Additionally, thank you for providing a fun atmosphere at lab meetings with funny stories and debates, letting me travel to Europe twice to attend my favorite Goodbye Flat Biology conference (among others), and supporting my extensive outside-research involvement in UMD organizations!

To my committee members, Dr. Imran Rizvi, Dr. Bill Polacheck, Dr. Kim Stroka, Dr. Joe Huang, and Dr. Peter Kofinas thank you for your support, time, and feedback throughout this process. I especially thank Dr. Imran Rizvi for establishing the basis of this project 4 years ago and introducing me to ovarian cancer biology. I also want to thank Dr. Kim Stroka and former graduate student, Dr. Kelsey Goodfriend (Gray) for their efforts in collaborating with me in my first publication.

To the faculty/staff of our department of bioengineering, I am especially grateful to have had the privilege to work in a friendly and supportive environment. I particularly thank all the support of student interests and the Bioengineering Graduate Student Society (BGSS). I wish to thank Dr. Helim Aranda-Espinoza and Dr. John Fisher for helping me out on countless occasions throughout my PhD and always showing their support. I also want to acknowledge all the staff members who keep the department running, from orders, to helping with holiday/retreat events, to sending us reminders to make sure we are on track to graduate, thank you!

To my current and past lab-mates, Jitao, Eitan, Giulia, Hongyuan, Tony, Milos, Josh, Maggie, Romanus, Raymundo, Justin, Jake, ChenChen, Tom, Angelina, thank you for helping me with research, providing me feedback, and being good friends. I have greatly enjoyed the insightful conversations and the laughter. I would especially like to thank my cohort classmate Josh for constantly being a source of guidance and being one step ahead, so I could follow in your footsteps!

To my UMD graduate school friends and colleagues, I am thankful for the last years of friendships and camaraderie. To my original cohort, thank you for being there for study/tutor sessions and helping me during the early years. I especially wish to thank all the graduate students who have served with me on committees like BGSS, for their efforts in creating social events, academic trainings, mentoring programs, etc. The UMD experience would have certainly not been the same without this!

Finally, some personal acknowledgements:

To two of my best friends, Alex and Meghan, thank you for always being a phone-call-away and being amazing, strong, driven, women in my life I can confide in. Thank you for the motivational check-ins and being a part of my journey!

Finally, a huge thank you to my family for always supporting me, providing motivational messages/calls, and making me laugh! Thank you to the best siblings ever, Jackie, Jeff, and Juleanne for leading the way and setting an example from the start. Thank you for always being there when I need it and just being your silly selves. Thank you to JohnPaul, Larissa, and Brian being the best sibling-in-laws I could ask for,

making holiday breaks and celebrations fun, and being great friends. And thank you to Carson and J.J. for being cute nephews and the most entertaining distraction during my PhD! Finally, thank you to my Mom and Dad, for inspiring me to be curious from an early age, raising me to be a problem-solver, teaching me to always try my best, and encouraging me to keep a balanced lifestyle. I certainly would not be at this stage without your advice over the last 27 years! Thank you all!!

Table of Contents

Acknowledgements.....	ii
Table of Contents	v
List of Tables	vii
List of Figures	viii
Chapter 1 : Overview of Thesis	1
Chapter 2 : Background	5
2.1 Ovarian Cancer Disease Progression	5
2.2 Implications of Ascites on Ovarian Cancer Progression	8
2.3 Cell Mechanics Overview.....	10
2.4 Water Volume Regulation	12
2.5 Methods to Characterize Mechanical Properties of Cells and Tissues	14
2.5.1 Overview of Technologies.....	14
2.5.2 Brillouin Confocal Microscopy	15
2.5.3 Atomic Force Microscopy	18
Chapter 3 : Characterization of Ovarian Cancer Tumor Spheroids using Brillouin Confocal Microscopy	20
3.1 Background.....	20
3.2 Methods.....	21
3.2.1 Cell Culture.....	21
3.2.2 Culture of 3D Spheroids	21
3.2.3 Brillouin Confocal Microscopy	22
3.2.2 Young’s Modulus using Atomic Force Microscopy.....	23
3.2.3 Young’s Modulus using MicroTester	24
3.2.2 Osmotic and Carboplatin Treatments	26
3.2.3 Statistical Analysis.....	27
3.3 Results.....	27
3.3.1 Mechanical Mapping of Spheroids using Brillouin Confocal Microscopy	27
3.3.2 Penetration Depth of Brillouin Confocal Microscopy for Tumor Spheroid Analysis.....	28
3.3.3 Mechanical Behavior of Tumor Spheroids Assessed using Brillouin Confocal Microscopy	30
3.3.4 Correlation of Mechanical Behavior of Tumor Spheroids with Atomic Force Microscopy and MicroTester.....	31
3.3.5 Effect of Carboplatin on Brillouin Shift	34
3.4 Discussion	35
Chapter 4 : Mechanical Properties of Tumor Spheroids under Shear Flow	40
4.1 Background.....	40
4.2 Methods.....	44
4.2.1 Cell Culture.....	44
4.2.2 Perfusion Chamber.....	45
4.2.3 Brillouin Confocal Microscopy	46
4.2.4 Statistical Analysis.....	47
4.3 Results.....	48
4.3.1 Spheroids Decrease Brillouin shift under Flow	48

4.3.2 Effects of Frequency of Medium Change on Osmolality and Growth of Tumor Spheroids.....	50
4.3.3 Brillouin Shift Corresponds to Medium Osmolality, but not Cumulatively	52
4.3.4 Nutrient Supply does not Affect the Brillouin Shift	54
4.4. Discussion	55
Chapter 5 : Water Transport Regulates Nucleus Volume, Cell Density, and Young’s Modulus in Tumor Spheroids	60
5.1 Background	60
5.2.1 Cell Culture.....	61
5.2.2 Spheroid Formation	62
5.2.3 Polyacrylamide Gels	62
5.2.4 Transfer of Spheroids.....	63
5.2.5 Osmotic Shock.....	63
5.2.6 Cell Volume Imaging and Analysis.....	64
5.2.7 Cell Density Imaging and Analysis	64
5.2.8 Atomic Force Microscopy	64
5.2.9 E-cadherin Staining Assay.....	65
5.2.10 Statistical Analysis.....	66
5.3 Results.....	66
5.3.1 Measuring Nuclear Volume in Tumor Spheroids	66
5.3.2 Link Between Osmolality and Young’s Modulus	69
5.3.4 Tumor Spheroids can Recovery Volume, Density, Young’s Modulus after Osmotic Shocks	71
5.3.5 Effect of Osmotic Shock on E-cadherin Expression.....	72
5.4 Discussion	77
Chapter 6 : Conclusion and Future Directions.....	81
6.1 Mechanical Effects due to Flow and Osmosis.....	81
6.2 A Potential Link Between Mechanics and Chemoresistance	83
6.3 Improvements in Modeling the Tumor Microenvironment	85
6.4 Technology development.....	86
Chapter 7 : Scientific Contributions	88
7.1 Publications.....	88
7.2 Presentations	89
Bibliography	93

List of Tables

Table 2.1 Summary of in vitro studies modeling flow	10
Table 2.2 Mechanical receptors	12
Table 3.1 Summary of techniques and culture method, duration, conditions, and number of samples for mechanical analysis	25
Table 3.2 Relationship between osmolality and sucrose concentration in PBS measured by an osmometer.....	26
Table 3.3 Results summary for mechanical testing of spheroids under varying sucrose concentrations	33
Table 5.1 Summary of percent difference from respective osmotic control.....	79

List of Figures

Figure 2.1 Brillouin confocal microscopy set-up	16
Figure 2.2 Brillouin spectrum and Brillouin map	17
Figure 3.1 Brillouin imaging of tumor spheroids	28
Figure 3.2 Signal penetration depth of tumor spheroids using Brillouin confocal microscopy	30
Figure 3.3 Osmotic shock effect on Brillouin shift of tumor spheroids	31
Figure 3.4 Effect of osmotic shock on Young's modulus	32
Figure 3.5 Relationship between Young's modulus and longitudinal modulus	33
Figure 3.6 Brillouin shift of spheroids treated with carboplatin	35
Figure 4.1 Brillouin confocal microscopy setup integrated with microfluidic chip ...	46
Figure 4.2 Static vs. flow Brillouin shift.....	49
Figure 4.3 Osmolality of medium with varying change frequencies over 7 days	51
Figure 4.4 Effect of medium change frequency on spheroid size.....	51
Figure 4.5 Cumulative effect of osmolality on Brillouin Shift.....	53
Figure 4.6 Effect of nutrients on spheroid growth and Brillouin shift.....	54
Figure 5.1 Relationship between osmolality and nucleus volume.....	68
Figure 5.2 Effect of osmotic shock on tumor cell density	69
Figure 5.3 Osmolality and Young's Modulus.....	70
Figure 5.4 Correlation between nucleus volume and Young's Modulus.....	71
Figure 5.5 Nuclear volume, density, and Young's modulus after recovery	72
Figure 5.6 E-cadherin experiment design and control	74
Figure 5.7 E-cadherin expression after 5 minutes of osmotic shock	75
Figure 5.8 E-cadherin expression after 30 minutes of osmotic shocks.....	76
Figure 5.9 E-cadherin aggregate size analysis	77
Figure 6.1 Molecular changes due to flow.....	84
Figure 6.2 Increased chemoresistance under flow	85

Chapter 1 : Overview of Thesis

Cells respond to physical cues using mechanotransduction, a process that converts mechanical inputs into biological outputs. [1–3] Specifically in cancer, cells are exposed to a variety of solid and fluid stresses in the tumor microenvironment, such as tension, compression, shear, osmotic, and fluid shear stress. [4] To understand the effects of these behaviors on cells, the tumor microenvironment has been recapitulated using in vitro models, which provide the ability to control specific mechanical and biochemical cues. [5] Moreover, these platforms can be adapted for mechanical analysis, microscopy, or a variety of biological assays to characterize cell phenotypes. Initial mechanobiology experiments were performed in 2-dimensional (2D) culture systems, but it is now recognized that cells have distinct behaviors when cultured in 3-dimensions (3D) due to biophysical interactions with the extracellular matrix, neighboring cells, and fluid. **The scope of this project is to identify how physical cues can impact mechanical behaviors in 3D culture systems.**

This dissertation focuses on the mechanical effects related to ovarian cancer ascites. Ascites refers to the abnormal accumulation of fluid in the peritoneal cavity caused by tumors obstructing lymphatic drainage and increased vasculature permeability. Studying this phenomena is critical as it is associated with a poor patient prognosis and resistance to chemotherapy. [6–9] Two mechanical factors inflicted by ascites are fluid flow and osmosis. Flow facilitates the dissemination of malignant tumors throughout the abdomen and imposes shear stress at the cellular level. Recently, using a microfluidic platform it was shown that flow mimicking ascites caused upregulated chemoresistance compared to a static condition. [9] In addition, ascites are

associated with an osmotic imbalance known as hyponatremia, a decreased serum sodium level that occurs as a result of the failure to excrete water. [10] Understanding the mechanical consequences of tumors under flow and in osmotically disturbed environments can inform the development of novel therapeutic strategies to target cancer cell mechanical pathways. **Thus, the overarching goals of this dissertation are to: (1) understand the effects of flow on mechanical properties of tumor spheroids and (2) identify the morphological, mechanical, and molecular consequences of water volume regulation in tumor spheroids.**

Chapter 2 provides background information on ovarian cancer, ascites, cell mechanics, cell volume regulation, and the mechanical analysis methods mainly used in this work, Brillouin confocal microscopy and atomic force microscopy (AFM). In **chapter 3**, we describe experiments performed to validate the ability of Brillouin confocal microscopy to assess the mechanical properties of 3D tumor spheroids by comparing to traditional techniques, including AFM and a parallel plate compression device (MicroTester). Ovarian cancer spheroids were cultured using two popular techniques: (1) an overlay method on Matrigel and (2) ultra-low attachment plates. To alter the mechanical state, spheroids were immersed in PBS with varying levels of sucrose to induce osmotic stress. Spheroid mechanical properties were measured by Brillouin confocal microscopy, AFM, and the MicroTester. Finally, spheroids were treated with carboplatin, a chemotherapeutic commonly used to manage ovarian cancer, to determine treatment-induced effects on tumor mechanical properties. Results indicated that Brillouin confocal microscopy allows mechanical analysis with a limited penetration depth of $\sim 92 \mu\text{m}$ for the Matrigel method and $\sim 54 \mu\text{m}$ for low attachment

method. Brillouin confocal microscopy metrics displayed the same trends as the corresponding “gold-standard” Young’s moduli measured with stress–strain methods when the osmolality of the medium was increased. Spheroids treated with carboplatin showed a decrease in Brillouin frequency shift. This characterization study provided confidence in using Brillouin confocal microscopy to analyze mechanics of 3D spheroids with micron-scale three-dimensional resolution.

In **chapter 4**, we applied Brillouin confocal microscopy to evaluate the mechanical modulation of tumor spheroids in response to flow. Here, we used a perfusion model to mimic ascites and exposed tumors to 7 days of flow with a shear stress of 3 dyne/cm². Our results indicated that ovarian cancer spheroids under flow had a significantly lower Brillouin shift compared to spheroids maintained in a static condition. We further dissected the role of distinct perturbations (e.g., shear flow, osmolality, nutrients) on tumor spheroid mechanical properties. The unique combination of a long-term microfluidic culture and noninvasive mechanical analysis technique provided insights on the effects of physical stress in ovarian cancer pathology.

In **chapter 5**, we sought to understand how osmoregulation impacted tumor morphology, mechanical properties, and cell-cell junctions. Previous work established relationships between osmolality, cell volume, and modulus in single cells; however, since tumors differ from single cells in that they possess multi-cellular interfaces, it was not obvious if they would behave similarly in response to osmotic shocks. Here, we subjected ovarian cancer tumor spheroids to hypotonic and hypertonic conditions using water and sucrose solutions and quantified nuclear volume, tumor cell density,

Young's modulus, and E-cadherin expression. Our analysis found that tumor spheroids did indeed behave in a similar manner to single cells with comparable power-law exponents for relationships previously established between osmolality, cell volume, and modulus. We found the proportion between the minimum nuclear volume and isotonic nuclear volume to differ from previous work, suggesting that the osmotically responsive water volume could be cell dependent or differ in 2D versus 3D environments. We also looked at the reversibility of mechanics and morphology after 5 minutes of osmotic shock and found spheroids had a robust ability to return to their original state. Finally, we quantified E-cadherin aggregates and observed a significant increase in aggregate size following 30 minutes of osmotic shock. Yet, these effects were not found just after 5 minutes, illustrating a temporal difference from mechanical and morphology properties. Interestingly, the osmotically induced cell adhesion changes which occurred at the 30-minute timepoint were reversible with isotonic medium. In a broader scope, this suggested that fluctuations in E-cadherin expression perceived to occur during cancer progression may be driven by physical stresses of the tumor microenvironment.

In **chapter 6**, we provide a conclusion of work, discussion of limitations, and future directions. Finally, **chapter 7** includes a list of publications and presentations resulting from this dissertation.

Chapter 2 : Background

2.1 Ovarian Cancer Disease Progression

Outcomes for advanced stage ovarian cancer continue to lag behind many other solid tumors with a 5-year survival rate of 49% and a 10-year survival rate of 31%. [11–15] For 2021, the American Cancer Society predicts approximately 21,410 women will receive a new diagnosis and 13,770 women will die from ovarian cancer. [15] A late-stage diagnosis, development of chemotherapy resistance, and on-set of ascites play a role in the high mortality rates associated with this disease. The typical progression of ovarian cancer is a multi-step process involving the (1) formation of tumors on the ovarian surface epithelium or in the fallopian tubes (2) outgrowth and expression of tumorigenic genes enabling the detachment of single cells or multi-cellular clusters (3) dissemination via transcoelomic routes (less common routes are hematogenous and lymphatic) and resistance to anoikis (4) implantation of metastases in the peritoneal cavity (5) spread of metastases to distant organs, most frequently the liver (57%), as well as the lung (38%), bone (4%), and brain (1%). [16–20]

Ovarian cancer tumors are classified as epithelial or non-epithelial. Epithelial tumors account for approximately 90% [15,21] of ovarian cancer cases and have five known histological subtypes which differ in pathology, site of origin, and behavior. These types include high-grade serous (70%), endometrioid (10%), clear cell (10%), mucinous (3%), and low-grade serous (<5%). [22] Endometrioid, clear cell, mucinous, and low-grade serous are classified as type I tumors and thought to originate from benign extraovarian lesions on the ovary. [23,24] Contrary, high-grade serous ovarian carcinomas are considered type II tumors which are more lethal and likely originate

from secretory or progenitor cells of the fallopian tube. [23] Somatic mutations (mutations acquired during disease development) vary based on histological subtype. Type I tumors are associated with PIK3CA, PTEN, KRAS, and BRAF gene mutations while Type II tumors almost always manifest TP53 mutations and can additionally have RB1, FOXM1, and NOTCH3 gene mutations. [23,24]

Germline (inherited) mutations increase a woman's likeliness to develop ovarian cancer. The relevant genes identified thus far include BRCA1, BRCA2, BRIP1, RAD51C, RAD51D, MSH2, MLH1, PMS2, MSH6, PALB2 and BARD1. [25,26] In addition, several hereditary and lifestyle factors may play a role in ovarian cancer development such as (1) hormone levels, (2) age of menarche and menopause, (3) fertility/infertility, (4) lactation, (5) benign gynecologic conditions (e.g. endometriosis) and gynecologic surgery, (6) birth control use, (7) hormone replacement therapy use, (8) obesity, (9) diet and nutrition, (10) physical activity, (11) smoking, alcohol, and drug use, and (12) ethnicity/race. [21,22] A longstanding theory is that ovarian cancer is related to recurring trauma of the ovarian epithelium; therefore, decreasing ovulation is postulated to reduce the risk. [27] In support of this hypothesis, studies indicate lower incidence rates of ovarian cancer occur in women who take estrogen and progestin combined birth control to prevent ovulation as well as women who reach menopause earlier. [28,29]

Ovarian cancer is often referred to as a 'silent killer' because warning signs remain hidden until late stages. [30] Symptoms such as abdominal or pelvic bloating, pain, and a loss of appetite are non-specific and often assumed to be gastrointestinal issues. [31] The conventional diagnostic imaging methods to detect tumor masses are

transvaginal ultrasound or abdominal contrast-enhanced CT. In addition, the use of magnetic resonance imaging, or fluorodeoxyglucose-positron emission tomography have been explored. [32] Only two biomarkers for the detection of ovarian cancer exist which are Carbohydrate Antigen 125 (CA125) and Human Epididymis Protein 4 (HE4). [33,34] Still, these biomarker tests are not able to be stand-alone diagnostic methods because normal conditions like menstruation can also cause elevated levels.

The standard treatment of ovarian cancer is surgical debulking (*i.e.* destruction of tumor volume) followed by an intravenous platinum/taxane based chemotherapy regime, generally given once every 21 days for six cycles. [35] While the majority of patients receive some benefits from chemotherapy at the start, approximately 50–70% of patients undergo relapse and chemoresistance. [36] Patient responses are classified as: (1) platinum refractory: tumor progresses during first chemo-treatment (2) platinum resistant: recurrence within 6 months after completion of first-line treatment (3) partially sensitive: recurrence within 6–12 months (4) highly sensitive: recurrence after more than 12 months. [35]

The recent development of poly (ADP-ribose) polymerase (PARP) inhibitors has provided a more positive outlook for patients. PARP is a family of nuclear enzymes which act to repair DNA damage, thus inhibiting them can destroy cancer cells. [37] Four PARP inhibitors, niraparib (Zejula), olaparib (Lynparza), Rucaparib (Rubraca), and veliparib have shown to improve patient outcome and Zejula, Lynparza, and Rubraca are FDA approved. [38–41]

Another novel approach to treat ovarian cancer is the use of light-based therapies which can increase tumor specificity and overcome chemoresistance. [42–44]

For example, photodynamic therapy (PDT) involves dosing the patient with a photosensitizing (PS) agent and irradiating the tumor with a visible light source at a specific wavelength. Activation of the PS agent yields singlet oxygen production and causes the cells to produce intracellular reactive oxygen species (ROS) instigating cell apoptosis. [45,46] In a similar manner, photoimmunotherapy (PIT) harnesses the effect of ROS production to increase cell death; here, conjugation of monoclonal antibodies to the PS agents provides increase selectivity to the tumor. [43,45] Light-based therapies appear promising but continued investigations are needed regarding the safety, efficacy, and underlying mechanisms.

2.2 Implications of Ascites on Ovarian Cancer Progression

The space between the parietal and visceral layers of the peritoneum is normally lined with fluid to reduce friction between the abdominal wall and organs. In >90% of stage III and IV ovarian cancer cases, an abnormal build-up of ascitic fluid occurs as a result of increased capillary permeability and impaired lymphatic drainage due to tumor obstruction. [47–49] Ascites contain tumor cells along with a variety of non-tumor cells including fibroblasts, adipocytes, mesothelial, endothelial and inflammatory cells. [49] In addition, ascites comprise tumorigenic cytokines such as interleukin (IL)-6, IL-8 tumor necrosis factor (TNF), and vascular endothelial growth factor (VEGF). [49,50] Malignant ascites possess unique metabolic and protein signatures distinguishable from non-malignant cirrhosis ascites and serum; thus, malignant ascites has been viewed to be a promising candidate for patient-specific biomarker analysis. [51,52] To relieve the pain caused by abdominal pressure, patients will often have fluid drained repeatedly via paracentesis. [47] In addition, patients are often recommended to partake in a

decreased sodium diet to reduce water retention; however, recent studies suggest this could be a counterproductive approach since ascites is associated with hyponatremia, a low serum sodium level. [53] In fact, one study showed that patients abiding by a restricted sodium diet had higher levels of ascites compared to patients not restricting sodium. [54]

To model ascites in vitro, several groups have developed and/or applied microfluidic platforms to analyze the continuous perfusion of medium over tumor cultures (summarized in **table 2.1**). [9,14,55–57]. Most crucially, these studies suggest flow induces (1) cell phenotypic changes resembling an epithelial-mesenchymal-transition (EMT), (2) downregulation of focal adhesion complex proteins, and (3) chemoresistance. Specifically, an upregulation of epidermal growth factor receptor (EGFR) and vimentin with a decrease of E-cad, characteristic of EMT, has been observed. [14] EMT is historically related to the underlying reconfiguration of the cytoskeleton, elongated morphology, front/back polarity, and increased migration. [58] In cancer, EMT is suspected to be involved in metastasis and chemoresistance. [59] It was also shown that flow induced a downregulation of phospho-paxillin, phospho-focal adhesion kinase (FAK), and vinculin. [9] The focal adhesion complex acts to stabilize the cytoskeleton and a loss of FAK has been linked to a decrease in cell stiffness. [60] Furthermore, flow was found to induce chemoresistance to carboplatin which is potentially mediated by downstream activation of EGFR signaling members mitogen-activated protein kinase/extracellular signal-regulated kinase (MEK) and extracellular signal-regulated kinase (ERK). [60] Collectively, these results potentially link mechanical markers with chemoresistance, but the correlation remains elusive. To

further investigate this relationship, we sought to directly quantify tumor mechanics under flow.

Table 2.1 Summary of in vitro studies modeling flow

Reference	Major Findings
Rizvi <i>et al.</i> , 2013. [14]	<ul style="list-style-type: none"> ▪ Compared static and flow cultures using same protocol as chapter 4 (7 days, 3 dyne/cm²) ▪ Flow cultures resembled EMT ▪ Flow caused upregulated epidermal growth factor receptor (EGFR) expression and vimentin ▪ Flow caused downregulated E-cadherin protein expression
Ip <i>et al.</i> , 2016. [55]	<ul style="list-style-type: none"> ▪ Compared static with flow cultures (0.02 dyne/cm² for 24 hours) ▪ Stemness markers Oct-4, c-Kit (CD117), ATP-binding cassette G2 (ABCG2), and P-glycoprotein (P-gp) were upregulated under flow ▪ Tumors under flow acquired resistance to cisplatin and paclitaxel
Sun <i>et al.</i> , 2019. [57]	<ul style="list-style-type: none"> ▪ Compared static and flow cultures ▪ Flow cultures had increased IL-8 protein production under shear stress of 0.5 – 2.0 dyne/cm² ▪ IL-8 production increased up to 5 hours after shear stress was applied
Nath <i>et al.</i> , 2020. [9]	<ul style="list-style-type: none"> ▪ Compared static and flow cultures using same protocol as chapter 4 (7 days, 3 dyne/cm²) ▪ Flow caused increased Phosphorylated-ERK1/2 ▪ Flow caused decreased phospho-paxillin and phospho-FAK and vinculin ▪ Increased carboplatin resistance under flow
Martinez <i>et al.</i> , 2021. [61]	<ul style="list-style-type: none"> ▪ Oscillating tension, but not constant tension, caused cells to develop metastatic phenotype ▪ Oscillating tension compared to constant tension caused increased cell migration, with decreased E-cadherin and increased Snail expression ▪ Cells subjected to oscillating tension developed larger tumors when injected into mice

2.3 Cell Mechanics Overview

Mechanical properties have been involved in nearly all cellular functions, e.g., migration, proliferation, gene expression, differentiation, apoptosis, [62–64] and in

tissue-level behaviors, *e.g.* morphogenesis, angiogenesis [65,66]. In cancer biology, it is now recognized that cross-talk between cells and physical cues from the microenvironment play a role in progression and metastasis. [4] The mechanical properties of cells can be influenced by a multitude of surrounding factors, such as solid stress, architecture of the substrate, fluid shear stress, etc. [67] In this work, we focused on flow and osmosis given the relevance to ovarian cancer ascites. Ultimately, understanding mechanotransduction pathways involved in tumorigenesis could be used to develop novel cancer therapies to control cell behaviors. [68]

Cells resemble sponges in that they are made up of a fibrous mesh consisting of the cytoskeleton, organelles, and macromolecules which are immersed in cytosol fluid. [69,70] For this reason, cells are often modeled as poroelastic biphasic materials, where fluid redistribution in response to deformation is determined by the poroelastic diffusion constant, which is influenced by the elastic modulus of the solid matrix, pore size of the cytoskeleton meshwork, and viscosity of the cytosol. [70] Cells have also been described as being viscoelastic, implying a dependence on probe frequency. [71,72] Importantly, mechanical analysis techniques use a wide range of probe sizes and frequencies; thus, one of the major efforts in recent years has been to standardize the relationships between various mechanical analysis techniques. [71] Therefore, one aim of our work was to utilize techniques operating in different regimes.

Sensing of mechanical stress at the cell surface is accomplished by several types of receptors/channels as listed in **table 2.2**. The most well-characterized mechanoreceptor are integrins, which bind to proteins such as collagen, laminin, and fibronectin on the ECM. [73–77] Integrins recruit focal adhesion complexes which can

lead to restructuring of the cytoskeleton and downstream activation of signaling pathways involving proteins such as Rho-associated protein kinase (ROCK), RHO, YAP, and TAZ. [78,79]

Table 2.2 Mechanical receptors

Channel/Family	References
Aquaporins	[80]
Integrins	[81–83]
Mechanosensitive G-protein-coupled receptors (GPCRs)	[83]
Mechanosensitive ion channels (“stretch-activated”)	[81,83,84]
Osmosensitive calcium (Ca ²⁺) channel (OSCA)	[85–87]
PIEZOs	[85,88,89]
Transient receptor potential (TRP) channels	[83,85,90]

Mechanical triggers like fluid shear stress have been shown to activate receptors such as transient receptor potential (TRP) channels or PIEZOs which mediate Ca²⁺ signaling [91–93], or aquaporins, which facilitate water transport across the cell membrane. [80] However, more work is needed to understand if mechanical stress acts directly or indirectly on specific receptors.

2.4 Water Volume Regulation

Water volume regulation plays an important role in numerous cell processes including survival, migration, and proliferation. [94] Approximately 50 to 75% of the human body is composed of water, with 70 to 75% being stored in cells and the remaining volume in plasma and interstitial spaces. [95] Osmoregulation is the process the body uses to maintain a balance between solutes and water and is predominately carried out by the kidneys. On average, serum osmolality in humans is 286 mOsm/kg

H₂O, but fluctuates depending on water and nutrient intake. [96] For instance, in the case of dehydration, the concentration of electrolytes in the blood rises. High serum osmolality triggers the pituitary gland in the brain to release antidiuretic hormone (ADH), also called vasopressin. ADH binds to vasopressin V2 receptors (V2R) on the basolateral membrane of cells in the cortical and medullary collecting tubules of the kidneys. [97] A cascade of signaling events initiates phosphorylation of aquaporin channels which provides a pathway for water to reabsorb into the cells, and thus results in less urine production. [97] Contrary, when serum osmolality levels are low, ADH production is impeded, and urine is diluted with water.

All cells participate in osmoregulation which is achieved by the exchange of ions (*e.g.* Na⁺, K⁺ and Cl⁻), organic osmolytes (*e.g.* sugars, polyols, amino acids, methylamines, and urea), and water to maintain an equal amount of solutes on the inside and outside of cells. [98–101] Water transports in the direction towards the highest solute concentration to attain equilibrium. [95] The mobility of water across the lipid bilayer of the cell membrane is achieved by transmembrane diffusion through the lipid matrix and facilitated diffusion using aquaporins and other membrane proteins, such as glucose transporters. [95,102–104] Nuclear volume is also responsive to extracellular osmotic conditions; in this case, water volume is regulated by passive diffusion through nuclear pore complexes. [105,106] In response to unequilibrated osmotic states, cells undergo regulatory volume decrease (RVD) or regulatory volume increase (RVI). Specifically, swelling initiates RVD which activates K⁺ and Cl⁻ efflux, whereas cell shrinkage prompts RVI and triggers a net NaCl uptake via Na⁺/H⁺ exchange, Na⁺-K⁺-2Cl⁻ cotransport, and Na⁺ channels. [107–109] It is not clearly

understood how cell types differ in their efficiency and time to complete RVI and RVD under varying osmotic states.

Regulation of cell volume has been implicated in a variety of processes including, cell cycle, energy metabolism, DNA repair, migration, proliferation, and differentiation. [110–112] Specifically in cancer, water volume regulation is linked to behaviors such as metastasis, proliferation, and angiogenesis. [109,113,114] Research has demonstrated that aquaporin expression is altered in several cancer types including lung, breast, ovarian, and prostate. [110,114–116] Cancer can also coincide with conditions such as hyponatremia (<130 mEq/L serum sodium levels or <280 mOsm/kg H₂O serum osmolality) [10,117] or syndrome of inappropriate secretion of anti-diuretic hormone (SIADH), where the body retains excess fluid. Specifically, in ovarian cancer, hyponatremia can arise in the manifestation of ascites, where elevated fluid levels occur in the peritoneal cavity. [47] In fact, a previous study showed 52.1% of patients with malignant ascites were affected by hyponatremia. [118] Other pathologies such as diabetes, sick-cell anemia, and cirrhosis can also cause disruptions in osmotic balances. [119,120] For instance, hyperosmolar hyperglycemic syndrome (HHS) is a complication that occurs in severe diabetes mellitus, where serum osmolality rises over 320 mOsm/kg H₂O. [121]

2.5 Methods to Characterize Mechanical Properties of Cells and Tissues

2.5.1 Overview of Technologies

The major advancements in mechanobiology have been driven by the development of technologies to quantify mechanical properties of cells. The most popular techniques today include the optical stretcher [122], micropipette aspiration

[123], atomic force microscopy [124], traction force microscopy [125], particle-tracking micro rheology [126], magnetic twisting/pulling cytometry [127], and Brillouin confocal microscopy [128]. [129–133] In addition, mechanical properties of tissues have been measured using techniques such as ultrasound elastography, and magnetic resonance elastography which possess lower spatial resolution but larger depth penetration. [131] Here, we highlight the two techniques used in this work, Brillouin confocal microscopy and atomic force microscopy.

2.5.2 Brillouin Confocal Microscopy

Brillouin Light Scattering (BLS) is based on the interaction between light and acoustic phonons i.e., microscopic mechanical waves within matter. BLS originated nearly a century ago by physicists Léon Brillouin and Leonid Mandelstam. According to history, Leonid Mandelstam was the first to develop the theories behind photon-phonon scattering in 1918. Meanwhile, Léon Brillouin predicted light scattering based from thermal fluctuations and published this work in 1922. [134] Mandelstam later published work in 1926. [135] The name “Brillouin-Mandelstam” scattering is occasionally used, but most often, it is referred to as “Brillouin scattering”. In the last 15 years, transitioning from point-sampling spectroscopy to an imaging modality [136] has enabled numerous mechanobiology applications, including the study of plants [137,138], the cornea and other optical tissue [139–143], mouse embryo [144], zebrafish [145], bone [146], spheroids [147], cancer cell migration [148], and more.

In the Brillouin Confocal Microscopy set-up used in this dissertation (**Figure 2.1**), backwards scattered light was collected at 180° and coupled into the Brillouin

spectrometer comprised of two stages of VIPA etalons arranged in cross-axis configuration. [128,149,150] A single mode linearly-polarized continuous wave laser (Torus, Laser Quantum) with a wavelength of either 660 nm or 532 nm was directed into an inverted microscope (Olympus IX81) where light was focused into the sample using an objective lens. A program created in-house (LabVIEW) was used to provide control of translational stages (Prior), image acquisition (Andor), region of interest selection, scanning step size, and exposure time.

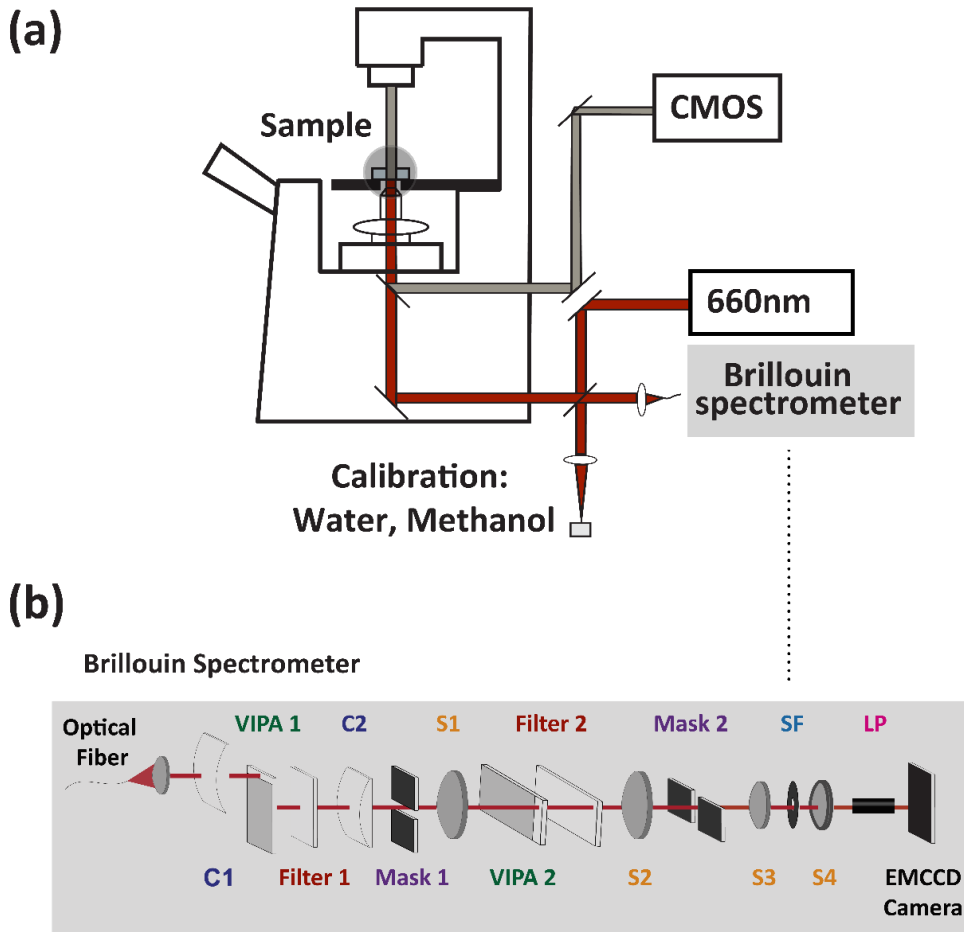


Figure 2.1 Brillouin confocal microscopy set-up

(a) Brillouin Confocal Microscope configuration. Light at 660 nm was focused onto the sample and back scattered light was collected by the same objective lens and directed to the Brillouin spectrometer. (b) Optical pathway of 2-stage VIPA Brillouin spectrometer. C1-2: cylindrical lenses; VIPA1-2: virtually imaged phased array; S1-4: spherical lenses; SF: spatial filter, LP: long-pass filter.

lens pair; Filter 1-2: linear variable neutral density filter; EMCCD: electron-multiplying charge-coupled device.

BLS is an inelastic process in which incident photons gain energy (anti-stokes) and lose energy (stokes). The shift in photon energy between incident and scattered light is the Brillouin frequency shift. **Figure 2.2** shows an example Brillouin spectrum composed of stokes and anti-stokes peaks. The free spectral range (FSR) i.e., wavelength separation between adjacent peaks and GHz per pixel i.e., factor to convert image pixels to frequency were determined by calibrating with water and methanol which have known Brillouin shifts (water: 7.46 at 532 nm and 6.01 GHz at 660 nm; methanol: 6.48 at 532 nm and 5.22 GHz at 660 nm). In this work, we reported the Brillouin frequency shift (GHz) displayed by a color bar where warmer colors (red) corresponded to an increased Brillouin frequency (and increased longitudinal modulus).

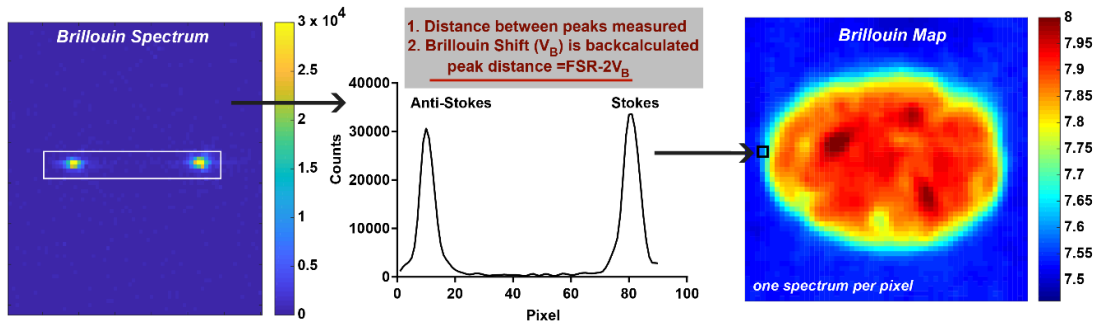


Figure 2.2 Brillouin spectrum and Brillouin map

(Left) Example of a Brillouin spectrum. Color bar represents intensity (Center) The anti-stokes and stokes correspond to the energy gained and loss, respectively, following the photon-phonon interaction. The distance between peaks is measured and the Brillouin shift is back calculated by knowing the free spectral range (determined during calibration). (Right) An example Brillouin map of a spheroid is shown where each pixel equates to one spectrum. The resolution of the Brillouin map is 1 $\mu\text{m}/\text{pixel}$. The color bar represents the Brillouin frequency shift, where a higher number/warmer color indicates a stiffer material. This measurement was acquired at 532 nm.

In a backscattering configuration, the Brillouin frequency shift (ν_B) is related to the longitudinal modulus (M') by:

$$M' = \frac{\rho \lambda^2 \nu_B^2}{4n^2}$$

Eq. 1

where ρ is the mass density, n is the refractive index, and λ is the incident wavelength. To estimate the error associated with the $\frac{\rho}{n^2}$ terms, we use prior literature which has approximated tumor mass densities to be between 1.024 g/cm³ and 1.046 g/cm³. Density and index of refraction are related by the Gladstone-Dale formula: [151]

$$n = n_{medium} + C * \alpha$$

where the n_{medium} and α terms can be approximated to be 1.33 and 0.00185 [152], respectively in medium, and C is the number of grams per 100 mL (102.4 and 104.6 grams in this case). Here, the estimated index of refraction of spheroids ranges between 1.519 and 1.524. Based on these estimates, the uncertainty associated with assuming a constant $\frac{\rho}{n^2}$ term is approximated to be 0.66%.

2.5.3 Atomic Force Microscopy

Atomic force microscopy is one of the most popular techniques used in mechanobiology experiments. A cantilever probes the surface by pressing at a preset indentation rate and distance. A laser beam is deflected on the cantilever tip and detected by a photodiode. Multiplying the cantilever spring constant by the cantilever deflection gives the force. Force verses displacement curves are then generated to extract mechanical information like Young's modulus. Probe selection is important to

define the spatial resolution and the information which is retrieved (e.g., cytoplasm vs. cortical stiffness in cells). For example, a sharp tip is useful for probing the cell surface, while a sphere/colloidal tip measures forces distributed throughout the cytoplasm. [153] In our work, we used a CP-qp-CONT-Au sphere colloidal probe (NanoAndMore USA Corp.) having a diameter of 3 - 5.5 μm and spring constant of 0.1 N/m according to the manufacturer. Force-displacement curves are most often analyzed using the Hertzian contact theory, which assumes the surface is frictionless, strains are small, and infinitesimal elastic deformation. [154] In this model, force and Young's modulus are related by equation:

$$F = \frac{4}{3} \cdot \frac{E}{1 - \nu^2} \cdot \sqrt{r} \cdot \delta^{\frac{3}{2}}$$

Eq. 2

with δ as the measured indentation of the sample, E is Young's modulus, ν is Poisson's ratio, and r is the probe radius. The Poisson's ratio for cells is generally estimated to be 0.5 which assumes the material to be perfectly incompressible and isotropic. [153] An important limitation to consider with this model, is that it does not account for the material's viscous components. [153]

Chapter 3 : Characterization of Ovarian Cancer Tumor Spheroids using Brillouin Confocal Microscopy

3.1 Background

It is widely accepted that cells sense and respond to mechanical cues in their microenvironment; however, the underlying causes of mechanical changes and the implications of altered mechanical properties in cancer progression remain areas of continued investigation. [4,76,163,164,155–162] A largely underestimated regulator of mechanical properties is osmotic pressure of the extracellular environment. On short time scales, i.e., immediately after adding the solute, changes in mechanical properties have been explained due to water efflux from cells and the resulting osmotic pressure gradient. [70,128,165,166] In single cells, several groups have explored the effects of hyperosmotic stress and have shown a positive correlation with Young's modulus. [70,128,165,166] Yet, single cells do not adequately portray disease pathology. For this reason, many groups have sought to fabricate 3D tumors, organoids, or biomaterials to reflect mechanical and biochemical components of the microenvironment and thus investigate how cells respond to various environmental stimuli. [4,14,158,164,167,168]

A major limitation of current technologies that measure the mechanical properties of biological samples is that they require contact with the sample and are severely limited in complex 3D matrix environments or other systems that do not offer direct access to cells. Therefore, a non-contact approach to extract the mechanical features of complex biological systems will be of value, particularly in cancer-related mechanobiology studies. One potential technology to address this need is Brillouin microscopy. Brillouin light scattering is a phenomenon where interaction of incident light with acoustic phonons within a material causes a frequency shift in the scattered

radiation. The Brillouin frequency shift is related to the longitudinal modulus of the sample, i.e., the ratio of stress-strain in a purely uniaxial setting at high-frequency (GHz). Thus, combining a high-resolution Brillouin spectrometer with confocal microscopy, will enable three-dimensional maps of material mechanics to be generated.

3.2 Methods

3.2.1 Cell Culture

Epithelial ovarian cancer cells (NIH: OVCAR5) were grown in standard conditions using the recommended culture medium containing RPMI 1640 Medium, no phenol red, 10% Fetal Bovine Serum (FBS), and 1% Pen Strep.

3.2.2 Culture of 3D Spheroids

Culture of Spheroids using Matrigel Overlay Method: Corning® Matrigel® (Growth Factor Reduced (GFR) Basement Membrane Matrix Phenol Red-Free, *LDEV-Free #356231) was used as the extracellular matrix for the cultures. Matrigel was thawed overnight on ice at 4 °C. The following day, 250 µL of thawed Matrigel was pipetted into wells of a sterile glass bottom 24-well plate (Greiner bio-one Sensoplate, #662892). Matrigel was polymerized by incubating at 37 °C for 20 minutes. 1 mL of 10^4 cells/mL OVCAR5 cells in medium supplemented with 2% Matrigel was added per well. Media was replaced every three days by gently aspirating old medium to not disturb spheroids attached to the Matrigel.

Culture of Spheroids using Low Attachment Plates: Corning™ 96 Well Ultra-Low Attachment Treated Spheroid Microplates (Fisher Scientific, #12-456-721) provided a method for growing larger spheroids without the need for Matrigel,

favorable for the MicroTester and AFM, where contact with the spheroid is required and the presence of Matrigel could skew the results. To prepare spheroids, 300 μL of OVCAR5 at a concentration of 10^5 cells/mL in OVCAR5 medium was added to 96 wells and incubated at 37 °C for 3 days. 12-mm glass coverslips coated in collagen were prepared to provide a surface for spheroid attachment: Glass coverslips were initially sterilized with 70% ethanol. A composition Rat Tail Type I Collagen High protein concentration (Corning™, #354249, protein concentration: 10.21 mg/mL) and 70% ethanol at a 1:4 ratio was prepared. 50 μL of the mix was added per coverslip and stored overnight at room temperature. On day 3 of spheroid growth, spheroids were removed from the 96-well plate by slowly pipetting with a 10 mL pipette tip and transferred to collagen coated coverslips. Spheroids were incubated in 37 °C for 24 hours to provide time to attach.

3.2.3 Brillouin Confocal Microscopy

For 3D imaging (**Figure 3.1**), we performed raster scanning in the XY dimension and refocused to a new location along the Z axis to generate another stacked image. For all other measurements (**Figures 3.2, 3.3, 3.4**), images were acquired in the central XZ plane perpendicular to the Matrigel bed. The spatial resolution of the images depends on the NA of the objective lens; here, the lateral resolution was 1 μm and axial resolution was 2 μm . A post-processing algorithm developed in MATLAB was used to fit the Brillouin peaks to a Lorentzian function and extrapolate the average Brillouin frequency shift. Average spheroid Brillouin frequency shift was determined by excluding the locations pertaining to the surrounding medium and averaging values corresponding to the remaining spheroid structure.

The mechanical response of spheroids cultured using Matrigel was tested under 3 osmotic conditions: 0, 500 mM, and 1000 mM sucrose. After 3 days of culture, 3 spheroids in 3 separate wells, for a total of 9 spheroids per condition were tested. Brillouin imaging was performed immediately after the addition of sucrose. Images were acquired in the XZ plane with 1 μm resolution. Due to the poor signal penetration depth in the z-direction for low attachment spheroids, we imaged 100 μm x 100 μm sections in the XY plane where the signal was resolvable with 2 μm resolution. Spheroids cultured using the low attachment plates were subjected to 0, 62.5 mM, and 125 mM sucrose. The decreased osmotic condition was required due to decrease signal intensity in the low attachment spheroids (**Figure 3.2c**). A total of 6 spheroids were measured per condition.

3.2.2 Young's Modulus using Atomic Force Microscopy

The Young's modulus was measured using an Asylum MFP-3D-BIO AFM with CP-qp-CONT-Au sphere colloidal probe (NanoAndMore USA Corp.) having a diameter of 3 - 5.5 μm according to the manufacturer. The spring constant of the cantilever was measured to be 0.17 N/m, which was within a factor of 1.69 to the manufacturer's nominal value of 0.1 N/m. AFM was performed using a 3 μm force distance, a 1 V trigger point (~8.7-8.8 nN), and a scan rate of 0.99 Hz. Force curves were fit to the Hertz model within Asylum's Igor Pro-based software, using the equation

$$F = \frac{4}{3} \cdot \frac{E}{1 - \nu^2} \cdot \sqrt{r} \cdot \delta^{\frac{3}{2}}$$

Eq. 3

with δ as the measured indentation of the sample and Young's modulus E as the fitting parameter. The Poisson's ratio ν of the sample was assumed to be 0.45 and the tip radius of curvature r was approximately 2.1 μm .

OVCAR5 tumor spheroids were cultured using the low attachment method and attached to collagen coated glass coverslips as previously described. Spheroids were placed in a Falcon® 50 mm x 9 mm Sterile Petri Dish (New Star Environmental and Laboratory Products #351006) and bathed in 4 mL of PBS with varying concentrations of sucrose (0, 500, and 1000 mM) warmed at 37 °C. Three 10 x 10 force maps spanning 2500 μm^2 (5 μm step size) were acquired per spheroid and 3 spheroids per sucrose level were tested.

3.2.3 Young's Modulus using MicroTester

Spheroids were prepared using the low attachment protocol previous described. Spheroids were placed in a fluid bath of PBS-sucrose solution warmed to 37 °C. A total of 35 spheroids were measured in varying sucrose conditions: 0, 250, 500, 750, and 1000 mM. A microbeam with a diameter of 152.4 μm , modulus 411,000 MPa, and length of 60 mm was fixed to a 2 mm x 2 mm compression plate and mounted to the vertical actuator. Data acquisition was performed using the software provided, SquisherJoy. Spheroids were compressed once in the Z-axis by ramping up to 75%, with a load time of 20 seconds, hold of 10 seconds, and recovery period of 20 seconds.

Data was exported to Microsoft Excel where analysis was performed. The Young's modulus was calculated as the slope of the stress strain curve using the formula:

$$E = \frac{F/A}{\Delta L/L}$$

Eq. 4

where E is the Young's modulus ($\mu\text{N}/\mu\text{m}^2$), F is the force in (μN), A is the surface area of the spheroid (μm^2), L is the height of the spheroid (μm), and ΔL is the displacement of the beam (μm). The surface area (A) was measured by assuming a circle as the shape of the surface. ImageJ was used to determine the diameter of the spheroid at 10% strain. [169] The length of the spheroid (L) was gathered by the SquisherJoy software, where cursors were placed prior to testing at the top and bottom of the spheroid. The Young's modulus was analyzed between 0 and 10% strain where initial strain (0%) was assumed to be when the applied force reached 0.1 μN . Culture methods for mechanical testing using Brillouin, AFM, and the MicroTester are summarized in **table 3.1**.

Table 3.1 Summary of techniques and culture method, duration, conditions, and number of samples for mechanical analysis

Methods Summary				
Technique	Culture Method	Culture duration (days)	Conditions (Sucrose Concentration mM)	Samples per condition
Brillouin	Matrigel	3	0, 500, 1000	9 spheroids
Brillouin	Low Attachment	4	0, 62.5, 125	6 spheroids
AFM	Low Attachment	4	0, 500, 1000	3 spheroids (3 regions of interest per spheroid)
MicroTester	Low Attachment	4	0, 250, 500, 750, 1000	8, 7, 7, 7, 6 spheroids respectively

3.2.2 Osmotic and Carboplatin Treatments

Osmotic Treatments: Concentrations of sucrose up to 1000 mM in Phosphate Buffered Saline (PBS, Dulbecco's phosphate-buffered saline, 1X) was added to the extracellular fluid of spheroids. A relationship between sucrose concentration and osmolality was established by measuring solutions with an Advanced® Micro-Osmometer Model 3300 (Table 3.2).

Table 3.2 Relationship between osmolality and sucrose concentration in PBS measured by an osmometer

Sucrose Concentration (mM)	Measured Osmolality (mOsm/kg H ₂ O)	
	Mean	Standard Deviation
0	285	4.58
250	546	5.69
500	847	1.53
750	1141	11.50
1000	1440	8.39

Carboplatin Treatments: OVCAR5 tumor spheroids were cultured for 7 days using the protocol for forming spheroids with Matrigel as previously described. Medium changes occurred on days 3 and 6 of culture. On day 7, spheroids were dosed with 500 μ M carboplatin in 1 mL of medium while non-treated groups were refreshed with 1 mL of medium. After 96 hours of incubation in 37 °C, the Brillouin shift of non-treated and treated cells were measured. To retrieve Brillouin shift of the spheroids, the extracellular medium was removed by thresholding values less than 7.65 GHz and the Brillouin shift was average across the remaining area of the spheroid. Experiments were performed using a previous set up which used a green laser ($\lambda = 532$ nm). Brillouin

shifts using a green laser ($\lambda = 532$ nm) is related to the Brillouin shifts using a red laser ($\lambda = 660$ nm) by multiplying by the ratio of wavelengths; Red Brillouin Shift = Green Brillouin Shift * (532/660). A total of 19 non-treated and 20 treated spheroids were measured in three separate rounds.

3.2.3 Statistical Analysis

For osmotic pressure experiments, a one-way ANOVA was used to compare groups. For the carboplatin treatment experiment, a paired t-test assuming equal variances was used to compare to the non-treatment group. All statistics were performed using GraphPad Prism7. * ≤ 0.05 ** ≤ 0.01 , *** ≤ 0.001 , **** ≤ 0.0001 .

3.3 Results

3.3.1 Mechanical Mapping of Spheroids using Brillouin Confocal Microscopy

A series of corresponding Brillouin XY cross-sectional images, taken at 12.5 μm step along the Z depth axis, are shown in **Figure 3.1a** and demonstrate the 3D sectioning capability provided by the confocal nature of Brillouin measurements. For the rest of the paper, to perform Brillouin imaging on a large population of spheroids, we scanned one depth-section (XZ plane) per spheroid; we chose the XZ plane cutting through the central axis of the spheroid, to maintain consistency in the assessed location across measurements. An example brightfield image in the XY plane of a spheroid cultured using the Matrigel method and corresponding Brillouin map in the XZ plane is shown in **Figure 3.1b**. High resolution Brillouin images revealed tumor spheroids to be a heterogenous conglomeration of cells. The subcellular sites with the highest Brillouin shifts are predicted to be nuclei, based on a previous analysis of single cells.

[149] Areas of Brillouin shifts as low as the liquid medium were observed within spheroids, probably indicating regions with no cells and no matrix.

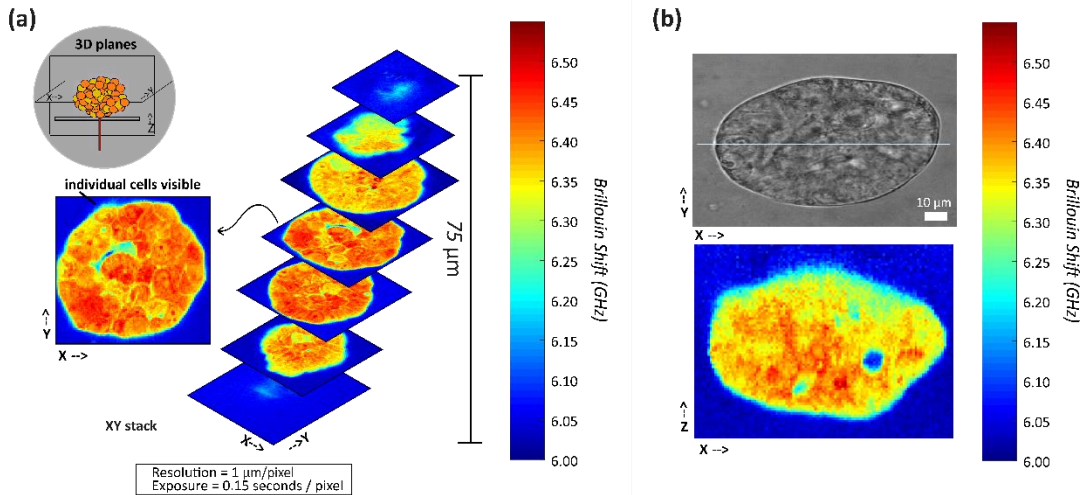


Figure 3.1 Brillouin imaging of tumor spheroids

(a) Images acquired in the XY plane of a tumor spheroid. Color bar represents the Brillouin shift in GHz, where an increased Brillouin shift is related to an increased longitudinal modulus. Images were acquired with a resolution of 1 μm per pixel and exposure of 0.15 seconds per pixel. (b) An example Brillouin map and brightfield image of a spheroid cultured using Matrigel measured in the XZ plane (perpendicular to the Matrigel surface).

3.3.2 Penetration Depth of Brillouin Confocal Microscopy for Tumor Spheroid

Analysis

As with any optical technique, the penetration depth achieved by Brillouin microscopy in non-transparent samples is limited. Here, we analyzed the signal intensity as a function of depth for spheroids on Matrigel and in low attachment cultures (**Figure 3.2**). We overlaid cells on Matrigel (**Figure 3.2a**) and in 96 Well Ultra-Low Attachment Treated Spheroid Microplates which resulted in the formation of spheroids in suspension, without an exogenous extracellular matrix (**Figure 3.2b**). [170] The sizes of spheroids cultured using both techniques depend on culture time and seeding density. Previous work has shown that OVCAR5 cells overlaid on Matrigel form

heterogeneous spheroids with a bimodal size distribution, which we observed as well. [171] Consistent with the culture duration for mechanical testing, we analyzed Matrigel spheroids on day 3 having a diameter of $\sim 50 \mu\text{m}$ and low attachment spheroids on day 4 with a diameter of $\sim 850 \mu\text{m}$. As expected, the signal intensity of light through scattered medium decreased exponentially. The relationship between signal intensity (I) and depth (z) is commonly written as $I = I_0 e^{-\beta z}$ where I_0 is the incident light intensity and β is the scattering coefficient. In **figure 3.2c.**, we show the natural log of the normalized intensity $\ln\left(\frac{I}{I_0}\right) = -\beta z$ and found the scattering coefficient β for low attachment spheroids to be significantly greater than Matrigel spheroids ($p \leq 0.0001$) (**Figure 3.2c**).

To approximate the maximal penetration depth for Brillouin signal analysis, we assumed that a minimum of 3000 counts of incident light intensity was required to retrieve the Brillouin shift. We quantified the intensity at varying penetration depths and predicted that spheroids grown using the Matrigel method up to a diameter in the Z direction of $\sim 92 \mu\text{m}$ could be measured. Low attachment spheroids had greater opacity compared to the Matrigel method, thus the penetration depth was reduced to $\sim 54 \mu\text{m}$. In both the Matrigel and low attachment spheroids, increasing extracellular osmolality using PBS with sucrose decreased the signal penetration depth. A penetration depth to enable Brillouin measurements was obtained for concentrations of sucrose of up to 1000 mM for Matrigel spheroids and up to 125 mM for low attachment spheroids.

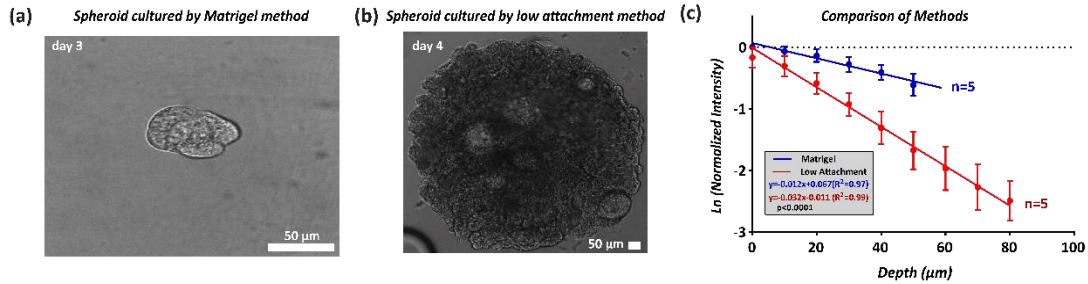


Figure 3.2 Signal penetration depth of tumor spheroids using Brillouin confocal microscopy

(a) Brightfield image (Objective: 60X) of a spheroid after 3 days of culture using the Matrigel method. (b) Brightfield image (Objective: 10X) of a spheroid after 4 days of culture using the low attachment method. (c) Depth in the z axis (μm) vs. natural log of normalized intensity for Matrigel and low attachment spheroids. A comparison of liner fits showed that the signal intensity in the low attachment method was significantly lower than the Matrigel method ($p \leq 0.0001$). A total N of 5 spheroids per condition were measured.

3.3.3 Mechanical Behavior of Tumor Spheroids Assessed using Brillouin Confocal Microscopy

To alter the mechanical properties of the spheroids, we immersed them in hyperosmotic solutions of PBS with up to 1000 mM of sucrose. We observed an increased Brillouin shift with increased osmolality of the solution in both Matrigel and low attachment spheroids (**Figure 3.3a, b**). The two methods, however, demonstrated similar trends in dependency between osmolality and Brillouin shift: **Figure 3.3c** overlays both **Figure 3.3a** and **Figure 3.3b** measurements and shows a linear relationship between osmolality and Brillouin shift, independent of the spheroid size and culture method.

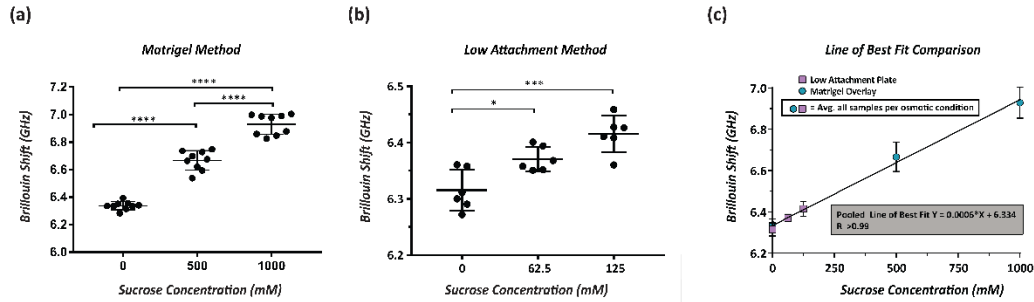


Figure 3.3 Osmotic shock effect on Brillouin shift of tumor spheroids

(a) Increased osmolality of extracellular solution for spheroids cultured using Matrigel method caused an increased spheroid Brillouin Shift. Data points represent the average Brillouin shift of a spheroid. A total $N = 9$ spheroids per condition were mapped. (b) Increased osmolality of spheroids cultured by low attachment method caused increased Brillouin shift. Due to stronger opacity in the low attachment method, a lower sucrose concentration was used compared to the Matrigel method. Data points represent the average Brillouin shift of a single spheroid. A total $N = 6$ spheroids per condition were mapped. (c) Brillouin shift was linearly related ($R^2 > 0.99$) to the osmolality of the PBS-sucrose solution, independent of culture method. Statistics to analyze significant differences between groups were performed using a one-way ANOVA, where $p \leq 0.05$ (*), $p \leq 0.01$ (**), $p \leq 0.001$ (***), $p \leq 0.0001$ (****).

3.3.4 Correlation of Mechanical Behavior of Tumor Spheroids with Atomic Force Microscopy and MicroTester

To validate the ability of Brillouin Confocal Microscopy to analyze the mechanical properties of tumor spheroids, we evaluated spheroids undergoing similar osmotic changes using two standard approaches to extrapolate Young's modulus based on deformation of the sample: Atomic Force Microscopy and Micro-Scale Mechanical Tester (MicroTester). For these experiments, the spheroids were cultured using the low attachment technique. Using AFM, (**Figure 3.4a**) we found an increase in Young's modulus with increased osmolality (**Figure 3.4b**). Similarly, using the MicroTester, (**Figure 3.4c**) we found that the Young's modulus increased with increasing osmolality. The Young's modulus at 0 to 10% strain was evaluated and an exponential relationship ($R^2=0.95$) was found between Young's modulus and increasing osmolality (**Figure 3.4d**). The averages and standard deviations for each condition are found in **table 3.3**.

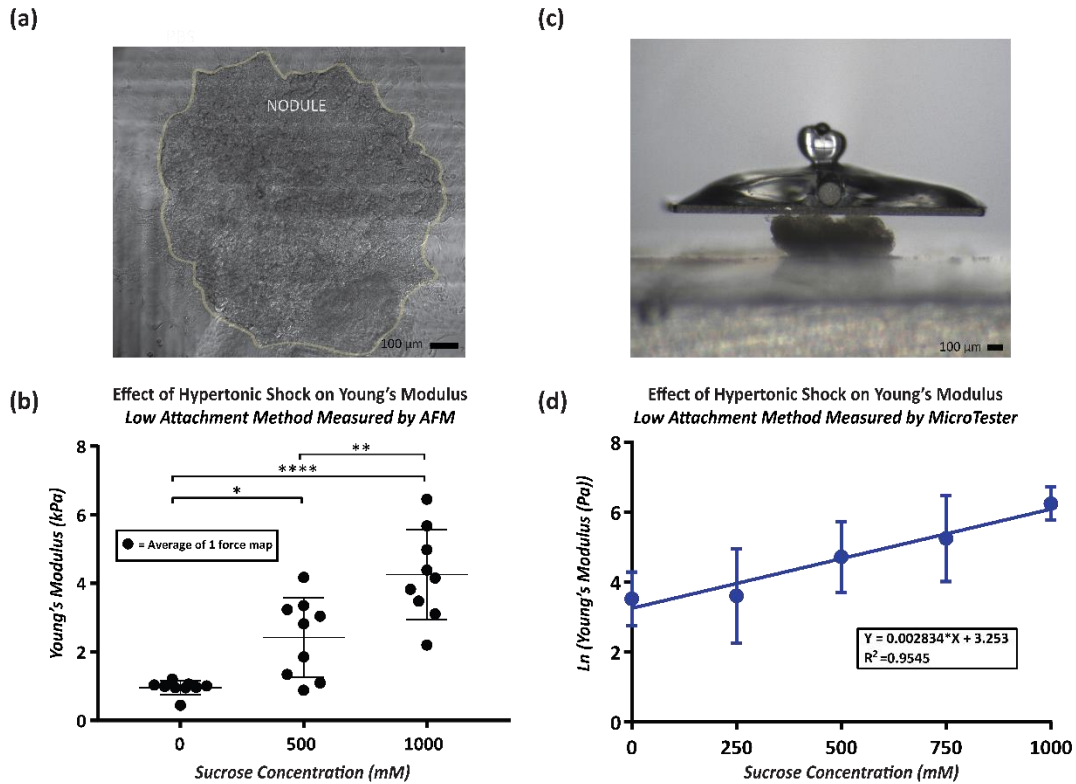


Figure 3.4 Effect of osmotic shock on Young's modulus

(a) Example of spheroid attached to a collagen coated glass coverslip measured using AFM. (b) Increased osmolality caused an increased Young's modulus measured by AFM. Each data point represents the average of one force map spanning an area of $2500 \mu\text{m}^2$ (10×10 pixels). Three spheroids were measured with three force maps per spheroid ($N = 9$ force maps) (c) Example of spheroid being contacted by MicroTester parallel compression plate. Statistics to analyze significant differences between groups were performed using a one-way ANOVA, where $p \leq 0.05$ (*), $p \leq 0.01$ (**), $p \leq 0.001$ (***), $p \leq 0.0001$ (****). (d) Increased osmolality exhibited an exponential relationship with Young's modulus measured by the MicroTester. A total $N = 8, 7, 7, 7, 6$ spheroids were acquired for 0, 250 mM, 500 mM, 750mM, and 1000 mM conditions, respectively

Table 3.3 Results summary for mechanical testing of spheroids under varying sucrose concentrations

Results Summary			
Technique	Culture Method	Sucrose (mM)	Mean \pm Standard Deviation
Brillouin	Matrigel	0	6.33 \pm 0.03 GHz
		500	6.67 \pm 0.07 GHz
		1000	6.93 \pm 0.07 GHz
Brillouin	Low Attachment	0	6.32 \pm 0.04 GHz
		62.5	6.37 \pm 0.02 GHz
		125	6.42 \pm 0.03 GHz
AFM	Low Attachment	0	0.96 \pm 0.18 kPa
		500	2.42 \pm 1.09 kPa
		1000	4.25 \pm 1.23 kPa
MicroTester	Low Attachment	0	42.32 \pm 26.69 Pa
		250	86.35 \pm 140.13 Pa
		500	168.47 \pm 156.81 Pa
		750	329.12 \pm 314.43 Pa
		1000	562.09 \pm 246.82 Pa

Using an approximation of 1.37 for the refractive index and 1.08 g/cm³ for density [128], we can estimate the longitudinal modulus and derive a relationship with the Young's modulus acquired using AFM (**figure 3.5**).

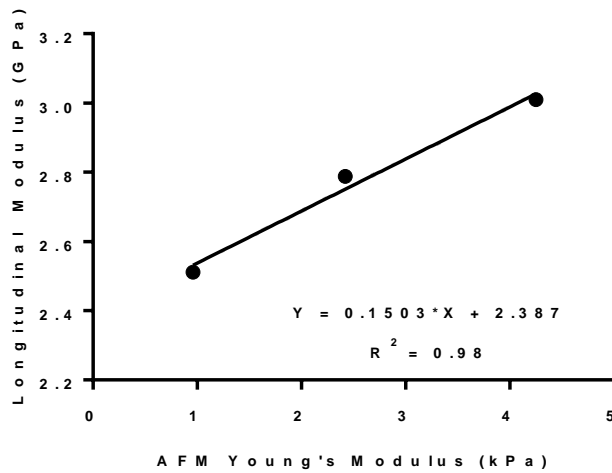


Figure 3.5 Relationship between Young's modulus and longitudinal modulus
Tumor spheroids were immersed in 0, 500 mM, or 1000 mM sucrose solutions. AFM Young's modulus was performed on spheroids fabricated using the low attachment method while Brillouin shift was acquired for nodules made using the Matrigel method. The longitudinal

modulus was calculated from the Brillouin shift using an approximation of 1.37 for the refractive index and 1.08 g/cm^3 for the density. Laser wavelength was 660 nm. Each data point represents the mean. Standard deviations and individual measurements are plotted in figures 3.3 and 3.4. For Young's modulus, three spheroids were measured with three force maps per spheroid ($N = 9$ force maps). For longitudinal modulus, a total $N = 9$ spheroids per condition were measured.

3.3.5 Effect of Carboplatin on Brillouin Shift

Finally, we evaluated the mechanical effect of carboplatin treatment on 3D tumor spheroids. Carboplatin is a commonly used anti-cancer chemotherapeutic to manage ovarian cancer. We acquired brightfield images in the XY plane and Brillouin maps in the XZ plane. Compared to no treatment controls, spheroids showed evidence of morphological changes after carboplatin treatment (**Figure 3.6a**). We also found carboplatin to cause a significant decrease in Brillouin shift ($p \leq 0.0001$) corresponding with a disrupted structure compared to the control group (**Figure 3.6b**). These results were consistent with previous literature showing HeLa cells undergoing a significant decrease in stiffness and damaged morphology following treatment with paclitaxel. [172] More recently, Margueritat *et al.* used Brillouin Confocal Microscopy to quantify tumor mechanics post chemotherapy and showed the tumor core had decreased drug efficacy. [173] Since OVCAR5 cells cultured on Matrigel form 3D spheroids with a bimodal size distribution,[171] the relationships between tumor size, treatment response and mechanical properties will be important to investigate in future studies. In addition, the possibility that drug resistant tumor cell populations have a decreased stiffness due to a more metastatic behavior should not be ruled out and would be an interesting experiment for the future.

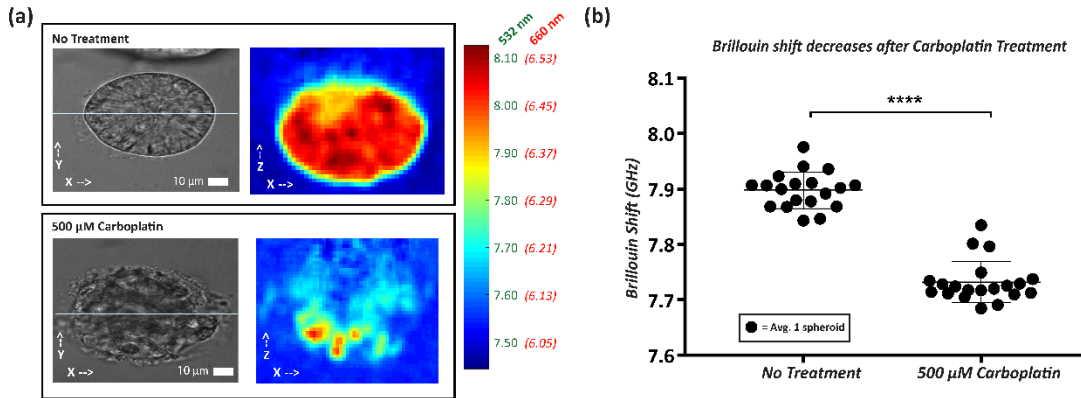


Figure 3.6 Brillouin shift of spheroids treated with carboplatin

(a) Brightfield images and corresponding Brillouin maps of no treatment and carboplatin treated spheroids. Color bar represents Brillouin shift (GHz) represented in both 660 nm and 532nm incident wavelengths. (b) Brillouin Shift of no treatment 500 μM carboplatin measured using Brillouin. A threshold of 7.65 GHz was used to isolate spheroids from surrounding medium. The Brillouin shift was significantly lower in the 500 μM carboplatin group compared to no treatment group (**** $p \leq 0.0001$). Each data point represents the average Brillouin shift per spheroid. A total of $N = 19$ control spheroids and $N = 20$ treated spheroids were measured. Statistics to analyze significant differences between groups were performed using a t-test.

3.4 Discussion

The mechanical properties of cells and extracellular components play critical roles in cell behaviors such as migration, differentiation, proliferation, and survival. [4,157,159,174,175] The need for technologies to quantify mechanical properties on a cellular level is widely recognized; thus, in the past two decades, tools including AFM, micropipette aspiration, optical stretchers, microfluidics, and microrheology have been developed. [129–133] Despite each of their strengths, analysis of 3D in vitro cultures, which are increasingly prevalent, requires destruction of the sample. AFM and micropipette aspiration both require direct contact with the sample, thus preventing the analysis of experiments involving spheroids encapsulated in 3D microenvironments or within microfluidic devices. [130,133] Both optical stretchers and microfluidic channels have enhanced the ability for high throughput mechanical analysis but they require deformation of the sample. [129,130,133] Microrheology is useful for assessing

the effects in 3D microenvironments; however, this technique is still invasive and involves tracing microparticles undergoing Brownian motion, so the data output typically involves trajectories of paths rather than mapping of the entire cell structure. [130,132]

Brillouin Confocal Microscopy is an all-optical method that can resolve mechanical information in 3D in vitro cultures without contact and with micron scale resolution. However, Brillouin does not provide information for traditional metrics such as Young's modulus. Thus, to align with gold standard technologies, we performed a validation to study the mechanical properties of ovarian cancer spheroids. We evaluated two different culture techniques since each showed benefits contingent on the mechanical analysis technology. We observed Brillouin to be advantageous compared to AFM and the MicroTester in measuring 3D tumor spheroids in overlay cultures on Matrigel. AFM analysis of spheroids cultured using Matrigel posed challenges due to the interference of the gel with the probe and forces felt beneath the spheroid caused by the low Young's modulus of Matrigel. To isolate adherent 3D spheroids from the underlying Matrigel matrix, centrifugation and enzymatic methods have been used, but these methods are highly disruptive to the spheroids. Culturing on Matrigel was also unfavorable for MicroTester analysis which requires samples to be greater than 50 μm and attached to a hard surface. Of the two culture techniques, we found the low attachment method to be better suited for AFM and the MicroTester. On the other hand, Brillouin had challenges in imaging spheroids generated by the protocol used here for low attachment cultures due to the large size and opacity of the spheroids. In the future, a lower initial seeding density could be used to form smaller spheroids

and ensure whole spheroid measurements with Brillouin. Consequentially, the low penetration depth of Brillouin signal may limit applications to cancer bio-mechanics studies. For instance, hypoxic cores are introduced in spheroids greater than 200 μm . [176] Whereas, our findings show the maximum penetration depth of Brillouin signal is $\sim 92 \mu\text{m}$ for Matrigel spheroids and $\sim 54 \mu\text{m}$ for low attachment spheroids. Additionally, extracting mechanical properties from real tissue specimens may better mimic the in vivo mechanical state due to the extracellular matrix and tumor cell heterogeneity. However, opacity and size of a biopsy sample may inhibit such measurements. Accordingly, until further advances are made in the Brillouin technology, experimental designs must be coordinated with the current specifications.

Both protocols appear to be uniquely advantageous; for example, Matrigel can vary batch-to-batch thus producing variable results; yet, depending on the cell line, the method yields a collection of heterogenous tumors in the same well, so mechanics in conjunction with migration and proliferation can be determined. [171] Finally, it is important to acknowledge the differences in sampling resolutions for each of the three systems used to assess the mechanical properties of the 3D tumor spheroids. Brillouin can create maps of the entire spheroid in three axes, although here we reduced the maps to one average value for comparison. AFM can generate a map with micron resolution as well, but only in one axis while the MicroTester only generates a single value per sample. Thus, the optimal technology choice is dependent on both culture technique and sampling interests.

As shown in this work, the mechanical measurements in 3D tumor spheroids performed by Brillouin microscopy correlate with the gold standard mechanical

measurements. Using AFM, we found that OVCAR5 spheroids had an average Young's modulus of 0.96 kPa in PBS. Because the tip of the AFM probe was approximately 5 μm , the Young's modulus of a spheroid was resolvable to the level of single cells. A similar range of Young's moduli have been previously reported for other ovarian cancer cell lines: OVCAR4: 1.120 kPa, HEY: 0.884 kPa, OVCAR3: 0.576 kPa, and HEYA8: 0.494 kPa. [174] In comparison, non-malignant immortalized ovarian surface epithelial cells had a Young's modulus of 2.472 kPa. [174] Using the MicroTester, we found that OVCAR5 spheroids had an average Young's modulus of 42.32 Pa in PBS and an exponential correlation was observed with increasing sucrose concentration. The Young's modulus of spheroids composed of mesenchymal stem cells was previously measured using the MicroTester and was found to be on a similar scale of 42.28 ± 6.14 Pa at 20% strain. [177]

In the present study, Brillouin shift evaluated optically, and Young's modulus determined by AFM and MicroTester, all increased with increasing osmolality. Previous reports measuring single cells subjected to hyperosmolar conditions provided similar results. [128,165,166] It is believed that increasing osmolality causes water efflux from cells, reduction of cell volume, and crowding of the intracellular space. In our experiments, a reduction in tumor volume was visible immediately following sucrose addition. [165,166] The relationship between cell volume and cell stiffness has spawned further questions on how cells regulate volume and behavioral consequences. Guo *et al.*, recently showed that changes in cell volume, due to either osmotic stress or matrix stiffness, influenced stem cell differentiation. [166] The consequences of cell volume changes in cancer cells is less understood but may be highly relevant in

tumorigenesis, where cancer cells experience a variety of external physical stresses. [164,178]

A critical next step is to identify Brillouin sensitivity to changes in cell stiffness due to different phenomena, such as solid/liquid fraction changes, variation in cell contractility, crowding of intracellular space, or cytoskeletal polymerization/crosslinking. Recent work revealed that at high water content (>95%), Brillouin measurements are strongly affected by water content compared to traditional mechanical testing systems to the point of practically being unable to characterize mechanical effects in highly hydrated gels. [179,180] However, in single cells and tissues, which have approximately ~70% water content, Brillouin shift and Young's modulus have both been shown to be sensitive to water content. [128,181] Thus, a strong correlation between Brillouin microscopy and traditional mechanical testing is generally observed and Brillouin technology appears to be sensitive to several relevant phenomena such as collagen crosslinking/branching, [140] chromatin decondensation [149] and activation/inhibition of actin polymerization. [128]

Chapter 4 : Mechanical Properties of Tumor Spheroids under Shear Flow

4.1 Background

A major cause of disease progression in patients with ovarian cancer is the accumulation of ascitic fluid within the abdomen. [55] Approximately 89% of patients with stage III or IV ovarian cancer develop ascites. [7,182] The cause of fluid retention is not well-established and thought in-part to be due to lymphatic obstruction. [7,183,184] Palliative care such as paracentesis via percutaneous drainage or catheter drainage is frequently used to reduce ascites; however, symptoms can reappear in as little as 10 days. [47,185,186] Not only does fluid accumulation raise intra-abdominal pressure [19] and cause discomfort to the patient, but ascites facilitates cell phenotypic modulations and intervenes with treatment success. The clinical presence of ascites is indicative of increased transcoelomic metastasis [19], resistance to chemotherapy [7], and upregulated markers associated with poor prognosis, such as vascular endothelial growth factor (VEGF). [183,185,187]

While increasing evidence supports the role of ascites as a negative prognostic indicator in advanced-stage ovarian cancer, the impact of mechanical stress (i.e., flow-induced shear stress) on aggressiveness, and poor sensitivity to treatment, in ovarian cancer remains understudied. Recent studies [11, 12] demonstrated an increase in epithelial to mesenchymal transition (EMT), marked by changes such as increased spindle-like morphology, loss of E-cadherin, and upregulated vimentin, in 3D OVCAR5 tumors grown under continuous flow for 7 days [14], compared to equivalent static cultures. A concomitant flow-induced increase in expression and activation of the epidermal growth factor receptor (EGFR) was observed. Elevated EGFR signaling

activity is understood to promote proliferation, invasiveness, and cell survival. [9] The experimental parameters used in this study informed the conditions used in the present study.

More recently, Nath *et al.* [12] demonstrated that flow-induced shear stress conferred resistance to carboplatin, compared to equivalent static cultures, despite higher drug uptake under flow. [12] This flow-induced resistance to carboplatin was associated with increased signaling of mitogen-activated protein kinase/extracellular signal-regulated kinase (MEK) and phosphorylated extracellular signal-regulated kinase (p-ERK). A variety of receptor tyrosine kinase (RTK) networks regulate MEK/ERK signaling, including the EGFR, which was confirmed to be upregulated under flow. [12] Interestingly, low-dose anti-EGFR photoimmunotherapy (PIT) resulted in comparable cytotoxic response in static and flow cultures, suggesting a role for targeted photochemistry-based therapies as part of rationally-designed combinations. [9]

Ip *et al.* [55] used the human ovarian carcinoma SKOV-3 cell line formed into spheroids and embedded them on a 2-hydroxyethylmethacrylate (poly-HEMA) coated glass slide. Exposing tumors to both 0.002 dyne/cm^2 and 0.02 dyne/cm^2 for 24 hours induced gene expressions corresponding to EMT characterized by increased Snail, Slug, and N-cadherin, with decreased E-cadherin. Upregulated stem cell marker gene expressions were also observed including octamer-binding transcription factor 4 (Oct-4), c-Kit (CD117), ATP-binding cassette G2 (ABCG2) and P-glycoprotein (P-gp). [55] Moreover, flow increased chemoresistance after treatment of cisplatin ($25 \mu\text{M}$) or paclitaxel (100 nM). [55]

While molecular consequences under flow are partially established, there remains inadequate information on how exposure to flow modulates mechanical properties. Mechanical properties of cells and tissues are known to play a critical role in cancer behaviors such as migration, survival, and proliferation. [155,159,188] In ovarian cancer particularly, prior studies indicate ovarian cancer cells have a lower Young's modulus in contrast to benign cells, suggesting they are more susceptible to physical change under longitudinal forces; however, the exact mechanisms causing this behavior is not clear. [174,189–192] As flow confers a physical stress and has been shown to induce elongated morphology [193], we expected that mechanical properties (*i.e.* stiffness) would be modulated under flow compared to static conditions.

A limitation to standard mechanical analysis techniques is the need for contact with the sample, therefore making analysis of spheroids embedded within a perfusion device impossible. To solve this issue, we apply Brillouin confocal microscopy, an all-optical approach based on an interaction between incident photons and thermally excited acoustic phonons within a material. [136] The Brillouin frequency shift describes the inelastic scattering of photons which is related to the longitudinal modulus at high frequency. A high Brillouin shift indicates a rigid material, while liquid-like medium such as cytosol will result in a lower shift. [194] As biological samples exhibit frequency dependent behaviors and are nearly incompressible, the Brillouin-derived longitudinal modulus probes different properties from traditional stress-strain tests. [141] However, correlative studies demonstrate that a log-log linear relationship exists between the Brillouin longitudinal modulus and Young's modulus in biological tissues and cells. [128,141,142] Specifically, we recently demonstrated

matching trends of the Young's modulus derived using AFM and the Brillouin-derived moduli in tumor spheroids, thus validating the use of Brillouin microscopy for mechanical evaluation in these samples. [147]

As previously mentioned, in the work presented here, we used the same perfusion platform, flow rates, and seeding densities described by Rizvi *et al.* [14], where a range of seeding densities and flow rates were evaluated. The conditions that resulted in consistent tumor growth and modulation of biological parameters over a 7-day timeframe (potentially mimicking physiologically-relevant conditions that are permissive to tumor growth), were then selected. [14] The shear stress conferred by the selected flow rate (~ 3 dyne/cm²) is based on evidence that peritoneal shear stresses are in the range of 0.14 dyne/cm² to 11 dyne/cm². [195] In the present study, the mechanical properties of 3D tumor spheroids were characterized on day 7, and it was found the Brillouin shift was significantly lower under flow, compared to spheroids in a static condition. To explain these differences, we considered that beyond shear stress, tumors in flow were exposed to cumulatively lower osmolality and higher nutrients compared to the static condition, where medium was replenished on days 3 and 6. The role of osmolality on mechanics was evaluated by measuring the Brillouin shift of static spheroids with varied frequency of medium changes. Our results demonstrate a strong association between the extracellular fluid osmolality and the Brillouin shift of spheroids. However, the cumulative history of osmolality did not influence the Brillouin shift, implying that osmotic differences between flow and static conditions were likely short-lived compared to the mechanical effects conferred by shear stress. We also examined the role of nutrients by changing fetal bovine serum concentrations

and found effects on tumor growth but no differences in the Brillouin shift. Our findings of a decrease in tumor spheroid stiffness under flow constitute an important question pertaining to the role of mechanical properties in ovarian cancer progression.

4.2 Methods

4.2.1 Cell Culture

Epithelial ovarian cancer cells (NIH: OVCAR5) were grown in standard culture medium containing RPMI 1640 Medium (Gibco®, #11835030) no phenol red, 10% Fetal Bovine Serum (FBS), and 1% Penicillin-Streptomycin. For low nutrient experiments, the FBS percentage was reduced to 1% or 0.1%. Static Tumor Spheroids: Corning® Matrigel® (Growth Factor Reduced (GFR) Basement Membrane Matrix Phenol Red-Free, *LDEV-Free #356231) was prepared by thawing overnight on ice at 4 °C. The following day, 250 µL of Matrigel was pipetted into wells of a pre-chilled sterile glass bottom 24-well plate (Greiner bio-one Sensoplate, #662892). Basement membranes were incubated at 37 °C for 20-30 minutes for gelation. Meanwhile, OVCAR5 cells were resuspended in medium with a concentration of 10^4 cells/mL and 1 mL was added per well. To replenish cell medium in the cultures, a 1 mL pipette was angled on the side of the well and medium was slowly aspirated and refilled. For flow vs. static experiments, cell medium was replenished on days 3 and 6. For medium change frequency experiments, spheroids were exposed to either no change in medium for 7 days, change day on day 3/6, or a daily change of medium for 7 days. Osmolality: 20 µl of medium within each well was extracted and osmolality was measured using an Advanced® Micro-Osmometer Model 3300. Spheroid Size: ImageJ was used to obtain the spheroid area using an in-house developed macro. [169] Images were

imported and ‘find edges’, ‘make binary’, and ‘analyze particles’ commands were successively performed.

4.2.2 Perfusion Chamber

The assembly of this device is previously described in literature. [147] Briefly, a double-sided adhesive (DSA) film (ARcare 90485; Adhesives Research) designed with 3 channels was pressed onto a glass cover slip. 20 μl of Matrigel was pipetted evenly into the channels of the DSA/glass coverslip assembly. The top sticky side of the DSA was removed and a polymethyl methacrylate (PMMA) part was placed on top. The DSA/PMMA construct was held together using screws. 100 cm tubing was inserted into the three inlet holes using an epoxy resin and hardener. In the same manner, 40 cm tubing was connected to the outlet. Cells were loaded into a 1 mL syringe at a concentration of 1×10^6 cells/mL and loaded into a syringe pump (Harvard Apparatus, Pump 11 Pico Plus #170-2213). The selected concentration was previously established to enable matching cell adherence densities with the static condition. [14] The syringe was connected to the tubing using an 18-G blunt needle and run at a flow rate of 100 $\mu\text{l}/\text{min}$ for 5 minutes to introduce cells into tube. The 1mL syringe was removed as cells reached the inlet of the microfluidic chip. A second syringe of 20 ml was filled with medium supplemented with 2% Matrigel and attached to the syringe pump. The pump was run at a flow rate of 100 $\mu\text{l}/\text{min}$ to introduce cells/medium from tube to chip for 5 minutes. Finally, the pump was run at a flow rate of 2 $\mu\text{l}/\text{min}$ for 7 days and the syringe of 2% Matrigel medium was replaced as needed. The microfluidic chip assembly was stored at 37 °C. A schematic of the microfluidic chip is shown in **Figure 4.1**.

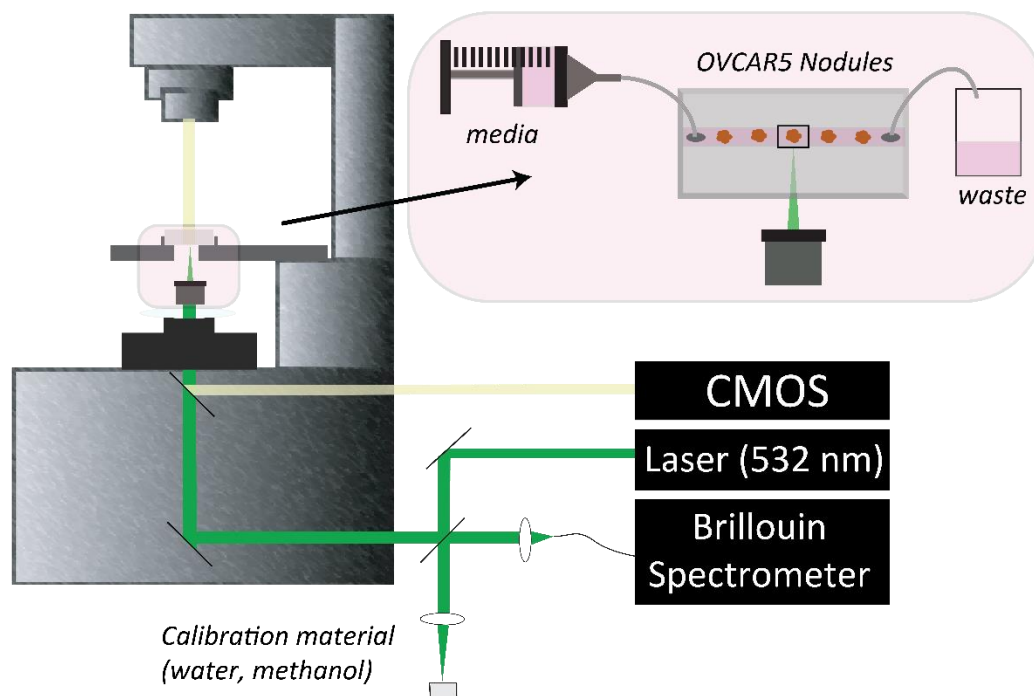


Figure 4.1 Brillouin confocal microscopy setup integrated with microfluidic chip

Schematic of the set-up integrating Brillouin confocal microscopy with a perfusion chamber for the growth of adherent ovarian cancer spheroids under flow. Medium was perfused through the microfluidic chip for 7 days in an incubator at 37°C and on the microscope stage during measurements.

4.2.3 Brillouin Confocal Microscopy

The configuration of Brillouin used here has been previously described in the background. [147] A single longitudinal mode laser (Torus 532 or Torus 660, Laser Quantum) with a wavelength of either 660 nm or 532 nm was used. Measurements comparing flow and static conditions were acquired in a previous set-up which utilized a 532 nm laser. To offer minimal absorption-mediated damage to samples, we now utilize a 660 nm light source. [196] The laser was directed into the side port of an inverted microscope (Olympus, IX81) where light was focused through an objective lens into the sample. Backwards scattered light was then collected by the same objective lens and coupled into the Brillouin spectrometer. The Brillouin spectrometer

is comprised of a two stage virtually imaged phased array (VIPA) in a cross-axis configuration. [136] Calibration was performed prior to the measurements using water (7.46 at 532 nm and 6.01 GHz at 660 nm) and methanol (6.48 at 532 nm and 5.22 GHz at 660 nm) which was further used to calculate the free spectral range (FSR) and convert the image in pixels to a frequency (GHz per pixel). Using a post-processing algorithm developed in MATLAB, the Brillouin spectrums were fit to a Lorentzian function and the Brillouin shift was obtained. To quantify average Brillouin shifts per spheroid, a threshold was used to remove the values corresponding to the surrounding medium of the Brillouin maps and the remaining pixels were averaged. Brillouin maps were acquired in the XZ plane using a 60X/0.7 NA objective lens which has an approximate spatial resolution of 1 μm and axial resolution of 2 μm . We report the *Brillouin elastic contrast* to normalize the numerical values between experiments and wavelengths. The use of a dimensionless quantity $\bar{\nu}_B$ was proposed by Antonacci *et al.* [197] where $\bar{\nu}_B = \nu_B/\nu_B^{(W)} - 1$, such that ν_B is the measured Brillouin frequency shift of the sample and $\nu_B^{(W)}$ is the Brillouin frequency shift of distilled water.

4.2.4 Statistical Analysis

For the flow experiments, a paired t-test assuming equal variances was used to compare to the non-treatment group. For medium exchange and nutrient experiments, a one-way ANOVA was used to compare groups. All statistics were performed using GraphPad Prism7. * ≤ 0.05 ** ≤ 0.01 , *** ≤ 0.001 , **** ≤ 0.0001 .

4.3 Results

4.3.1 Spheroids Decrease Brillouin shift under Flow

To probe the cellular-mechanical effects of flow, we utilized Brillouin confocal microscopy, which enables access to tumors adhered onto Matrigel within a perfusion chamber. Measurements were acquired following 7 days of continuous perfusion of medium. As a control, tumors spheroids were adhered onto Matrigel in static cultures using a 24-well plate. Three independent experiments were performed with a total of $N = 26$ static spheroids and $N = 27$ flow spheroids. Brillouin maps were acquired along the XZ axis with $2 \mu\text{m}$ step size in both dimensions. **Figure 4.2a** shows three representative Brillouin images from the three independent experiments. As shown in **figure 4.2b**, spheroids in the static condition had an average Brillouin shift (532 nm) of 7.92 ± 0.02 GHz (0.062 ± 0.003 Brillouin elastic contrast) while the tumors under flow had an average Brillouin shift (532 nm) of 7.85 ± 0.02 GHz (0.052 ± 0.003 Brillouin elastic contrast).

We used an empirical correlation between longitudinal and Young's modulus previously obtained on spheroids to estimate the corresponding Young's modulus. [147] Longitudinal modulus (M') is defined as $M' = \frac{\rho\lambda^2\Omega^2}{4n^2}$ where ρ is the mass density, λ is the optical wavelength, Ω is the Brillouin shift, and n is the refractive index. We estimated the refractive index to be 1.37 and density is 1.08 g/cm^3 , similar to that of single cells. [128] This equates to a longitudinal modulus of 2.55 MPa for static spheroids and 2.51 for flow spheroids, corresponding to approximately a 13% decrease in Young's modulus.

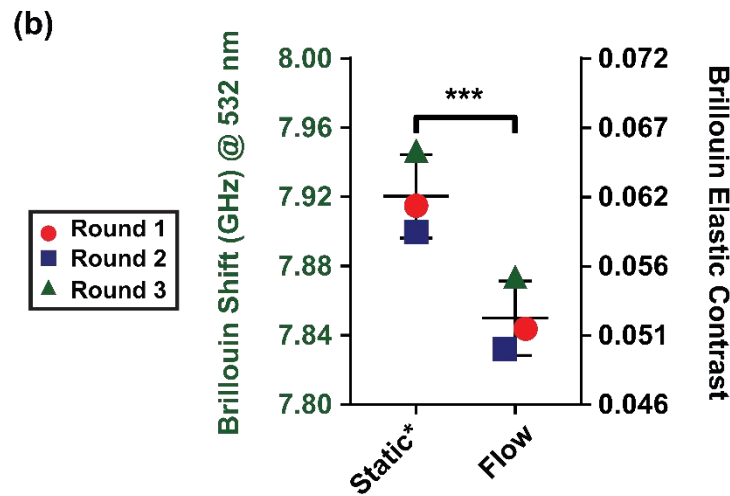
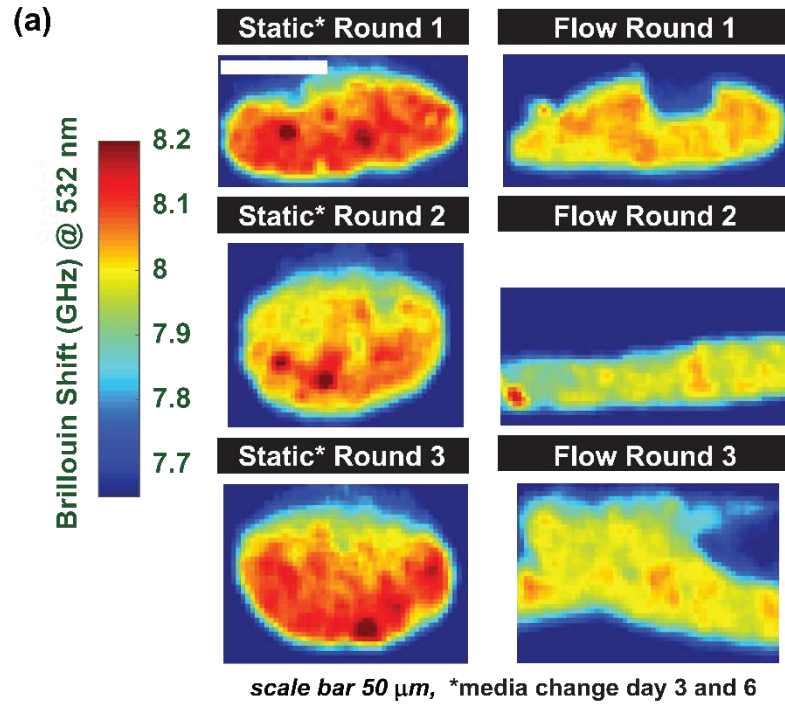


Figure 4.2 Static vs. flow Brillouin shift

(a) Representative Brillouin maps from 3 independent experiments of static and flow conditions. Brillouin images were acquired in the XZ plane perpendicular to the stage. The color bar scale indicates the Brillouin shift in GHz where an increased value (warmer color) indicates a stiffer material. Scale bar = 50 μm . (b) (Left axis) Comparison of static and flow conditions. Each data point represents the average Brillouin shift per round. Three independent rounds of measurements were performed to acquire a total of $N = 26$ spheroids for the static condition and $N = 27$ spheroids for the flow condition. A paired t-test between rounds showed a significant reduction ($***p \leq 0.001$) of the Brillouin shift under flow compared to static. Brillouin shifts were acquired using a 532 nm laser. (Right axis) Conversion of Brillouin shift

to Brillouin elastic contrast, $\bar{\nu}_B = \nu_B/\nu_B^{(W)} - 1$, such that ν_B is the measured Brillouin frequency shift of the sample and $\nu_B^{(W)}$ is the Brillouin frequency shift of distilled water.

4.3.2 Effects of Frequency of Medium Change on Osmolality and Growth of Tumor Spheroids

To explain differences in Brillouin shift between flow and static, we proposed the fluid osmolality of medium could influence mechanics. We first evaluated the osmolality of medium with varying renewal frequencies: no medium change (red squares), medium change on days 3 and 6 (black circles), and daily medium change for 7 days (green triangles) (**Figure 4.3**). No medium change caused a significant rise ($p \leq 0.0001$) in osmolality (mOsm/kg H₂O) compared to the daily medium change and medium change on days 3/6. The control PBS (blue diamonds) shows the variability of the osmometer system (292 ± 3 mOsm/kg H₂O). As expected, in static cultures if the medium is not replenished, waste builds up causing a rise in solute particles inside the well. Another apparent effect of medium change frequency was on tumor growth. As shown in **Figure 4.4a, b**, spheroids that experienced no medium change over a course of 7 days had significantly smaller spheroid areas (μm^2) compared with spheroids that either experienced medium changes on days 3/6 ($p \leq 0.01$) or daily ($p \leq 0.0001$).

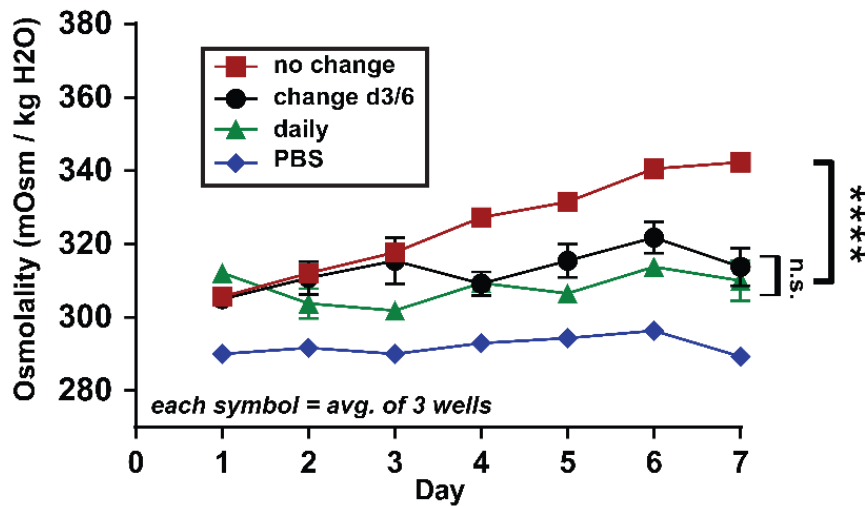


Figure 4.3 Osmolality of medium with varying change frequencies over 7 days

(a) Osmolality of medium over time measured using an osmometer. No medium change (red squares) resulted in a rise in osmolality compared to medium changes on days 3/6 (black circles) and daily medium changes (green triangles). PBS was used to show the variability of the osmometer (blue diamonds). Each data point represents the average of 3 measurements. An ANOVA analysis was performed and showed a significant ($****p \leq 0.0001$) increase in the osmolality of the no change condition compared to the daily condition on day 7. There was no significant difference between the change day 3/6 and daily osmolality on day 7, indicating that the osmolality of the static and flow experiment previously performed was not significantly different.

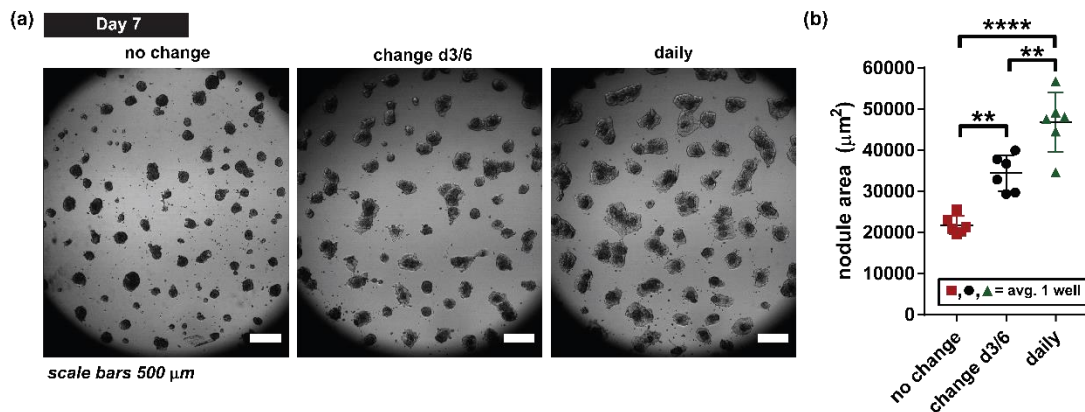


Figure 4.4 Effect of medium change frequency on spheroid size

(a) Brightfield images of adherent ovarian cancer spheroids in static cultures on day 7 for three experimental conditions: no medium change (left panel), medium changes on days 3/6 (middle panel), and daily medium changes (right panel). Scale bars = 500 μm. (b) Spheroid area on day 7 for the three medium change conditions shown in (a). Statistics to analyze significant differences between groups were performed using a one-way ANOVA, where $p \leq 0.05$ (*), $p \leq 0.01$ (**), $p \leq 0.001$ (***), $p \leq 0.0001$ (****).

4.3.3 Brillouin Shift Corresponds to Medium Osmolality, but not Cumulatively

Given that medium change frequency influences osmolality, we sought to determine the role of osmolality on mechanics. On day 7, Brillouin maps of tumor spheroids were acquired in the XZ plane using 1 μm step size (**Figure 4.5a**). Spheroids with no medium change for 7 days had an average Brillouin shift of 6.42 ± 0.01 GHz (0.068 ± 0.001 Brillouin elastic contrast) while spheroids with daily medium changes had a significantly lower Brillouin shift of $6.36 \text{ GHz} \pm 0.02 \text{ GHz}$ (0.058 ± 0.003 Brillouin elastic contrast) ($p \leq 0.0001$).

We next asked if there was a cumulative effect of osmolality changes on the Brillouin shift. Here, we tested whether changing the medium on day 7 of the no medium change group would maintain an increased Brillouin shift, or regress to the daily medium change condition. Interestingly, we found that these spheroids reduced their Brillouin shift immediately after the medium was changed. The average Brillouin shift after the medium change on day 7 was 6.37 ± 0.01 GHz (0.060 ± 0.002 Brillouin Elastic Contrast), which was not significantly different compared to the daily medium change condition (**Figure 4.5b, c**). Altogether, these results demonstrated that osmolality influences tumor mechanics with short-time scales. The lack of a cumulative effect of osmolality on the Brillouin shift supports the idea that the differences observed between flow and static conditions in **Figure 4.2** are minimally affected by osmolality since the osmotic states were matched on day 7 (**Figure 4.3**).

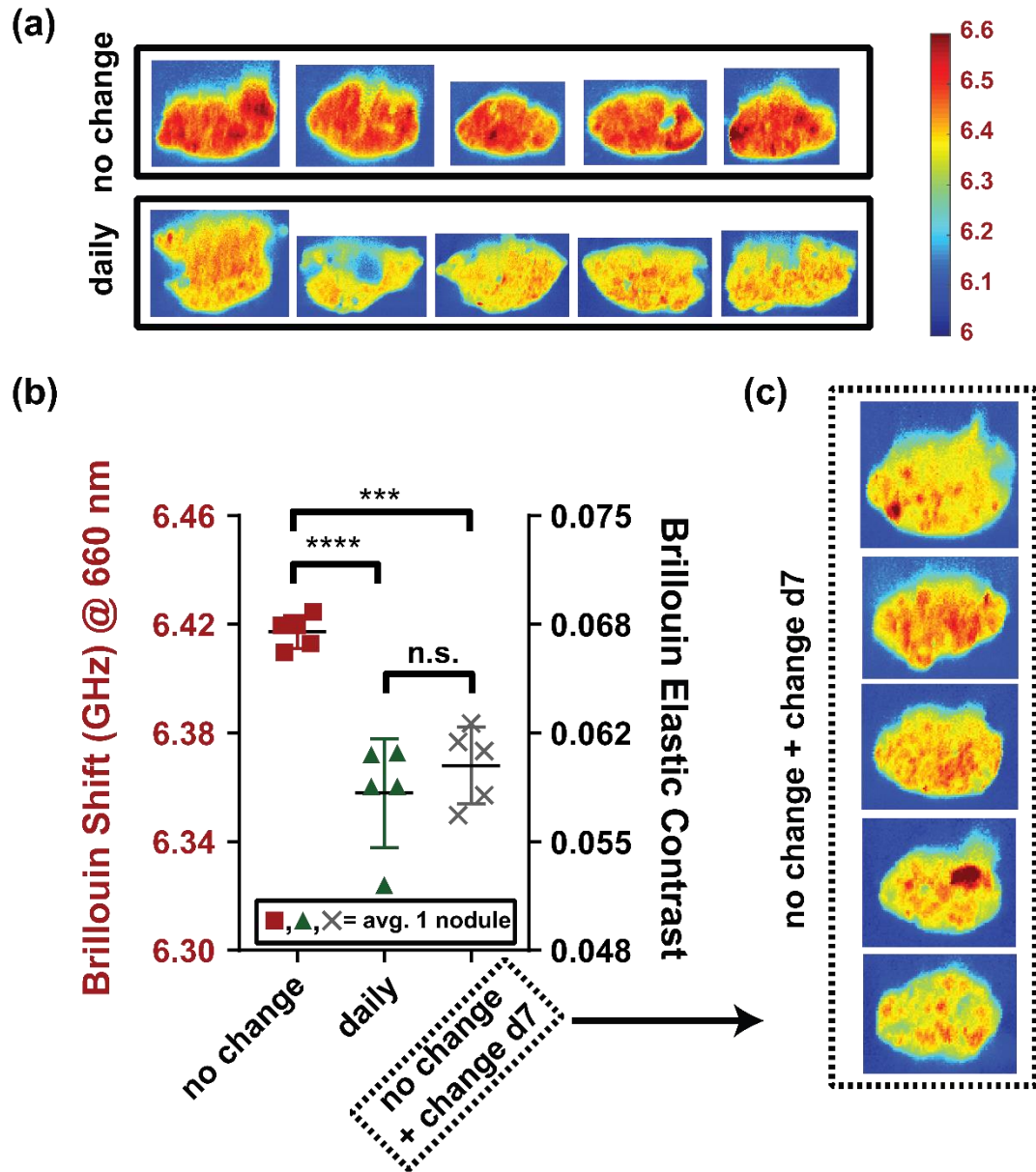


Figure 4.5 Cumulative effect of osmolality on Brillouin Shift

(a) Brillouin maps of spheroids grown with no medium changes (top row) and with daily medium changes (bottom row). Images were acquired in the XZ plane, perpendicular to the Matrigel. (b) (Left Axis) The average Brillouin shift in the no medium change group (red squares) was significantly greater than the average Brillouin shift in the daily medium change group (green triangles) (**** $p \leq 0.0001$). A comparison between the Brillouin shift of the daily medium change and no medium change spheroids for which medium was replenished on day 7 (grey X's) resulted in no significant differences, demonstrating that having a history of a higher osmolality did not influence the mechanical properties. (Right axis) Conversion of Brillouin shift to Brillouin elastic contrast. Statistics to analyze significant differences between groups were performed using a one-way ANOVA, where $p \leq 0.05$ (*), $p \leq 0.01$ (**), $p \leq 0.001$ (***), $p \leq 0.0001$ (****). A total of $N = 5$ spheroids per condition were analyzed. (c) Brillouin maps corresponding to the no medium change + change on day 7 condition.

4.3.4 Nutrient Supply does not Affect the Brillouin Shift

In our previous experiment, we varied the frequency of medium changes; however, there was also a variation of the level of nutrients supplied. For example, changing the medium every day provided ~700 μl of FBS total compared to no medium changes, which provided ~100 μl of FBS total. Thus, we asked whether differences in the availability of nutrients have a direct effect on the mechanical properties of tumors. To test this, spheroids were cultured for 7 days in 1mL of medium supplemented with 0.1%, 1%, and 10% FBS. As expected, higher levels of nutrients caused more growth as pictured in **Figure 4.6a**. On day 3, we measured the Brillouin shift of 9 spheroids per 0.1% FBS and 10% FBS conditions and found no significant differences between the groups (**Figure 4.6b**). Similarly, we measured the osmolality of the medium and found no significant differences (**Figure 4.6c**). Our findings demonstrate that changes in nutrients have a negligible effect on tumor mechanical properties, compared to osmolality, which has a strong effect (**Figures 4.3, 4.4, 4.5**). In addition, the growth of spheroids in these altered FBS concentration conditions appears to be independent of Brillouin shift.

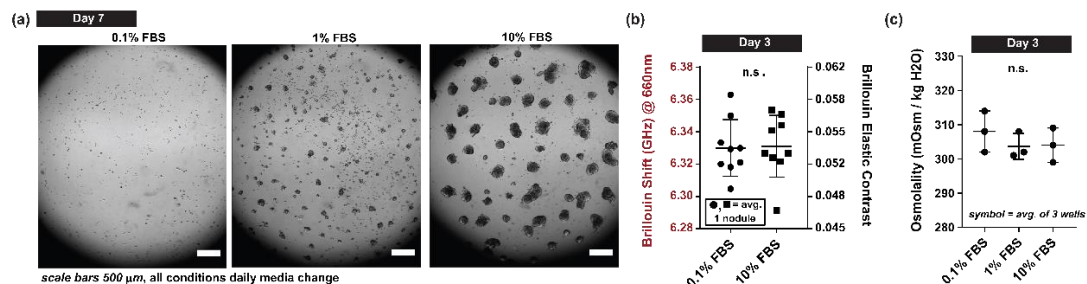


Figure 4.6 Effect of nutrients on spheroid growth and Brillouin shift
(a) Brightfield images of spheroids on day 7 cultured in 0.1%, 1%, and 10% FBS conditions. Scale bars = 500 μm . (b) (Left axis) A t-test analysis revealed no significant differences between the Brillouin shift of spheroids grown in 0.1% FBS and 10% FBS medium. Three

spheroids per well in 3 separate wells were acquired for a total $N = 9$ spheroids. (Right axis) Conversion of Brillouin shift to Brillouin elastic contrast. (c) Osmolality of 0.1% FBS, 1% FBS, and 10% FBS culture medium incubated for 3 days in tumor cultures had no significant difference. Each data point represents one measurement acquired using an osmometer ($N = 3$ measurements per condition).

4.4. Discussion

Here, we present the application of Brillouin confocal microscopy to investigate the mechanical properties of adherent ovarian cancer spheroids grown in a perfusion chamber and subjected to flow for 7 days. It was found that flow caused a decrease in Brillouin shift (i.e., softening of the tumor spheroid). We then performed a series of experiments to test other variables implicated in the flow and static conditions. In addition to shear stress, tumors under flow experienced a cumulatively lower osmolality and higher nutrient supply compared to the static control where medium was replaced on day 3 and 6. To examine the contribution of osmolality on Brillouin shift, we altered the frequency of medium changes in static spheroids and found that higher fluid osmolality directly corresponded to an increased Brillouin shift. The lowest Brillouin shift was observed in the daily medium change condition, which had a Brillouin elastic contrast of 0.058 ± 0.003 . However, we saw that having a cumulative osmolality difference, or history of higher osmolality did not affect mechanics. This was demonstrated by changing the medium on day 7 of spheroids where medium was previously not replenished. The Brillouin elastic contrast of no medium change + change day 7 had a Brillouin elastic contrast of 0.060 ± 0.002 , which was not significantly different from the daily medium change group. Combined with the evidence that spheroids under flow showed a significant decreased Brillouin elastic contrast (0.052 ± 0.003) compared to the daily medium change condition, and that the change day 3/6 medium osmolality is not significantly different from the daily medium

osmolality (**Figure 4.3**), we suspected osmotic influences were negligible in our flow versus static experiments. Finally, we showed that while higher FBS supplementation enhanced spheroid growth, there were no effects on mechanical properties. Altogether, we attribute the observed decrease in Brillouin shift under flow to shear stress effects, with minimal contributions due to osmolality differences. Nonetheless, we emphasize the importance of considering osmolality differences during experimental designs.

The potency of a cell's perception to a variety of microenvironmental mechanical stresses such as fluid shear stress, osmolality, and ECM solid stresses remains unknown. Likely, cells sense multiple cues which can compete or synergize to influence a cell's action. [198] Combined with previous works which analyze the molecular effects of tumor spheroids under flow, there appears to be a relationship between decreased tumor stiffness and activation of EGFR and EMT signaling events. Yet, understanding the correlation between mechanics and biochemical signaling requires a deeper investigation. The fact that fluid shear stress promotes cytoskeletal rearrangement and differential expression of junctional molecules is consistent with observations of the effects of fluid shear stress on vascular endothelial cells. [163,199,200] While the upstream flow sensing molecules and mechanisms remain unknown, cytoskeletal remodeling is accompanied by changes in cell stiffness in endothelial cells [200–202], suggesting that our observed changes in spheroid stiffness could be related to cytoskeletal remodeling.

The strong relationship between water fraction and mechanical properties warrants a discussion on the contribution to mechanical properties by solid and fluid components within cells and other biological materials. Recently, Guo *et al.*, revealed a strong

relationship between cell volume and mechanical properties independent of perturbation method in single cells (e.g., substrate stiffness, osmotic shock, cytoskeletal perturbation). Han *et al.* also demonstrated in tumors that cells at the periphery were both softer and larger. [203] Here, the strong relationship of medium osmolality and the Brillouin shift was substantiated when we found that the mechanical properties could be instantaneously reversed by changing the surrounding fluid osmolality.

Given Brillouin microscopy is an optical approach, this technology offers unique experimental advantages compared to traditional testing systems such as atomic force microscopy (AFM) which require contact with the sample. However, the longitudinal modulus probed by Brillouin scattering is not directly related to the Young's modulus measured by conventional methods. Indeed, the difference in frequency probed (GHz vs quasi-static) and the near incompressibility of biological materials make the two moduli vary by orders of magnitude in absolute values. Nevertheless, numerous experiments find strong correlations in biological samples, including cells, tissues and spheroids. [128,142,147,204] These studies establish an empirical log-log linear relationship to allow estimating the changes to elastic modulus based on changes in Brillouin-derived longitudinal modulus. [128,142,147,204] This is because both moduli are similarly affected by underlying properties such as polymerization, polymer branching, liquid-solid fraction and network tension. [128,142,147,166,204,205] In recent years, several papers have been dedicated to the topic, specifically in terms of dependence on water content. In highly (~95%) hydrated materials, Brillouin signatures are strongly affected by hydration and thus become an unreliable estimator of traditional mechanical properties [179,180]; instead, in the regime of cells, tissues

and spheroids, where we expect the water content to be approximately 70%, it has been shown that Brillouin technology can be used to estimate traditional mechanical properties after proper calibration. [139,206]

Our study has several limitations which are important to discuss. First, results were evaluated using a single ovarian cancer cell line. Therefore, the effects observed here cannot be generalized until assessments on other ovarian cancer and non-cancerous cell lines are performed. Second, spheroids are formed across multiple depths [9,14], yet imaging was performed in one XZ plane; thus, any heterogeneity and directionality dependencies of flow on intratumoral mechanics was disregarded in our analysis. Third, the physiological relevance of osmolality of the tumor microenvironment is largely unknown in the context of ovarian cancer. Particularly, there is a vital need to characterize the osmolality of ascites. Here, we use a perfusion model where fresh medium was supplied. Other groups suggest the use of a perfusion system with medium recirculation, which would inevitably trigger a higher osmolality over time. As gathered from our experiments and the work of others, understanding the contributions of osmolality and shear stress, among other physical factors such as substrate stiffness, are critical to appropriately model the clinical state. Therefore, careful consideration of these factors should be made in the design of future perfusion systems. Finally, here we test a single time-point (7 day) and shear stress (3 dyne/cm²). Measuring at varying durations and rates could give insight to time and stress-dependencies on mechanics.

To conclude, this study analyzes the response of mechanical properties to flow by utilizing Brillouin confocal microscopy, an optical approach with uniquely enables access to confined tumors within a microfluidic chip. Previously, flow has been shown

to alter cell morphology, protein/gene profile, and chemoresistance [9,14,175,193]; here, we show flow also alters mechanical properties. Given this initial evidence of a link between mechanics and chemoresistant phenotype, altering cell mechanics could be considered as a therapeutic target in the future.

Chapter 5 : Water Transport Regulates Nucleus Volume, Cell Density, and Young's Modulus in Tumor Spheroids

5.1 Background

An overlooked phenomenon associated with cancer is osmotic dysregulation. Here, we focused on ovarian cancer which typically results in ascites, the retention of water in the peritoneal cavity caused by leaky vasculature and obstruction of lymphatic drainage. [207,208] Ascites has been clinically associated with hyponatremia, a decreased serum sodium and osmolality level, suggesting that tumors are exposed to abnormal osmotic microenvironments. [10,118,120,209] Given evidence that the tumor microenvironment influence cell phenotypes, considering the effects of cancer in the presence of hypotonic and hypertonic fluids is crucial. It is well described that mechanical properties of cells play an imperative role in behaviors such as migration, gene expression, differentiation, proliferation, and apoptosis. [210–212] Thus in the long-term, understanding the consequences of microenvironmental cues on cell mechanics has the potential to guide the development of novel therapies to target mechanical signaling pathways and regulate cancer behavior.

On several accounts, literature has described a robust relationship between osmotically induced cell volume and mechanics. [84,128,147,166] However, these studies have mostly been performed on single cells, which do not actively incorporate cell-cell adhesions, a fundamental property allowing for spheroid formation and an important attribute of the *in vivo* state. Thus, here we sought to understand how ovarian cancer tumor spheroids acted in response to volume modulations. To regulate water transport, we provoked tumor spheroids using hypotonic and hypertonic shocks.

First, we characterized nuclear volume, density, and Young's modulus relationships in 3D tumor spheroids and compared to relationships derived in literature for single cells. One of the striking behaviors of cancer is the changeover of phenotypes during various stages of metastasis. [213] For example, cells are thought to undergo an epithelial-mesenchymal-transition (EMT) and reverse states via a mesenchymal-epithelial-transition (MET). [214] Thus, one objective was to see if osmotic stress-induced morphology and mechanical effects were reversible.

As opposed to single cells, spheroids possess adhesion junction molecules which are responsible for linking cells together. Thus, we looked to see whether water regulation influenced the expression of the epithelial cell-cell adhesion marker, E-cadherin (E-cad). E-cad is particularly interesting to study in cancer given that a loss is historically associated with an epithelial-mesenchymal-transition. [215,216] Overall, this work contributes to a deeper understanding on the mechanical, morphological, and molecular relationships in response to the physical stress of dysregulated osmolality.

5.2 Methods

5.2.1 Cell Culture

Epithelial ovarian cancer cells (NIH: OVCAR5) were grown using standard procedures. Cells were cultured using RPMI 1640 Medium (Gibco®, #11835030) supplemented with 10% Fetal Bovine Serum (FBS) and 1% Penicillin-Streptomycin. Cells were stored at 37°C and passaged regularly (every 3-5 days).

5.2.2 Spheroid Formation

Spheroids were formed using a Corning™ 96-Well, Ultra-Low Binding, U-Shaped-Bottom Microplate (Corning™ #4515). Cells were diluted to a concentration of 15,000 cells/mL and transferred to an MTC-Bio 25mL Reagent Reservoir (Pipette.com, #P8025-1S). 100 µL (approximately 1500 cells) were then added to each well the low attachment plate using a Rainin Pipet-Lite™ 12 channel manual pipette (Pipette.com, #L12-200R). Cells were incubated overnight at 37°C to allow for spheroid formation.

5.2.3 Polyacrylamide Gels

Polyacrylamide gels were fabricated using a previously established protocol. [33], [34] First, a cotton swab was used to treat the bottom of an 18 mm circular glass coverslip (Electron Microscopy Slides, #72229-01) with 0.1 M NaOH. 200 µl of 3-Cover glasses were coated with Aminopropyltrimethoxysilane (APTMS) for 3 minutes and subsequently washed thoroughly with dH₂O. 400 ul of 0.5% glutaraldehyde was added to the cover glasses for 30 min followed by washing with dH₂O. Top coverslips were coated with RainX on one side with a cotton swab for 5 minutes and washed with dH₂O. Gels with a 1.1 kPa shear modulus were made by combining 94 µl of acrylamide (AA), 15 µl of N,N'-methylene-bis-acrylamide (bis), and 391 µl of phosphate buffered saline (PBS). 1.5 µl of Tetramethylethylenediamine (TEMED) and 5 µl of 10% by weight Ammonium Persulfate (APS) was added to the AA/bis/PBS solution to catalyze polymerization. Solutions were mixed with 1 mL pipette set to 400 ul to avoid air bubbles. 20 µl of the solution was pipetted onto each 18mm diameter glass coverslip. The RainX coated glass coverslip was sandwiched on top and gels were let sit for 15

minutes to allow gel to solidify. PBS was added to each gel for another 15 minutes. The top coverslip was then removed using a razor blade and tweezers. 200 μ L of 1mg/mL solution of Sulfo-SANPAH in 50mM HEPES and 0.25% DMSO was added to the dishes and placed under a UV lamp for 6 minutes to enable crosslinking. Gels were washed with 50 mM of HEPES. The crosslinking process was performed twice. At the end of the crosslinking, gels were washed 3 times with 50mM HEPES. Gels were then coated with 1 mL of a Rat Tail Collagen Coating Solution (50 μ g/ml, Sigma Aldrich, #122-20). Gels were stored overnight at 4°C in FluoroDish Cell Culture Dish - 35mm, 23mm well (World Precision Instruments, #FD35-100).

5.2.4 Transfer of Spheroids

Collagen coated polyacrylamide gels were washed three times with PBS. A Rainin Pipet-Lite™ 12 channel manual pipette set at 50 μ l was used to move spheroids to an MTC-Bio 25mL Reagent Reservoir. Then, 2 mL of the spheroids were transferred to each collagen-coated gel.

5.2.5 Osmotic Shock

Hypotonic shocks were performed by mixing medium with dH₂O at ratios of 1:3 and 1:1. Hypertonic shocks were performed using 500mM and 1000 mM sucrose with medium. Osmolality of solutions were measured with an Advanced® Micro-Osmometer Model 3300 using freezing point depression. *Recovery:* For cell volume, density, and Young's modulus recovery experiments, hyper/hypo-osmotic shocks were performed for 5 or 30 minutes, following by restoration with isotonic medium for the matched duration of the osmotic shock.

5.2.6 Cell Volume Imaging and Analysis

Nuclear volume fluorescent images were acquired using an Olympus FLUOVIEW FV3000 confocal microscope and 30X/1.05 NA silicon oil-immersion objective lens (UPLSAPO). Analysis: Z-stack Olympus (.oir) files were imported into ImageJ, where single nuclei were cropped. [169] Nucleus image stacks (.tiff) were further analyzed in MATLAB using the ‘isosurface’ function and using the function ‘boundary’ to create a 3D ellipsoid mesh. The radii of the spheroid along the x, y, and z dimensions were used to calculate the volume using the equation $V = \frac{4}{3}\pi xyz$.

5.2.7 Cell Density Imaging and Analysis

Images were acquired with the Olympus FLUOVIEW FV3000 and 30X/1.05 NA objective lens. Three locations were randomly selected per spheroid and cells within the area were manually counted using ImageJ. The density was calculated by dividing the number of cells by the area of the image. Since image areas differed based on optimization, the density was normalized to an area of 100 x 100 μm^2 .

5.2.8 Atomic Force Microscopy

A JPK NanoWizard 4a Atomic Force Microscope was employed in force contact mode to generate Young’s moduli maps of spheroids. To probe the cells, a CP-qp-CONT-Au sphere tip (Nanoandmore) with a diameter range of 3 - 5.5 μm was used. Measurements were performed using a 2 μm force distance, extend speed of 2.0 $\mu\text{m}/\text{s}$, and relative setpoint of 2.0 nN. Three 10 x 10 μm force maps with a step size of 1 $\mu\text{m}/\text{pixel}$ were generated per spheroid. A total of 6 spheroids per condition were

acquired. To extract the Young's modulus, force curves were fit to the Hertz model using the JPK Data Processing Software and following equation:

$$F = \frac{4}{3} \cdot \frac{E}{1 - \nu^2} \cdot \sqrt{r} \cdot \delta^{\frac{3}{2}}$$

Eq. 5

where δ is the measured indentation of the sample, E is the Young's modulus, ν is the Poisson's ratio, assumed to be 0.5, and r is tip radius of curvature, assumed to be approximately 5 μm .

5.2.9 E-cadherin Staining Assay

Polyacrylamide gels with a 1.1 kPa shear modulus (G') were prepared as described previously. Tumor spheroids formed in a low attachment plate with 1,500 cells/well were seeded onto the gels. Four hours after transfer, media was changed to a hypertonic (1000 mM sucrose) or hypotonic (25% media + 75% dH₂O) solution for 5 or 30 minutes. For recovery experiments, hypertonic and hypotonic conditions were replenished with isotonic medium for same duration as the shock (either 5 or 30 minutes). Control spheroids in isotonic medium were also prepared. Spheroids were subsequently fixed using 4% formaldehyde for 15 minutes at room temperature. Cells were rinsed three times in 1X PBS for 5 minutes each. A blocking buffer was prepared by mixing 0.5 ml normal goat serum (Cell Signaling, #5425), 0.5 ml 20X PBS, 9.0 ml dH₂O, and 30 μl Triton™ X-100. 1 mL of the blocking buffer was added to the dishes for 1 hour. E-cadherin Rabbit mAb Alexa Fluor® 488 Conjugate (Cell Signaling, #3199) was added at 1:200 dilution and dishes were incubated overnight at 4°C. Cells were imaged using the Olympus FLUOVIEW FV3000. Analysis: ImageJ was used to

convert the images to .PNG files and 16-bit. A threshold minimum was set to 20 counts to remove the background noise. The “analyze particles” function set to a size of 0 to 100 pixels², circularity of 0 to 1.0, including holes was used to calculate the average aggregate size of dense E-cadherin regions. A total of 5 spheroids per condition were analyzed.

5.2.10 Statistical Analysis

For all experiments, a one-way ANOVA was used to compare groups. All statistics were performed using GraphPad Prism7. * ≤ 0.05 ** ≤ 0.01 , *** ≤ 0.001 , **** ≤ 0.0001 .

5.3 Results

5.3.1 Measuring Nuclear Volume in Tumor Spheroids

First, we explored the consequences of water transport on cell morphology. To understand the timeframe which morphology changes occur due to osmotic shocks, we captured consecutive images every 5 seconds and saw that tumor spheroids increased/decreased surface areas within the first 5 minutes of hypotonic/hypertonic shocks, respectively. Therefore, we extrapolated that nuclear volume would be affected as early as 5 minutes after the osmotic shock. The longest duration post-osmotic shock nuclear volume was measured was 40 minutes. Within this time frame, it did not appear that cells activated regulatory volume decrease or increase mechanisms.

To quantify nuclear volume, three cells were randomly selected per spheroid, as indicated by the ‘x’ marks on the example shown in **figure 5.1a**. For each nucleus, confocal stacks of DAPI fluorescent images were acquired (**Figure 5.1b**). Prior work

has demonstrated cell volume and nuclear volume scale proportionally. [166] Thus, here we quantified nuclear volume since a clear boundary was established by a non-fluorescently stained cytoplasm which made analysis easier. An in-house constructed algorithm in MATLAB was used to identify the x, y, and z dimensions and calculate volume (**Figure 5.1c**). In each of the experiments to follow, two hypotonic (25% medium and 50% medium) and two hypertonic (500 mM and 1000 mM sucrose) conditions were tested. 100% medium was used as the control. As reported in **figure 5.1d**, the average osmolalities (mOsm/kg H₂O) were 71 ± 0 (25% medium), 139 ± 1 (25% medium), 278 ± 2 (control), 846 ± 17 (500 mM sucrose), and 1427 ± 35 (1000 mM sucrose). To assess the relationships between osmolality and nuclear volume, we plotted on a logarithmic scale ($\log Y = \kappa \log x + \log \alpha$) where the slope κ refers to the power and exponent of the linear plot $Y = \alpha x^\kappa$. Osmolality (mOsm/kg H₂O) and nucleus volume (μm^3) were related by an inverse correlation, $\log_{10} Y = 4.08 - 0.41 * \log_{10} X$ ($r^2 = 0.80$) (**Figure 5.1e**). The power κ was consistent to a previous correlation by Guo *et al.*, where osmotic pressure and volume of single cells (seeded on polyacrylamide gels with a shear modulus of 1.2 kPa) were related by a power of -0.63. [166]

Given a change in cell volume, we hypothesized that osmotic stress would also result in a cohesive spatial movement of cells. To analyze this effect, we quantified tumor cell density. Previously, it was found in breast cancer spheroids, that after 5 days a spatial gradient developed where cells near the periphery became larger and loosely packed, while cells in the core were smaller and tightly packed. [203,217] Here, we calculated tumor cell density by manually counting the number of nuclei per area in a

similar fashion as the operation of a hemocytometer. As shown in **figures 5.1f** and **5.2**, increased osmolality corresponded to higher packed nuclei. Quantifying this relationship revealed a positive correlation between osmolality (mOsm/kg H₂O) and density (cells per 100 * 100 μm²). The logarithmic relationship between osmolality and nuclear density, implied that density plateaued at increasing hypertonic conditions, indicating a potential maximum packing density of cells was reached.

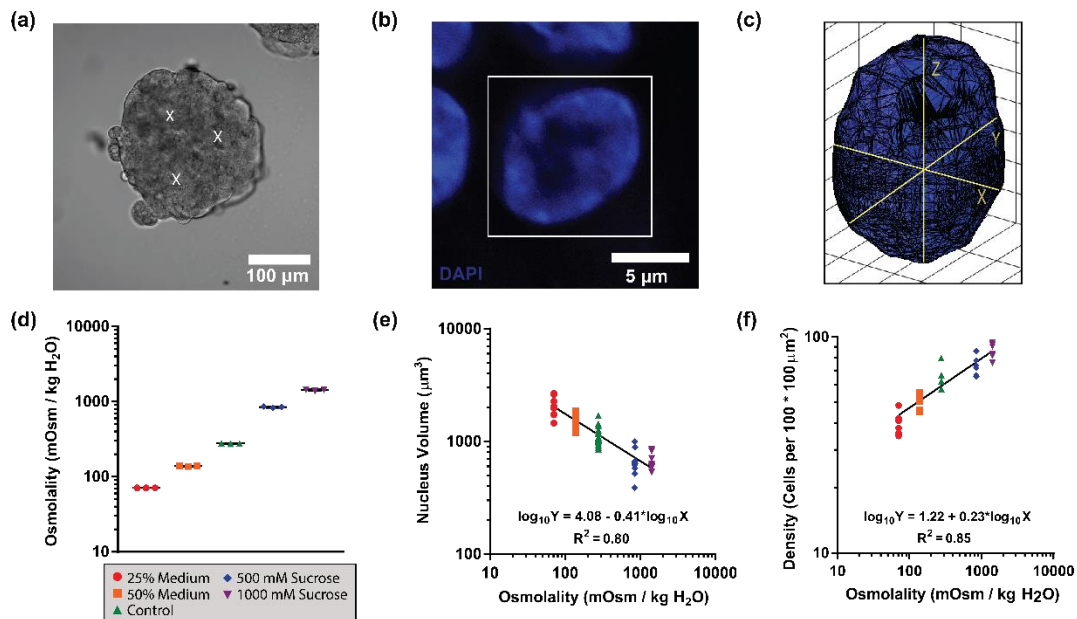


Figure 5.1 Relationship between osmolality and nucleus volume

(a) A representative image of a spheroid cultured using low-attachment spheroid dishes and transferred to a polyacrylamide gel coated with collagen. Spheroids became adhered to the surface after approximately 4 hours of incubation. Three nuclei at random locations within the spheroid were selected for volume analysis, as indicated by “X” symbols. Scale bar = 100 μm. (b) Example fluorescent image of nucleus stained with DAPI. Scale bar = 5 μm. (c) Representative image of nucleus volume calculated in MATLAB. (d) Osmolality of conditions acquired using an osmometer. Each data point represents one measurement and a total of 3 measurements were acquired. (e) Nucleus volume comparison between conditions: 25% medium + 75% dH₂O (red circles), 50% medium + 50% dH₂O (orange squares), control (green upward-triangles), 500 mM sucrose (blue diamonds), 1000 mM sucrose (purple downward-triangles). Each data point represents the average of 3 nuclei in a spheroid. A total N = 9 spheroids were analyzed for all conditions except for the control condition where N = 17 spheroids. (f) Density calculated as cells per 100 x 100 μm area at varying osmotic conditions.

Each data point represents the average of 3 images captured within a single spheroid. N = 6 spheroids per condition.

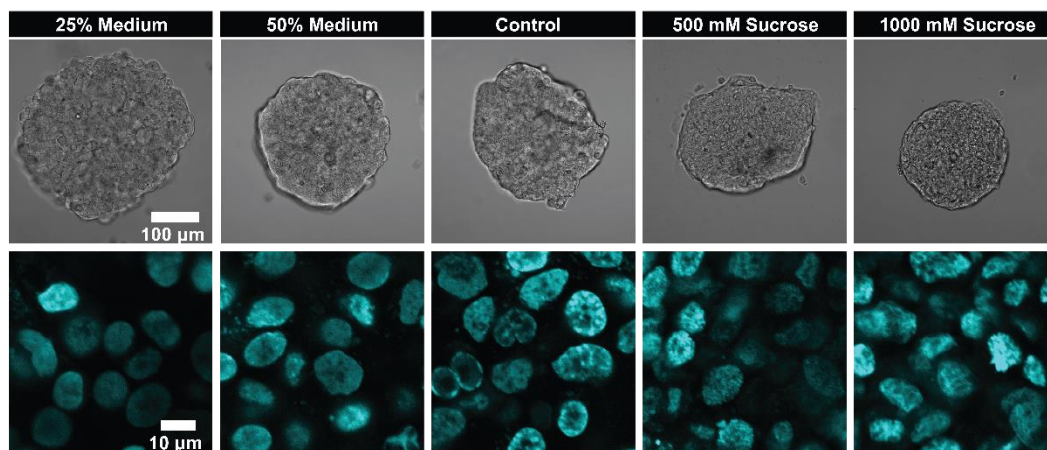


Figure 5.2 Effect of osmotic shock on tumor cell density

(Top) Brightfield images of tumor spheroids (scale bar = 100 μm) (bottom) DAPI stained images (scale bar = 10 μm) at varying osmotic conditions: 25% medium (red circle), 50% medium (orange square), control (green upward-triangle), 500 mM sucrose (blue diamond), and 1000 mM sucrose (purple downward-triangle). Higher osmolality caused an increased density.

5.3.2 Link Between Osmolality and Young's Modulus

Next, we analyzed the effects of osmolality on mechanical properties of spheroids using atomic force microscopy. Prior correlations in single cells showed that hypertonic shocks increase the Young's modulus due to an efflux of water and compression of intracellular contents. [128,166] On the other hand, water influx has been shown to reduce Young's modulus. Here, we analyzed three regions per spheroid, each consisting of a 10 x 10 force map with a step size of 1 μm . (**Figure 5.3a**). **Figure 5.3b** shows the variance of the Young's modulus for an example spheroid in isotonic medium. Using AFM, we found an inverse correlation between osmolality (mOsm/kg H_2O) and Young's modulus (Pa). Our analysis showed these parameters were related

by $\log_{10} Y = -0.21 + 1.08 * \log_{10} X$ ($r^2 = 0.85$) which matched a prior correlation obtained in single cells, which also had a power of ~ 1 . [128] (**Figure 5.3c**).

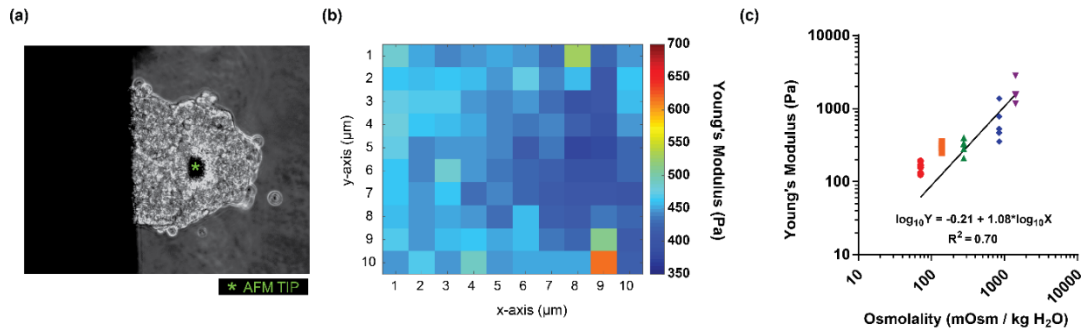


Figure 5.3 Osmolality and Young's Modulus

(a) Example brightfield image of a tumor spheroid adhered to a polyacrylamide gel coated with collagen. AFM probe location is represented by *. (b) Representative AFM map with 100 points total (10 x 10 μm with 1 μm step size). Color bar ranges from 350 Pa to 700 Pa. (c) Young's Modulus acquired for varying conditions: 25% medium (red circles), 50% medium (orange squares), control (green upward-triangles), 500 mM sucrose (blue diamonds), and 1000 mM sucrose (purple downward-triangles). Each data point represents the average Young's modulus of three 10 x 10 μm maps (1 μm step size) collected per spheroid. A total N = 5 spheroids per condition were analyzed.

Furthermore, when plotting cell volume versus Young's modulus, as shown in **Figure 5.4**, we found a power of ~ -2 , which was nearly identical to a previous correlation obtained in single cells. [166] Overall, the tumor spheroid model resembled the morphology and mechanical response to water regulation observed in prior single cell measurements. [128,166]

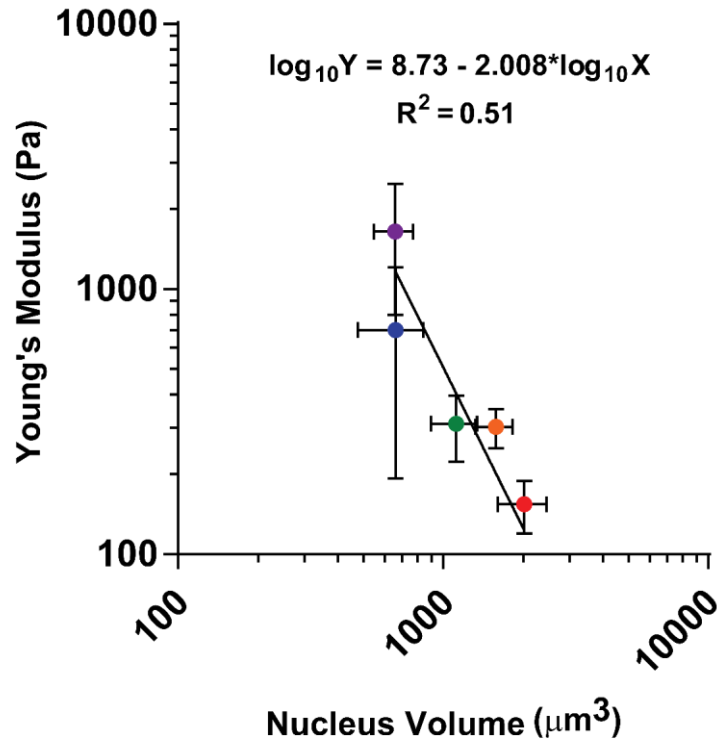


Figure 5.4 Correlation between nucleus volume and Young's Modulus

Nucleus volume from figure 5.1e and Young's modulus from 5.3c plotted. For nucleus volume, mean and standard deviation are displayed where each data point represents the average of 3 nuclei in a spheroid. A total $N = 9$ spheroids were analyzed for all conditions except for the control condition where $N = 17$. For Young's modulus, the mean and standard deviation are plotted where each data point represents the average Young's modulus of three $10 \times 10 \mu\text{m}$ maps ($1 \mu\text{m}$ step size) collected per spheroid. A total $N = 5$ spheroids per condition were analyzed. Colors of data points refer to the varying osmotic conditions: 25% medium (red), 50% medium (orange), control (green), 500 mM sucrose (blue), and 1000 mM sucrose (purple).

5.3.4 Tumor Spheroids can Recovery Volume, Density, Young's Modulus after Osmotic Shocks

Next, we tested the reversibility of nuclear volume, density, and Young's modulus perturbations. Here, tumors were exposed to 5 minutes of 25% medium or 1000 mM sucrose and subsequently replenished with isotonic medium. As shown in **figure 5.5**, there was a complete recovery of all three parameters showcasing the ability of cells to adapt their morphology and mechanics in response to osmotic environments.

Given the extreme osmotic conditions tested in our experiments, we suspect that morphological and mechanical effects in an in vivo state would also be reversible.

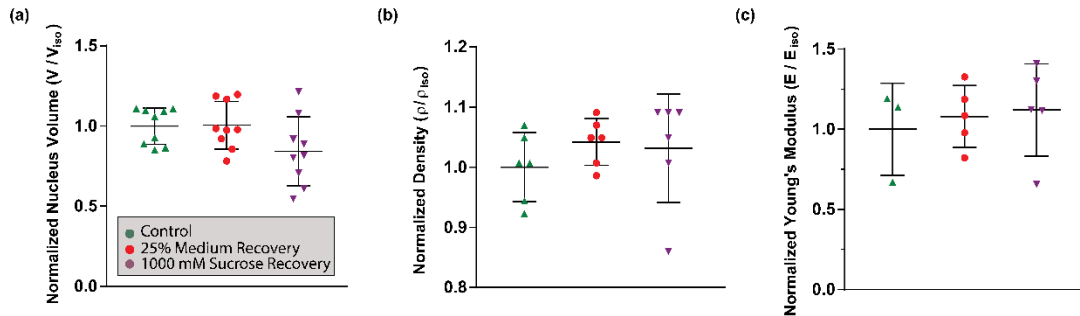


Figure 5.5 Nuclear volume, density, and Young's modulus after recovery

Measurements were acquired after a 5 minute osmotic shock and 5 minute replenishment with isotonic medium. Values are normalized to the average of the control group. A one-way ANOVA analysis revealed no significant difference between groups. Mean and standard deviation are displayed. (a) Recovery of nucleus volume. Each data point represents the average volume of 3 nuclei. A total of N = 9 spheroids per condition were acquired. (b) Recovery of density. Each data point represents the average of three images. A total of N = 6 spheroids were analyzed. (c) Recovery of Young's modulus. Each data point represents the average of three 10 x 10 μm maps with 100 points total. N = 3 for control group and N = 5 for osmotic shock groups.

5.3.5 Effect of Osmotic Shock on E-cadherin Expression

Most epithelial cells express e-cadherin, an adhesion molecule which cooperates with cytoplasmic catenins (*e.g.* p120-catenin, α-catenin, β-catenin) to form bridges between neighboring cells. [218] E-cadherin is thought to play an important role in metastasis and be a biomarker of EMT. [216,219–222] Yet, how the tumor microenvironment impacts e-cadherin expression remains elusive. Previously, we observed that morphology changes occurred in the first 5 minutes of osmotic shock, thus we sought to identify if molecular changes occurred simultaneously. In addition, it is unclear why marker expression changes appear to fluctuate throughout cancer

progression. Thus, we sought to determine if e-cadherin spatial distribution effects were permanent or reversible.

Here, spheroids were subjected to either 25% medium or 1000 mM sucrose for 5 or 30 minutes (**Figure 5.6a**). A control group with isotonic medium was also prepared. In the recovery experiments, spheroids were replenished with isotonic medium for the equal duration as the initial shock (5 or 30 minutes). Spheroids were fixed and stained for E-cadherin using the protocol described in the methods section. To quantify E-cadherin aggregate size, we developed an algorithm in ImageJ. First, intensities of pixels less than 20 counts (background noise) were removed from the image. Next, we used the ‘particle analysis’ function to outline edges, fill holes, and quantify the size of aggregates (**Figure 5.6b**)

First, it was found that spheroids in the control condition displayed an even distribution of E-cadherin on the periphery of cells (**Figure 5.6c**). In our analysis to determine the timescale of e-cadherin effects, we found that a 30 minute osmotic shock was sufficient to cause increased E-cadherin protein aggregate size; yet negligible effects occurred after 5 minutes of osmotic shock. (**Figures 5.7, 5.8, 5.9**). The delay likely signified that cadherin signaling acts on an independent timescale from morphology. When tumors were re-immersed into isotonic medium, we saw that like prior mechanical and morphology recovery experiments, molecular E-cadherin distribution returned to its original state.

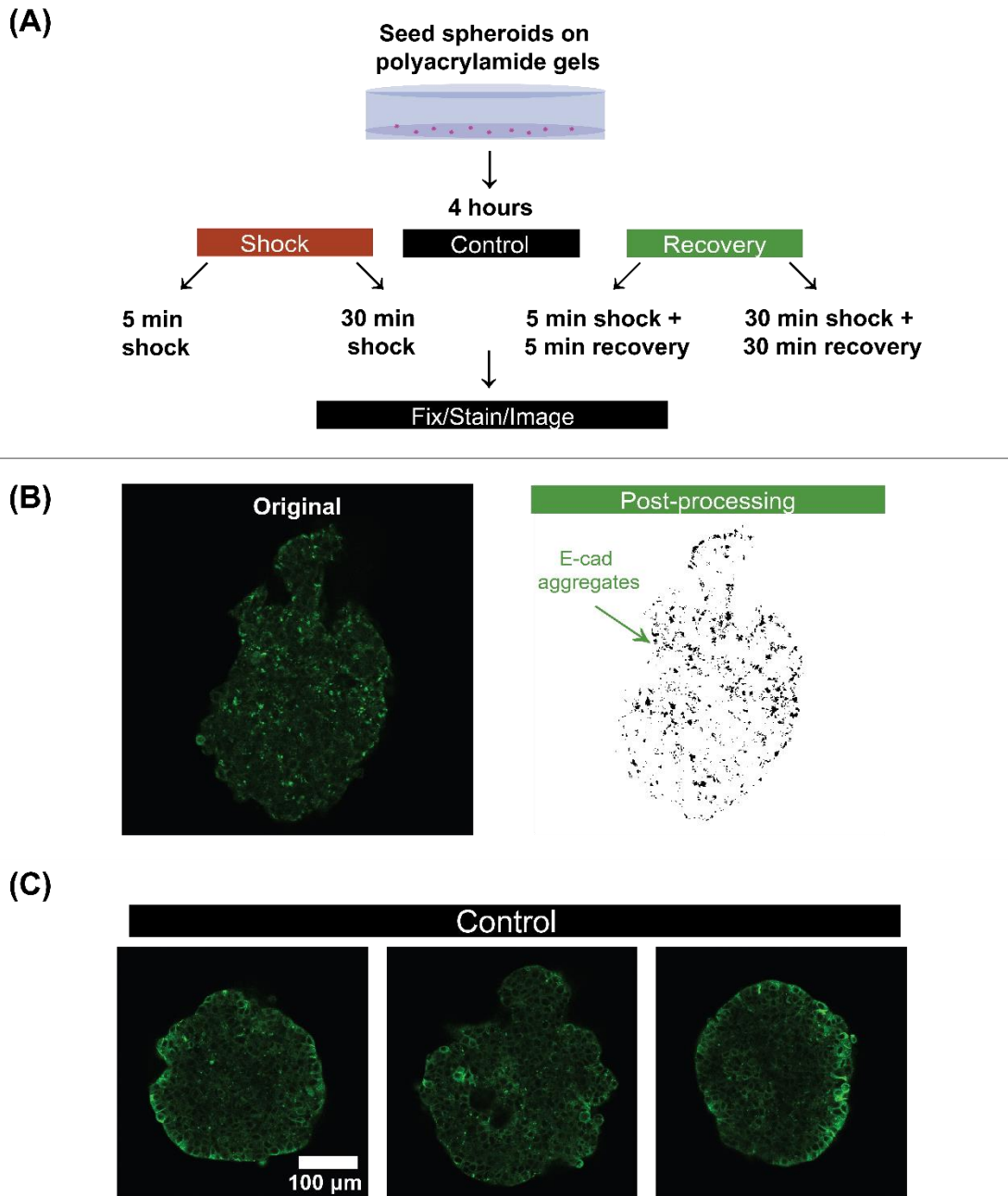


Figure 5.6 E-cadherin experiment design and control

(a) E-cadherin staining protocol. Spheroids were immersed in 25% Medium or 1000 mM sucrose osmotic shock conditions for 5 or 30 minutes. For recovery experiments, spheroids were replenished with isotonic medium for the equivalent duration of the original shock (5 or 30 minutes). (b) Example analysis of E-cadherin aggregate size performed in ImageJ. Low intensity background noise was eliminated using a threshold. Remaining high intensity pixels were analyzed using a particle analysis technique where pixels close in proximity were grouped together. The average size of a cluster (aggregate size) is reported. (c) Control spheroids showed E-cadherin on the periphery of cells. Scale bar = 100 μ m for all images.

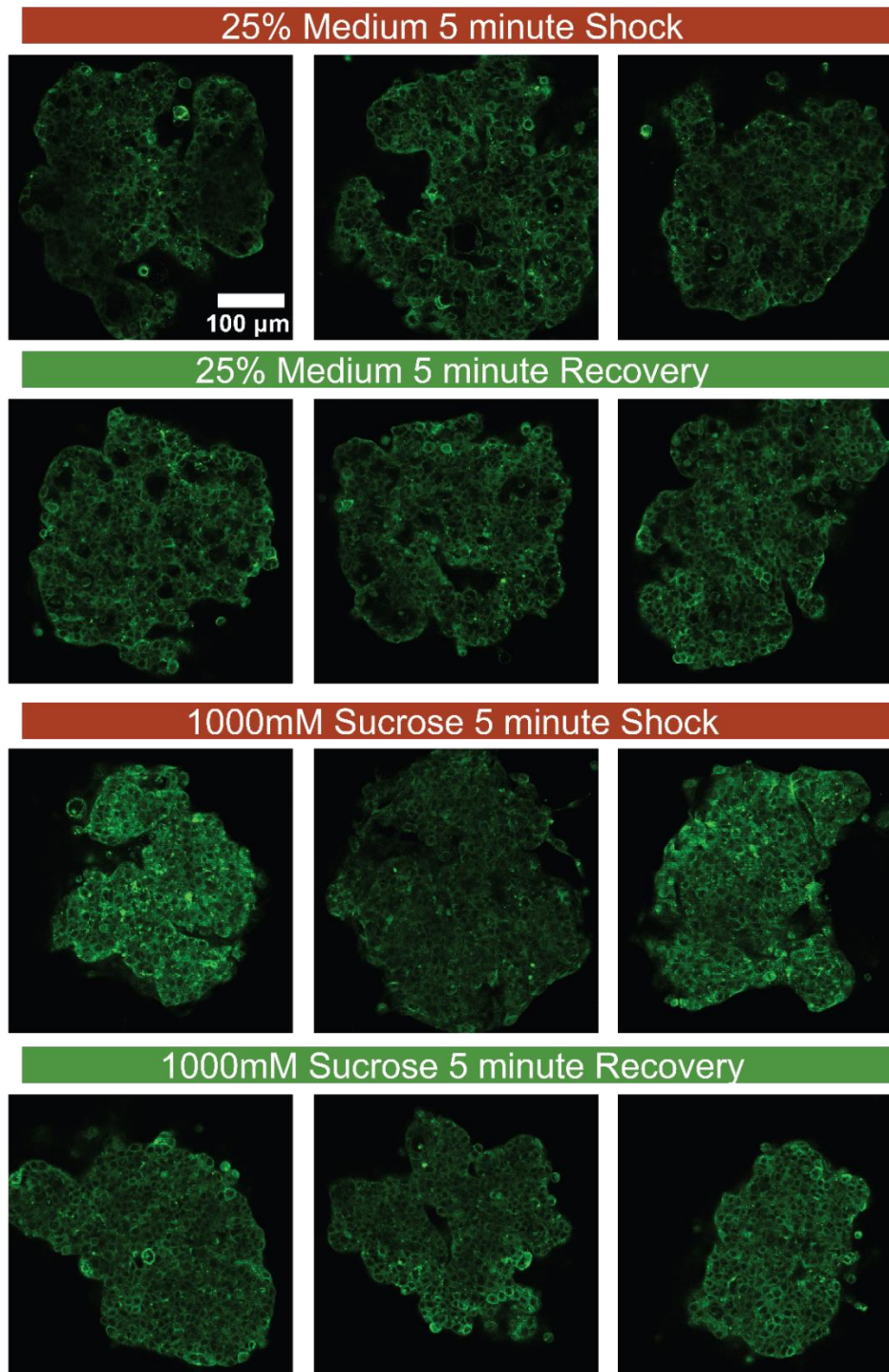


Figure 5.7 E-cadherin expression after 5 minutes of osmotic shock

Example images of E-cadherin expression after 5 minutes of 25% medium or 1000 mM sucrose osmotic shocks. Recovery experiments were performed by replenishing spheroids with 5 minutes of isotonic medium. No effects on e-cadherin aggregate size were observed after 5 minutes of hypotonic and hypertonic shocks. Scale bar = 100 μm for all images.

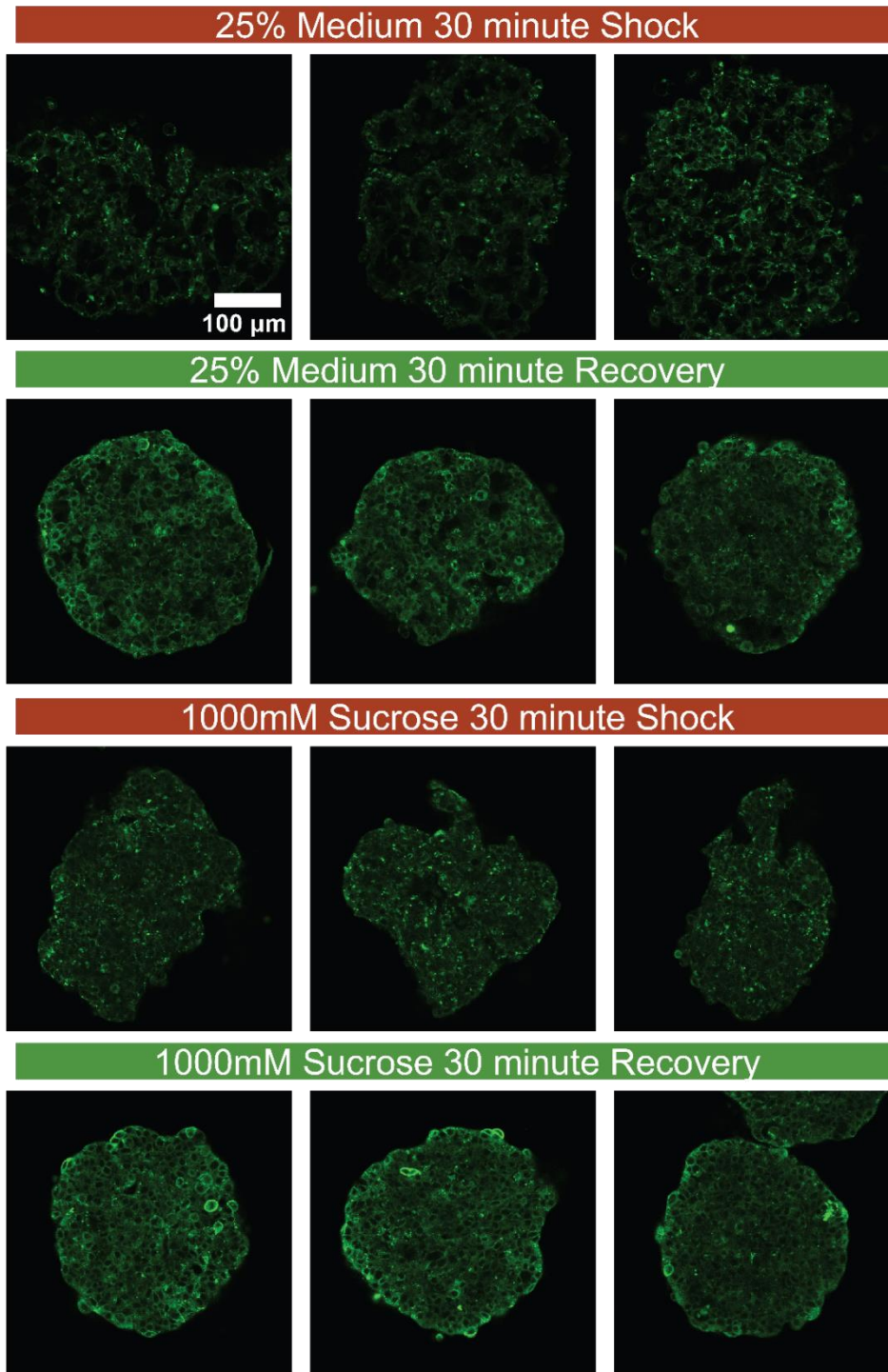


Figure 5.8 E-cadherin expression after 30 minutes of osmotic shocks

Representative images of E-cadherin expression after a 30 minute osmotic shock with 25% medium and 1000 mM sucrose. Recovery experiments were performed by adding replenishing spheroids with 30 minutes of isotonic medium. E-cadherin aggregates appeared in both the 25% medium and 1000 mM sucrose following the 30 minute shock. E-cadherin recovered back to the original state when immersed in isotonic medium. Scale bar = 100 μm for all images.

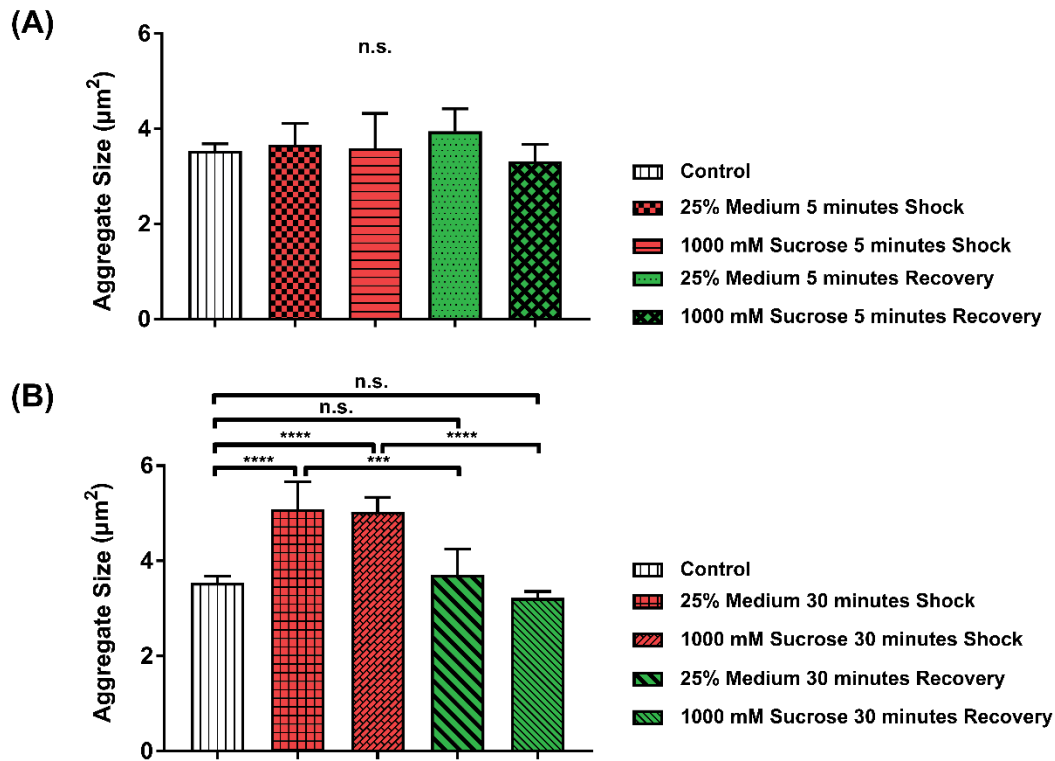


Figure 5.9 E-cadherin aggregate size analysis

Quantification of E-cadherin aggregate size (a) No change in aggregate size after 5 minutes of osmotic shock was observed. (b) A significant increase in aggregate size was found following 30 minutes of 25% medium and 1000 mM osmotic shocks. Aggregate size reduced to match control condition after spheroids were re-immersed for 30 minutes in isotonic medium. Statistics to analyze significant differences between groups were performed using a one-way ANOVA, where $p \leq 0.05$ (*), $p \leq 0.01$ (**), $p \leq 0.001$ (***), $p \leq 0.0001$ (****).

5.4 Discussion

To summarize, the goals of this work were to 1) compare morphology and mechanical responses due to water transport between tumor spheroids and single cells 2) analyze e-cadherin junctions in response to osmotic shock and compare timescales of molecular effects with morphology 3) determine if osmotic shock drives permanent or reversible mechanical, morphology, and molecular variations.

As expected, a higher osmolality (500 mM sucrose and 1000 mM sucrose) caused a smaller nuclear volume and increased Young's modulus due to the efflux of

water. Whereas lower osmolality (25% and 50% medium) produced a larger nuclear volume and lower Young's modulus due to water influx. The logarithmic relationship between osmolality and nuclear volume implied that cells reached a minimum volume of $659 \pm 110 \mu\text{m}^3$, which represented the volume of solid-like components (i.e., chromatin, nucleolus, proteins, etc.) and osmotically unresponsive water, i.e., water associated with protein conformation. The minimum nuclear volume equated to a loss of ~41% of the control nuclear volume ($1120 \mu\text{m}^3$). In comparison, the minimum whole cell volume measured by Guo *et al.* was $2053 \pm 30 \mu\text{m}^3$, which equated to a loss of ~73% (control whole cell volume = $7646 \mu\text{m}^3$). [166] The discrepancies in volume loss may be attributed to differences of osmotically unresponsive water between cell types. [223,224] In addition, 2D versus 3D culture has been shown to cause unique responses to osmotic shocks, even in comparisons between the same cell lines. [110]

Using an in-house algorithm to quantify dense E-cadherin aggregates, we found an increased protein aggregate size following 30 minutes of osmotic shock, but not after 5 minutes. We suspect the time-dependency is due to trafficking of E-cadherin molecules, which is thought to be accomplished via endocytosis and occurs on minute-time scales. [225,226] Despite the formation of protein aggregates at 30 minutes, replenishing spheroids in isotonic medium for an additional 30 minutes caused redistribution of E-cadherin to the cell periphery. There is limited knowledge on how E-cadherin aggregates influence adhesion strength in tumors, but prior work in endothelial cells have shown that a punctate distribution of VE-cadherin is related to decreased adhesion strength and perturbed barrier integrity. [227]

A clinically translational aspect of this work was the observation that mechanical, morphology (**Table 5.1**) and molecular perturbations were reversible. These in vitro experiments indicated that cells have an ability to adapt to new environments with minute timescales. A major challenge in cancer treatment has been the differential expression of markers found at varying disease stages. [63,228] Thus, this work provided evidence that physical cues may be crucial in facilitating transformations like EMT or MET across varying tumor sites and/or intratumoral heterogeneity.

Table 5.1 Summary of percent difference from respective osmotic control

Percent difference of nucleus volume, density, and Young's modulus normalized with respect to the control group for 25% medium, 1000 mM sucrose, 25% medium recovery, and 1000 mM sucrose recovery. Percent change (%) = 100 * (experimental - control) / control.

	25% Medium	1000 mM sucrose	25% medium recovery	1000 mM sucrose recovery
Nucleus Volume	81 ± 38% (****)	-41 ± 10% (***)	1 ± 15% (n.s.)	-16 ± 21% (n.s.)
Density	-39 ± 7% (****)	32 ± 11% (****)	4 ± 4% (n.s.)	3 ± 9% (n.s.)
Young's Modulus	-50 ± 9% (n.s.)	431 ± 220% (****)	8 ± 19% (n.s.)	12 ± 29% (n.s.)

In conclusion, osmoregulation is a critical process, which has been shown to be implicated in protein folding transport, chromatin condensation, proliferation, differentiation, and migration. [70,111,112,166,229–231] This work highlighted an important role of water regulation in nucleus volume, Young's modulus, density, and e-cadherin expression. Importantly, this work was performed in a single cell line (OVCAR5), thus it is not certain that the relationships we observed here can be generalized to other cell types. Another limitation is a lack of clinically relevant values of the osmolality in various fluids relevant to disease states (*e.g* plasma, peritoneal cavity, urine, etc.). Particularly in ovarian cancer, it is important to understand how

hyponatremia may influence mechanical, morphological, and molecular properties and should be accounted for when designing treatment strategies such as chemotherapy or peritoneal drainage. [118,232,233]

Chapter 6 : Conclusion and Future Directions

6.1 Mechanical Effects due to Flow and Osmosis

This dissertation highlighted the effects of flow and osmotic stress, associated with ovarian cancer ascites. Ascites is a dangerous condition which arises in most cases of ovarian cancer and has been shown to promote tumor dissemination, activate members of the EMT and EGFR signaling cascades, and upregulate chemoresistance. [9,14] Given that mechanical properties of cells play a crucial role in behaviors such as migration, gene expression, proliferation, and apoptosis, it is important to understand how the ascites microenvironment alters tumor mechanical properties. [210–212] Overall, our results indicated both flow and osmosis significantly drive mechanical changes.

To study the mechanics of tumors under flow, we used Brillouin confocal microscopy, a non-contact mechanical analysis modality, which enabled the examination of tumor spheroids embedded in a microfluidic chip. [128] We found that tumor spheroids under flow had a decreased Brillouin shift (i.e., decreased stiffness) compared to spheroids in a static condition. Given that tumors under flow were exposed to a cumulatively lower osmolality and higher nutrient supply, we next examined the mechanical contribution of medium change frequency and fetal bovine serum in static conditions. We found that increasing the frequency of medium changes, i.e., maintaining a lower osmolality, caused a lower Brillouin Shift compared to cultures with no medium changes, i.e., having a higher osmolality. By replenishing the medium on day 7 of cultures which previously had no medium changes, we established that having a history of increased osmolality and lowered nutrients did not affect spheroid

mechanics. This evidence confirmed that the lowered Brillouin shift of tumors under flow was likely driven by shear stress, as opposed to osmolality or nutrients. Furthermore, we observed that varying fetal bovine serum concentrations did not directly impact mechanics, thus demonstrating that osmolality was responsible for altering mechanics in the medium change frequency experiments.

Given the significant role of osmolality in regulating tumor spheroid mechanical properties, we next delve into a deeper investigation on the relationships between water transport, morphology, and molecular behaviors. Here, we used a traditional-contact modality to quantify tumor spheroid mechanics, atomic force microscopy. We found hypotonicity caused tumor softening and hypertonicity induced tumor stiffening. When comparing cell volume relationships to mechanical properties, we found that spheroids and single cells possessed similar trends. Based on evidence that ascites induces both shear stress and hypotonic conditions, we suspect metastases in the peritoneal cavity would be subjected to decreased mechanical properties as well as underlying molecular changes. [10,14] A future step is to identify the mechanoreceptors involved in sensing osmotic stress and flow.

While this work was limited in the use of a single ovarian cancer cell line, all cancer types undergoing a metastatic progression inevitably experience measures of stress related to fluid as a result of lymphatic, interstitial or blood flow. [234] Thus, assessing the generalizability of the mechanical effects is another future direction.

Throughout this work, we found several instances of reversible mechanical, morphological, and molecular behaviors in tumors. In chapter 4, we showed the mechanical properties of tumor spheroids in a static condition were directly impacted

by the medium change frequency (i.e., osmotic properties of extracellular fluid). However, having a history of culture in a higher osmotic environment did not leave any lasting effects on the mechanical state when they were reimmersed in isotonic medium. Another instance of reversibility was found in chapter 5, in which tumors immersed in extreme hypotonic and hypertonic fluids reversed nucleus volume, density, Young's modulus, and e-cadherin distribution. These results gave insight on how physical cues of the tumor microenvironment can directly regulate cell phenotypes. Still, there remains many questions on the link between physical properties and fluctuation of cell states relevant to cancer progression, such as EMT and MET.

6.2 A Potential Link Between Mechanics and Chemoresistance

In chapter 4, we showed that flow caused a reduced stiffness of tumor spheroids compared to the static condition. As shown in **figure 6.1**, a previous study led by our collaborators who used same protocol, found that flow upregulated p-ERK and EGFR and downregulated p-Paxillin, p-FAK, and vinculin. [9,14] Additionally, as shown in **figure 6.2**, flow caused increased resistance carboplatin, despite higher platinum uptake. [9,55] The link with softening of the tumor spheroid and tumorigenic characteristics under flow appears to align with studies indicating a decrease in cancer cell stiffness is associated with a poorer prognosis. [131,235] However, it remains unclear on the mechanoreceptor responsible for sensing flow and the downstream signaling mechanisms facilitating upregulated chemoresistance.

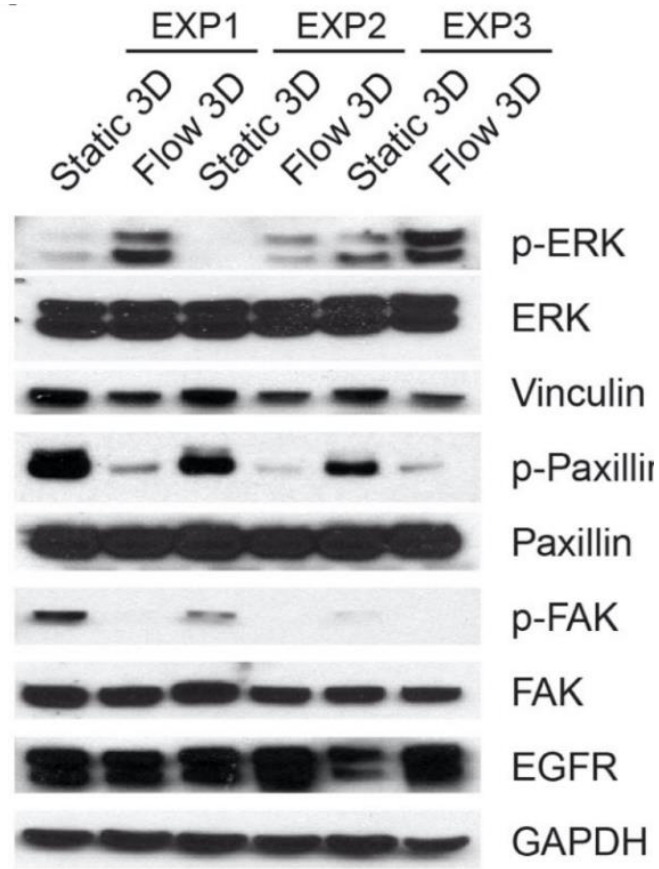


Figure 6.1 Molecular changes due to flow

Figure from Nath et. al., Journal of Clinical Medicine, 2020 [9]. Western blot analysis of tumors in static versus flow conditions. Flow increased p-ERK, EGFR, and decreased vinculin, p-paxillin, and p-FAK expression.

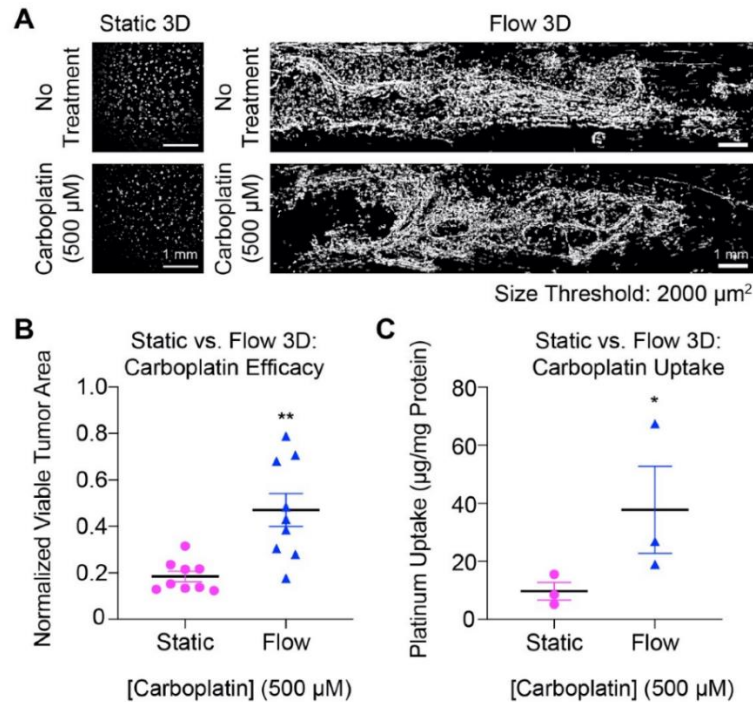


Figure 6.2 Increased chemoresistance under flow

Figure from Nath et. al., Journal of Clinical Medicine, 2020 [9] (a) Representative images of static and flow no treatment and carboplatin treatment groups. (b) Quantification of the normalized viable tumor area revealed a significant increased cytotoxic resistance in tumors under flow (two-tailed t test; ** $p < 0.01$; $N = 9$). (c) Intracellular platinum content was higher for tumors under flow (Mann-Whitney test; * $p \leq 0.05$; $N = 3$).

6.3 Improvements in Modeling the Tumor Microenvironment

In this work, we employed several 3D culture techniques including the overlay of spheroids on Matrigel, low-attachment spheroids on collagen/polyacrylamide gels, and a perfusion model. However, these aforementioned in vitro models had a limited level of complexity. For example, in the perfusion model used in chapter 4, improvements can be made by adding endothelial cells to understand the impact of flow on endothelial-tumor cross-talk. [236]

Another shortcoming of in vitro modeling is a lack of information on solid and fluid parameters related to the clinical state. Many physical parameters associated with ovarian cancer ascites remain unclear such as, fiber architecture, matrix geometry,

porosity, osmotic pressure, hydrostatic pressure, fluid viscosity, shear stress, etc. These parameters could be quantified by acquiring patient-derived tumor and fluid samples. Moreover, the use of organoid models, where tumors are extracted from patient samples, as opposed to cell lines would be beneficial to retain heterogeneity and disease features. [237]

This work contributed a couple additional lessons regarding the future development of 3D models. First, highlighted in chapter 4, the medium change frequency and surrounding osmolality of the tumors drastically influenced tumor properties. Thus, osmolality needs to be accounted for in the design of microfluidics or organ-on-a-chip systems, especially when considering the recirculation of medium which could cause a build-up of waste. Second, in our tumor spheroid model we found that the relationships between volume and stiffness resembled previously established relationships in single cells. [237] Future efforts to validate the spheroid aggregate models against patient samples would be important to understand the model's accuracy.

6.4 Technology development

Finally, mechanical analysis technologies are the crux to advancing our understanding of the interaction between mechanics and diseases. All mechanical analysis techniques suffer a similar drawback in analysis rates. Biological assays such as flow cytometry can sample cells at a rate of $\sim 10,000$ cells/second. Contrary, most mechanical analysis techniques measure on orders of 10 cells/hour or 100 cells/hour. [238–240] To overcome this limitation, continuous flow methods have been proposed to measure cells at speeds of 1,000 cells/hour, thus bridging the gap slightly. [240] Non-contact modalities like Brillouin confocal microscopy have a clear advantage in that

they do not require perturbations to the sample to assess mechanical properties. Yet, improvements in the areas of resolution and depth penetration are ongoing issues. Furthermore, integrating ‘omics’ genetic/protein analysis techniques with mechanics is an exciting opportunity for development. [238]

Chapter 7 : Scientific Contributions

7.1 Publications

1. Nikolić M., **C. Conrad**, J. Zhang, G. Scarcelli. (2018) Noninvasive Imaging: Brillouin Confocal Microscopy. In: C. Dong, N. Zahir, K. Konstantopoulos (eds) Biomechanics in Oncology. Advances in Experimental Medicine and Biology, vol 1092. Springer, Cham.
2. Altartouri, B., A.J. Bidhendi, T. Tani, J. Suzuki, **C. Conrad**, Y. Chebli, N. Liu, C. Karunakaran, G. Scarcelli and A. Geitmann. Pavement cells morphogenesis involves a multi-step mechanism governed by cell wall mechanics. *Plant Physiology*. 2019, 181 (1) 127-141.
3. **Conrad, C.**, K. M. Gray, K. M. Stroka, I. Rizvi and G. Scarcelli. Mechanical Characterization of 3D Ovarian Cancer Nodules Using Brillouin Confocal Microscopy. *Cell. Mol. Bioeng.*, 2019, 12, 215–226.
4. Nath, S.; Pigula, M.; Khan, A.P.; Hanna, W.; Ruhi, M.K.; Dehkordy, F.M.; Pushpavanam, K.; Rege, K.; Moore, K.; Tsujita, Y.; Conrad, C.; Inci, F.; del Carmen, M.G.; Franco, W.; Celli, J.P.; Demirci, U.; Hasan, T.; Huang, H.-C.; Rizvi, I. Flow-induced Shear Stress Confers Resistance to Carboplatin in an Adherent Three-Dimensional Model for Ovarian Cancer: A Role for EGFR-Targeted Photoimmunotherapy Informed by Physical Stress. *J. Clin. Med.* 2020, 9, 924.
5. Li, J., Kim, E., Gray, K. M., **Conrad, C.**, Tsao, C.-Y., Wang, S. P., Zong, G., Scarcelli, G., Stroka, K. M., Wang, L.-X., Bentley, W. E., Payne, G. F.,

Mediated Electrochemistry to Mimic Biology's Oxidative Assembly of Functional Matrices. *Adv. Funct. Mater.* 2020, 2001776.

6. **Conrad, C.**, K. Moore, W. J. Polacheck, I. Rizvi and G. Scarcelli. Mechanical Modulation of Tumor Nodules under Flow. *IEEE Transactions on Biomedical Engineering*. Accepted.

7.2 Presentations

* indicates presenter

1. **Conrad***, C., K.M. Gray, K.M. Stroka. I. Rizvi, and G. Scarcelli. Overcoming the Limitations of 3D Nodule Mechanical Analysis using Brillouin Confocal Microscopy. Research Fest. University of Maryland. June 2018. Poster.
2. **Conrad***, C., K.M. Gray, K.M. Stroka. I. Rizvi, and G. Scarcelli. Evaluating ovarian cancer 3D spheroid mechanical properties using Brillouin confocal microscopy. Bioengineering Graduate Student Society. University of Maryland. August 2018. Talk.
3. **Conrad***, C., K.M. Gray, K.M. Stroka. I. Rizvi, and G. Scarcelli. Overcoming the Limitations of 3D Nodule Mechanical Analysis using Brillouin Confocal Microscopy. Goodbye Flat Biology. Berlin, Germany. September 2018. Poster. Top 8/91 selected for Poster Flash Talk.
4. **Conrad***, C., K.M. Gray, K.M. Stroka. I. Rizvi, and G. Scarcelli. Evaluating ovarian cancer 3D nodule mechanical properties using Brillouin confocal microscopy. Second Annual BioBrillouin Meeting, Perugia, Italy. September 2018. Talk.

5. **Conrad*, C.**, K.M. Gray, K.M. Stroka. I. Rizvi, and G. Scarcelli. Evaluating Ovarian Cancer 3D Nodule Mechanical Properties using Brillouin Confocal Microscopy. 2nd Annual Cancer Research Day. University of Maryland Marlene and Stewart Greenebaum Cancer Center. September 2018. Poster.
6. **Conrad*, C.**, K.M. Gray, K.M. Stroka. I. Rizvi, and G. Scarcelli. Mechanical Characterization of 3D Ovarian Cancer Nodules using Brillouin Confocal Microscopy. 2018 Cancer Systems Biology Consortium and Physical Sciences in Oncology Network (CSBC/PS-ON) Annual Investigators Meeting. Bethesda, Maryland. September 2018. Poster.
7. **Conrad, C.**, K.M. Gray*, K.M. Stroka. I. Rizvi, and G. Scarcelli. Mechanical Characterization of Ovarian Cancer 3D Tumor Nodules using Brillouin Confocal Microscopy. Biomedical Engineering Society Annual Meeting. Atlanta, Georgia. October 2018. Poster.
8. **Conrad*, C.**, K.M. Gray, K.M. Stroka. I. Rizvi, and G. Scarcelli. Mechanical Characterization of Ovarian Cancer 3D Tumor Nodules using Brillouin Confocal Microscopy. 2019 Cellular and Molecular Bioengineering Conference. San Diego, CA. January 2019. Poster.
9. **Conrad*, C.**, I. Rizvi, and G. Scarcelli. The Effects of Fluid Shear Stress on Ovarian Cancer Tumor Nodule Mechanics: A Potential Role of Nutrients and Osmolarity. 3rd Annual Cancer Research Day. University of Maryland Marlene and Stewart Greenebaum Cancer Center. Baltimore, MD. September 2019. Poster.

10. **Conrad***, C., I. Rizvi, and G. Scarcelli. The Effects of Fluid Shear Stress on Ovarian Cancer Tumor Nodule Mechanics: A Potential Role of Nutrients and Osmolarity. Bioengineering Graduate Student Society. College Park, Maryland. October 2019. Talk.
11. **Conrad***, C., H. Aranda-Espinoza. I. Rizvi, and G. Scarcelli. Cell Volume Regulation in 3D Ovarian Cancer Tumor Nodules. Biomedical Engineering Society Annual Meeting. Philadelphia, PA. October 2019. Poster.
12. **Conrad***, C., I. Rizvi, and G. Scarcelli. The Effects of Fluid Shear Stress on Ovarian Cancer Tumor Nodule Mechanics: A Potential Role of Nutrients and Osmolarity. Goodbye Flat Biology. Berlin, Germany. November 2019. Poster.
13. **Conrad***, C., I. Rizvi, and G. Scarcelli. Mechanical Modulation of Tumor Spheroids under Fluid Shear Stress. Mechanobiology Across Length Scales, NIH. Bethesda, Maryland. November 2019. Talk.
14. **Conrad***, C., K. Moore, W. J. Polacheck, I. Rizvi and G. Scarcelli. Mechanical Modulation of Tumor Nodules under Flow. 2020 Cancer Systems Biology Consortium and Physical Sciences in Oncology Network (CSBC/PS-ON) Annual Junior Investigators Meeting. Virtual. August 2020. Poster/Flash Talk.
15. **Conrad***, C., K. Moore, W. J. Polacheck, I. Rizvi and G. Scarcelli. Mechanical Modulation of Tumor Nodules under Flow. Fourth Annual BioBrillouin Meeting. Virtual. September 2020. Talk.
16. **Conrad***, C., K. Moore, W. J. Polacheck, I. Rizvi and G. Scarcelli. Mechanical Modulation of Tumor Nodules under Flow. University of Maryland

Bioengineering Retreat. Virtual. August 2020. Talk. Awarded Top Presentation.

Bibliography

1. Paluch, E. K. *et al.* Mechanotransduction: use the force(s). *BMC Biol.* **13**, 47 (2015).
2. Eyckmans, J., Boudou, T., Yu, X. & Chen, C. S. A Hitchhiker's Guide to Mechanobiology. *Dev. Cell* **21**, 35–47 (2011).
3. Martino, F., Perestrelo, A. R., Vinarský, V., Pagliari, S. & Forte, G. Cellular Mechanotransduction: From Tension to Function. *Frontiers in Physiology* vol. 9 824 (2018).
4. Kumar, S. & Weaver, V. M. Mechanics, malignancy, and metastasis: The force journey of a tumor cell. *Cancer Metastasis Rev.* **28**, 113–127 (2009).
5. Gensbittel, V. *et al.* Mechanical Adaptability of Tumor Cells in Metastasis. *Dev. Cell* (2020) doi:<https://doi.org/10.1016/j.devcel.2020.10.011>.
6. Ahmed, N. & Stenvers, K. L. Getting to know ovarian cancer ascites: opportunities for targeted therapy-based translational research. *Front. Oncol.* **3**, 256 (2013).
7. Huang, H. *et al.* Clinical significance of ascites in epithelial ovarian cancer. *Neoplasma* **60**, 546–552 (2013).
8. Carduner, L. *et al.* Ascites-induced shift along epithelial-mesenchymal spectrum in ovarian cancer cells: enhancement of their invasive behavior partly dependant on α v integrins. *Clin. Exp. Metastasis* **31**, 675–688 (2014).
9. Nath, Shubhankar; Pigula, Michael; Khan, Amjad P.; Hanna, William; Ruhi, Mustafa K.; Dehkordy, Farzaneh M.; Pushpavanam, Karthik; Rege, Kaushal; Moore, Kaitlin; Tsujita, Yujiro; Conrad, Christina; Inci, Fatih; del Carmen,

- Marcela G.; Franco, Walfre; Celli, I. & Nath Michael; Khan, Amjad P.; Hanna, William; Ruhi, Mustafa K.; Dehkordy, Farzaneh M.; Pushpavanam, Karthik; Rege, Kaushal; Moore, Kaitlin; Tsujita, Yujiro; Conrad, Christina; Inci, Fatih; del Carmen, Marcela G.; Franco, Walfre; Celli, Imran., S. P. Flow-induced Shear Stress Confers Resistance to Carboplatin in an Adherent Three-Dimensional Model for Ovarian Cancer: A Role for EGFR-Targeted Photoimmunotherapy Informed by Physical Stress. *J. Clin. Med.* **9**, 924 (2020).
10. Fortune, B. & Cardenas, A. Ascites, refractory ascites and hyponatremia in cirrhosis. *Gastroenterol. Rep.* **5**, 104–112 (2017).
 11. Siegel, R. L., Miller, K. D. & Jemal, A. Cancer Statistics, 2017. *CA. Cancer J. Clin.* **67**, 7–30 (2017).
 12. Cress, R. D., Chen, Y. S., Morris, C. R., Petersen, M. & Leiserowitz, G. S. Characteristics of Long-Term Survivors of Epithelial Ovarian Cancer. *Obs. Gynecol* **126**, 491–497 (2015).
 13. Labidi-Galy, S. I. *et al.* High grade serous ovarian carcinomas originate in the fallopian tube. *Nat. Commun.* **8**, 1093 (2017).
 14. Rizvi, I. *et al.* Flow induces epithelial-mesenchymal transition, cellular heterogeneity and biomarker modulation in 3D ovarian cancer nodules. *PNAS* **110**, 1974–1983 (2013).
 15. Cancer Facts & Figures 2021. *Am. Cancer Soc.* (2021).
 16. Gardner, A. B. *et al.* Ovarian, uterine, and cervical cancer patients with distant metastases at diagnosis: most common locations and outcomes. *Clin. Exp. Metastasis* **37**, 107–113 (2020).

17. Al Habyan, S., Kalos, C., Szymborski, J. & McCaffrey, L. Multicellular detachment generates metastatic spheroids during intra-abdominal dissemination in epithelial ovarian cancer. *Oncogene* **37**, 5127–5135 (2018).
18. Auer, K., Bachmayr-Heyda, A., Aust, S., Grunt, T. W. & Pils, D. Comparative transcriptome analysis links distinct peritoneal tumor spread types, miliary and non-miliary, with putative origin, tubes and ovaries, in high grade serous ovarian cancer. *Cancer Lett.* **388**, 158–166 (2017).
19. Tan, D. S., Agarwal, R. & Kaye, S. B. Mechanisms of transcoelomic metastasis in ovarian cancer. *Lancet Oncol* **7**, 925–934 (2006).
20. He, X., Chien, J. & Shridhar, V. Assessment of resistance to anoikis in ovarian cancer. in *Ovarian cancer* 347–354 (Springer, 2013).
21. Stewart, C., Ralyea, C. & Lockwood, S. Ovarian Cancer: An Integrated Review. *Semin. Oncol. Nurs.* **35**, 151–156 (2019).
22. Reid, B. M., Permuth, J. B. & Sellers, T. A. Epidemiology of ovarian cancer: a review. *Cancer Biol. Med.* **14**, 9–32 (2017).
23. Marusyk, A. & Polyak, K. Tumor heterogeneity: causes and consequences. *Biochim. Biophys. Acta* **1805**, 105–117 (2010).
24. Hatano, Y. *et al.* A Comprehensive Review of Ovarian Serous Carcinoma. *Adv. Anat. Pathol.* **26**, (2019).
25. Norquist, B. M. *et al.* Inherited Mutations in Women With Ovarian Carcinoma. *JAMA Oncol.* **2**, 482–490 (2016).
26. Ciriello, G. *et al.* Emerging landscape of oncogenic signatures across human cancers. *Nat. Genet.* **45**, 1127–1133 (2013).

27. Vassilev, A. & DePamphilis, M. L. Links between DNA Replication, Stem Cells and Cancer. *Genes (Basel)*. **8**, 45 (2017).
28. Iversen, L. *et al.* Association between contemporary hormonal contraception and ovarian cancer in women of reproductive age in Denmark: prospective, nationwide cohort study. *BMJ* **362**, k3609 (2018).
29. Gong, T.-T., Wu, Q.-J., Vogtmann, E., Lin, B. & Wang, Y.-L. Age at menarche and risk of ovarian cancer: a meta-analysis of epidemiological studies. *Int. J. cancer* **132**, 2894–2900 (2013).
30. Gajjar, K., Ogden, G., Mujahid, M. I. & Razvi, K. Symptoms and Risk Factors of Ovarian Cancer: A Survey in Primary Care. *ISRN Obstet. Gynecol.* **754197**, (2012).
31. Ebell, M. H., Culp, M. B. & Radke, T. J. A Systematic Review of Symptoms for the Diagnosis of Ovarian Cancer. *Am. J. Prev. Med.* **50**, 384–394 (2016).
32. Kemppainen, J., Hynninen, J., Virtanen, J. & Seppänen, M. PET/CT for Evaluation of Ovarian Cancer. *Semin. Nucl. Med.* **49**, 484–492 (2019).
33. Dochez, V. *et al.* Biomarkers and algorithms for diagnosis of ovarian cancer: CA125, HE4, RMI and ROMA, a review. *J. Ovarian Res.* **12**, 28 (2019).
34. Montagnana, M., Benati, M. & Danese, E. Circulating biomarkers in epithelial ovarian cancer diagnosis: from present to future perspective. *Ann. Transl. Med.* **5**, 276 (2017).
35. Cortez, A. J., Tudrej, P., Kujawa, K. A. & Lisowska, K. M. Advances in ovarian cancer therapy. *Cancer Chemother. Pharmacol.* **81**, 17–38 (2018).
36. Kim, S. *et al.* Tumor evolution and chemoresistance in ovarian cancer. *NPJ*

- Precis. Oncol.* **2**, 20 (2018).
37. Kurnit, K. C., Fleming, G. F. & Lengyel, E. Updates and New Options in Advanced Epithelial Ovarian Cancer Treatment. *Obstet. Gynecol.* **137**, 108–121 (2021).
 38. Coleman, R. L. *et al.* Veliparib with First-Line Chemotherapy and as Maintenance Therapy in Ovarian Cancer. *N. Engl. J. Med.* **381**, 2403–2415 (2019).
 39. González-Martín, A. *et al.* Niraparib in Patients with Newly Diagnosed Advanced Ovarian Cancer. *N. Engl. J. Med.* **381**, 2391–2402 (2019).
 40. Ray-Coquard, I. *et al.* Olaparib plus Bevacizumab as First-Line Maintenance in Ovarian Cancer. *N. Engl. J. Med.* **381**, 2416–2428 (2019).
 41. Shirley, M. Rucaparib: A Review in Ovarian Cancer. *Target. Oncol.* **14**, 237–246 (2019).
 42. Shishkova, N., Kuznetsova, O. & Berezov, T. Photodynamic therapy for gynecological diseases and breast cancer. *Cancer Biol. Med.* **9**, 9–17 (2012).
 43. Duska, L. R., Hamblin, M. R., Miller, J. L. & Hasan, T. Combination Photoimmunotherapy and Cisplatin: Effects on Human Ovarian Cancer Ex Vivo. *JNCI J. Natl. Cancer Inst.* **91**, 1557–1563 (1999).
 44. Sorrin, A. J. *et al.* Photodynamic Therapy and the Biophysics of the Tumor Microenvironment. *Photochem. Photobiol.* **96**, 232–259 (2020).
 45. Sánchez-Barceló, E. J. & D Mediavilla, M. *Recent Patents on Light Based Therapies: Photodynamic Therapy, Photothermal Therapy and Photoimmunotherapy. Recent patents on endocrine, metabolic & immune drug*

- discovery* vol. 8 (2013).
46. Yokoyama, Y. *et al.* Differences in the sensitivity of ovarian cancer to photodynamic therapy and the mechanisms for those differences. *Oncol. Lett.* **13**, 4933–4938 (2017).
 47. Kipps, E., Tan, D. S. P. & Kaye, S. B. Meeting the challenge of ascites in ovarian cancer: new avenues for therapy and research. *Nat. Rev. Cancer* **13**, 273–282 (2013).
 48. SMOLLE, E., TAUCHER, V. & HAYBAECK, J. Malignant Ascites in Ovarian Cancer and the Role of Targeted Therapeutics. *Anticancer Res.* **34**, 1553 LP – 1561 (2014).
 49. Ford, C. E., Werner, B., Hacker, N. F. & Warton, K. The untapped potential of ascites in ovarian cancer research and treatment. *Br. J. Cancer* **123**, 9–16 (2020).
 50. Cummings, M., Freer, C. & Orsi, N. M. Targeting the tumour microenvironment in platinum-resistant ovarian cancer. *Semin. Cancer Biol.* (2021) doi:<https://doi.org/10.1016/j.semcancer.2021.02.007>.
 51. Shender, V. O. *et al.* Proteome-metabolome profiling of ovarian cancer ascites reveals novel components involved in intercellular communication. *Mol. Cell. Proteomics* **13**, 3558–3571 (2014).
 52. Kuk, C. *et al.* Mining the ovarian cancer ascites proteome for potential ovarian cancer biomarkers. *Mol. Cell. Proteomics* **8**, 661–669 (2009).
 53. Pedersen, J. S., Bendtsen, F. & Møller, S. Management of cirrhotic ascites. *Ther. Adv. Chronic Dis.* **6**, 124–137 (2015).

54. Gu, X.-B., Yang, X.-J., Zhu, H.-Y. & Xu, B.-Y. Effect of a diet with unrestricted sodium on ascites in patients with hepatic cirrhosis. *Gut Liver* **6**, 355–361 (2012).
55. Ip, C. K. M. *et al.* Stemness and chemoresistance in epithelial ovarian carcinoma cells under shear stress. *Sci. Rep.* **6**, 26788 (2016).
56. Li, S.-S. *et al.* Sialyl Lewisx-P-selectin cascade mediates tumor–mesothelial adhesion in ascitic fluid shear flow. *Nat. Commun.* **10**, 2406 (2019).
57. Sun, L. *et al.* Fluid shear stress-induced IL-8/CXCR signaling in human ovarian cancer cells. *Transl. Cancer Res. Vol 8, No 4 (August 2019) Transl. Cancer Res.* (2019).
58. Leggett, S. E., Hruska, A. M., Guo, M. & Wong, I. Y. The epithelial–mesenchymal transition and the cytoskeleton in bioengineered systems. *Cell Commun. Signal.* **19**, 32 (2021).
59. Yeung, K. T. & Yang, J. Epithelial–mesenchymal transition in tumor metastasis. *Mol. Oncol.* **11**, 28–39 (2017).
60. Fabry, B., Klemm, A. H., Kienle, S., Schäffer, T. E. & Goldmann, W. H. Focal adhesion kinase stabilizes the cytoskeleton. *Biophys. J.* **101**, 2131–2138 (2011).
61. Martinez, A. *et al.* Understanding the effect of mechanical forces on ovarian cancer progression. *Gynecol. Oncol.* (2021)
doi:<https://doi.org/10.1016/j.ygyno.2021.04.003>.
62. Kai, F., Laklai, H. & Weaver, V. M. Force matters: biomechanical regulation of cell invasion and migration in disease. *Trends Cell Biol.* **26**, 486–497

- (2016).
63. Mierke, C. T. Mechanical Cues Affect Migration and Invasion of Cells From Three Different Directions. *Front. cell Dev. Biol.* **8**, 583226 (2020).
 64. van Helvert, S., Storm, C. & Friedl, P. Mechanoreciprocity in cell migration. *Nat. Cell Biol.* **20**, 8–20 (2018).
 65. Lecuit, T. & Lenne, P.-F. Cell surface mechanics and the control of cell shape, tissue patterns and morphogenesis. *Nat. Rev. Mol. Cell Biol.* **8**, 633–644 (2007).
 66. Zanutelli, M. R. & Reinhart-King, C. A. Mechanical Forces in Tumor Angiogenesis. *Adv. Exp. Med. Biol.* **1092**, 91–112 (2018).
 67. Nia, H. T., Munn, L. L. & Jain, R. K. Physical traits of cancer. *Science (80-.)*. **370**, eaaz0868 (2020).
 68. Broders-Bondon, F., Nguyen Ho-Bouloires, T. H., Fernandez-Sanchez, M.-E. & Farge, E. Mechanotransduction in tumor progression: The dark side of the force. *J. Cell Biol.* **217**, 1571 LP – 1587 (2018).
 69. Moeendarbary, E. & Harris, A. R. Cell mechanics: principles, practices, and prospects. *Wiley Interdiscip. Rev. Syst. Biol. Med.* **6**, 371–388 (2014).
 70. Moeendarbary, E. *et al.* The cytoplasm of living cells behaves as a poroelastic material. *Nat. Mater.* **12**, 253 (2013).
 71. Hu, J. *et al.* Size-and speed-dependent mechanical behavior in living mammalian cytoplasm. *Proc. Natl. Acad. Sci.* **114**, 9529–9534 (2017).
 72. Mason, T. G. & Weitz, D. A. Optical Measurements of Frequency-Dependent Linear Viscoelastic Moduli of Complex Fluids. *Phys. Rev. Lett.* **TA - TT - 74**,

- 1250–1253 (1995).
73. Kechagia, J. Z., Ivaska, J. & Roca-Cusachs, P. Integrins as biomechanical sensors of the microenvironment. *Nat. Rev. Mol. Cell Biol.* (2019)
doi:10.1038/s41580-019-0134-2.
 74. Bianconi, D., Unseld, M. & Prager, G. W. Integrins in the Spotlight of Cancer. *Int. J. Mol. Sci.* **17**, 2037 (2016).
 75. Maziveyi, M. & Alahari, S. K. Cell matrix adhesions in cancer: the proteins that form the glue. *Oncotarget* **8**, 48471 (2017).
 76. Zaman, M. H. *et al.* Migration of tumor cells in 3D matrices is governed by matrix stiffness along with cell-matrix adhesion and proteolysis. **103**, 10889–10894 (2006).
 77. Kobayashi, M., Sawada, K. & Kimura, T. Potential of Integrin Inhibitors for Treating Ovarian Cancer: A Literature Review. *Cancers (Basel)*. **9**, 83 (2017).
 78. HE, M. & Yang, J. The 2016 John J. Abel Award Lecture: Targeting the Mechanical Microenvironment in Cancer. LK -
<https://umaryland.on.worldcat.org/oclc/6905076030>. *Mol. Pharmacol. TA - TT* - **90**, 744–754 (2016).
 79. Rafiq, N. B. M. *et al.* A mechano-signalling network linking microtubules, myosin IIA filaments and integrin-based adhesions. *Nat. Mater.* **18**, 638–649 (2019).
 80. Sidhaye, V. K., Schweitzer, K. S., Caterina, M. J., Shimoda, L. & King, L. S. Shear stress regulates aquaporin-5 and airway epithelial barrier function. *Proc. Natl. Acad. Sci.* **105**, 3345 LP – 3350 (2008).

81. Kobayashi, T. & Sokabe, M. Sensing substrate rigidity by mechanosensitive ion channels with stress fibers and focal adhesions. *Curr. Opin. Cell Biol.* **22**, 669–676 (2010).
82. Hamidi, H. & Ivaska, J. Every step of the way: integrins in cancer progression and metastasis. *Nat. Rev. Cancer* **18**, 533–548 (2018).
83. Bukoreshtliev, N. V, Haase, K. & Pelling, A. E. Mechanical cues in cellular signalling and communication. *Cell Tissue Res.* **352**, 77–94 (2013).
84. Jiang, H. & Sun, S. X. Cellular pressure and volume regulation and implications for cell mechanics. *Biophys. J.* **105**, 609–619 (2013).
85. Kefauver, J. M., Ward, A. B. & Patapoutian, A. Discoveries in structure and physiology of mechanically activated ion channels. *Nature* **587**, 567–576 (2020).
86. Jojoa-Cruz, S. *et al.* Cryo-EM structure of the mechanically activated ion channel OSCA1.2. *Elife* **7**, e41845 (2018).
87. Marques, M. C., Albuquerque, I. S., Vaz, S. H. & Bernardes, G. J. L. Overexpression of Osmosensitive Ca²⁺-Permeable Channel TMEM63B Promotes Migration in HEK293T Cells. *Biochemistry* **58**, 2861–2866 (2019).
88. Moroni, M., Servin-Vences, M. R., Fleischer, R., Sánchez-Carranza, O. & Lewin, G. R. Voltage gating of mechanosensitive PIEZO channels. *Nat. Commun.* **9**, 1096 (2018).
89. De Felice, D. & Alaimo, A. Mechanosensitive Piezo Channels in Cancer: Focus on altered Calcium Signaling in Cancer Cells and in Tumor Progression. *Cancers (Basel)*. **12**, 1780 (2020).

90. Freund, J. B., Goetz, J. G., Hill, K. L. & Vermot, J. Fluid flows and forces in development: functions, features and biophysical principles. *Development* **139**, 1229–1245 (2012).
91. Pethő, Z., Najder, K., Bulk, E. & Schwab, A. Mechanosensitive ion channels push cancer progression. *Cell Calcium* **80**, 79–90 (2019).
92. Baratchi, S., Knoerzer, M., Khoshmanesh, K., Mitchell, A. & McIntyre, P. Shear Stress Regulates TRPV4 Channel Clustering and Translocation from Adherens Junctions to the Basal Membrane. *Sci. Rep.* **7**, 15942 (2017).
93. Hyman, A. J., Tumova, S. & Beech, D. J. Chapter Two - Piezo1 Channels in Vascular Development and the Sensing of Shear Stress. in *Piezo Channels* (ed. Gottlieb, P. A. B. T.-C. T. in M.) vol. 79 37–57 (Academic Press, 2017).
94. LANG, F. *et al.* Functional Significance of Cell Volume Regulatory Mechanisms. *Physiol. Rev.* **78**, 247–306 (1998).
95. Delpire, E. & Gagnon, K. B. Water Homeostasis and Cell Volume Maintenance and Regulation. *Curr. Top. Membr.* **81**, 3–52 (2018).
96. Brinkman, J. & Sharma, s. Physiology, Body Fluids. in (2018).
97. Boone, M. & Deen, P. M. T. Physiology and pathophysiology of the vasopressin-regulated renal water reabsorption. *Pflugers Arch.* **456**, 1005–1024 (2008).
98. Model, M. A. Methods for cell volume measurement. *Cytom. Part A* **93**, 281–296 (2018).
99. Kay, A. R. How Cells Can Control Their Size by Pumping Ions . *Frontiers in Cell and Developmental Biology* vol. 5 41 (2017).

100. Yancey, P. H. Organic osmolytes as compatible, metabolic and counteracting cytoprotectants in high osmolarity and other stresses. *J. Exp. Biol.* **208**, 2819 LP – 2830 (2005).
101. Jentsch, T. J. VRACs and other ion channels and transporters in the regulation of cell volume and beyond. *Nat. Rev. Mol. Cell Biol.* **17**, 293–307 (2016).
102. Brown, D. The Discovery of Water Channels (Aquaporins). *Ann. Nutr. Metab.* **70(suppl 1)**, 37–42 (2017).
103. Disalvo, E. A. *et al.* Functional role of water in membranes updated: A tribute to Träuble. *Biochim. Biophys. Acta - Biomembr.* **1848**, 1552–1562 (2015).
104. Fischbarg, J. *et al.* Glucose transporters serve as water channels. *Proc. Natl. Acad. Sci. U. S. A.* **87**, 3244–3247 (1990).
105. Alberts, B. *et al.* *Molecular biology of the cell LK* - <https://umaryland.on.worldcat.org/oclc/926585551>. TA - TT - (Garland Science, 2015).
106. Kim, D.-H. *et al.* Volume regulation and shape bifurcation in the cell nucleus. *J. Cell Sci.* **128**, 3375 LP – 3385 (2015).
107. Mongin, A. A. & Orlov, S. N. Mechanisms of cell volume regulation and possible nature of the cell volume sensor. *Pathophysiology* **8**, 77–88 (2001).
108. Cacace, V. I. *et al.* Regulatory Volume Increase and Regulatory Volume Decrease Responses in HL-1 Atrial Myocytes. *Cell. Physiol. Biochem.* **33**, 1745–1757 (2014).
109. Morishita, K., Watanabe, K. & Ichijo, H. Cell volume regulation in cancer cell migration driven by osmotic water flow. *Cancer Sci.* **110**, 2337–2347 (2019).

110. Miermont, A., Lee, S. W. L., Adriani, G. & Kamm, R. D. Quantitative screening of the effects of hyper-osmotic stress on cancer cells cultured in 2- or 3-dimensional settings. *Sci. Rep.* **9**, 13782 (2019).
111. Pu, W., Qiu, J., Riggins, G. J. & Parat, M.-O. Matrix protease production, epithelial-to-mesenchymal transition marker expression and invasion of glioblastoma cells in response to osmotic or hydrostatic pressure. *Sci. Rep.* **10**, 2634 (2020).
112. Lee, H., Stowers, R. & Chaudhuri, O. Volume expansion and TRPV4 activation regulate stem cell fate in three-dimensional microenvironments. *Nat. Commun.* **10**, 529 (2019).
113. De Ieso, M. L. & Yool, A. J. Mechanisms of Aquaporin-Facilitated Cancer Invasion and Metastasis. *Front. Chem.* **6**, 135 (2018).
114. Yan, C. *et al.* Down-regulated aquaporin 5 inhibits proliferation and migration of human epithelial ovarian cancer 3AO cells. *J. Ovarian Res.* **7**, 78 (2014).
115. Direito, I., Madeira, A., Brito, M. A. & Soveral, G. Aquaporin-5: from structure to function and dysfunction in cancer. *Cell. Mol. Life Sci. TA - TT -* **73**, 1623–1640 (2016).
116. Wang, J. *et al.* Expression of aquaporin 3 in the human prostate. *Int. J. Urol.* **14**, 1088–1092 (2007).
117. Seri, I., Ramanathan, R. & Evans, J. R. Chapter 30 - Acid-Base, Fluid, and Electrolyte Management. in (eds. Taesch, H. W., Ballard, R. A. & Gleason, C. A. B. T.-A. D. of the N. (Eighth E.) 372–397 (W.B. Saunders, 2005).
doi:<https://doi.org/10.1016/B978-072169347-7.50032-9>.

118. Gupta, S. *et al.* Incidence of Hyponatremia in Patients With Indwelling Peritoneal Catheters for Drainage of Malignant Ascites. *JAMA Netw. Open* **3**, e2017859–e2017859 (2020).
119. McManus, M. L., Churchwell, K. B. & Strange, K. Regulation of Cell Volume in Health and Disease. *N. Engl. J. Med.* **333**, 1260–1267 (1995).
120. Djamgoz, M. B. A. Hyponatremia and Cancer Progression: Possible Association with Sodium-Transporting Proteins. *Bioelectricity* **2**, 14–20 (2020).
121. GD, S. Hyperosmolar hyperglycemic state. LK - <https://umaryland.on.worldcat.org/oclc/112042105>. *Am. Fam. physician TA - TT* - **71**, 1723–1730 (2005).
122. Guck, J. *et al.* The Optical Stretcher: A Novel Laser Tool to Micromanipulate Cells. *Biophys. J.* **81**, 767–784 (2001).
123. Hochmuth, R. M. Micropipette aspiration of living cells. *J. Biomech.* **33**, 15–22 (2000).
124. Haase, K. & Pelling, A. E. Investigating cell mechanics with atomic force microscopy. *J. R. Soc. Interface* **12**, 20140970 (2015).
125. Harris, A. K., Wild, P. & Stopak, D. Silicone rubber substrata: a new wrinkle in the study of cell locomotion. *Science (80-.)*. **208**, 177–179 (1980).
126. Tseng, Y., Kole, T. P. & Wirtz, D. Micromechanical Mapping of Live Cells by Multiple-Particle-Tracking Microrheology. *Biophys. J.* **83**, 3162–3176 (2002).
127. Wang, N., Butler, J. P. & Ingber, D. E. Mechanotransduction across the cell surface and through the cytoskeleton. *Science (80-.)*. **260**, 1124–1127 (1993).

128. Scarcelli, G. *et al.* Noncontact three-dimensional mapping of intracellular hydro-mechanical properties by Brillouin microscopy. *Nat Methods* **12**, 1132–1134 (2015).
129. Guck, J., Ananthkrishnan, R., Moon, T. J., Cunningham, C. C. & Kas, J. Optical deformability of soft biological dielectrics. *Phys Rev Lett* **84**, 5451–5454 (2000).
130. Wu, P.-H. *et al.* A comparison of methods to assess cell mechanical properties. *Nat. Methods* **15**, 491 (2018).
131. Alibert, C., Goud, B. & Manneville, J. B. Are cancer cells really softer than normal cells? *Biol Cell* **109**, 167–189 (2017).
132. Mason, T. G. & Weitz, D. A. Optical measurements of frequency-dependent linear viscoelastic moduli of complex fluids. *Phys. Rev. Lett.* **74**, 1250–1253 (2018).
133. Gossett, D. R. *et al.* Hydrodynamic stretching of single cells for large population mechanical phenotyping. *PNAS* **109**, 7630–7635 (2012).
134. Brillouin, L. Diffusion de la lumière et des rayons X par un corps transparent homogène Influence de l'agitation thermique. *Ann. Phys. TA - TT - 9*, 88–122 (1922).
135. Mandelstam, L. I. Light scattering by inhomogeneous media. *Zh. Russ. Fiz-Khim. Ova* **58**, 381 (1926).
136. Scarcelli, G. & Yun, S. H. Confocal Brillouin microscopy for three-dimensional mechanical imaging. *Nat. Photonics* **2**, 39–43 (2008).
137. Altartouri, B. *et al.* Pectin Chemistry and Cellulose Crystallinity Govern

- Pavement Cell Morphogenesis in a Multi-Step Mechanism. *Plant Physiol.* **181**, 127 LP – 141 (2019).
138. Elsayad, K. *et al.* Mapping the subcellular mechanical properties of live cells in tissues with fluorescence emission–Brillouin imaging. *Sci. Signal.* **9**, rs5 LP-rs5 (2016).
139. Webb, J., Zhang, H., Sinha Roy, A., Randleman, J. & Scarcelli, G. Detecting Mechanical Anisotropy of the Cornea Using Brillouin Microscopy. *Transl. Vis. Sci. Technol.* **in press**, (2020).
140. Scarcelli, G. *et al.* Brillouin microscopy of collagen crosslinking: noncontact depth-dependent analysis of corneal elastic modulus. *Invest Ophthalmol Vis Sci.* **54**, 1418–1425 (2013).
141. Scarcelli, G., Pineda, R. & Yun, S. H. Brillouin optical microscopy for corneal biomechanics. *Invest. Ophthalmol. Vis. Sci.* **53**, 185–190 (2012).
142. Webb, J. N., Su, J. P. & Scarcelli, G. Mechanical outcome of accelerated corneal crosslinking evaluated by Brillouin microscopy. *J Cataract Refract Surg* **43**, 1458–1463 (2017).
143. Yun, S. H. & Chernyak, D. Brillouin microscopy: assessing ocular tissue biomechanics. *Curr. Opin. Ophthalmol.* **29**, 299–305 (2018).
144. Raghunathan, R. *et al.* Evaluating biomechanical properties of murine embryos using Brillouin microscopy and optical coherence tomography. *J. Biomed. Opt.* **22**, 1–6 (2017).
145. Schlüßler, R. *et al.* Mechanical Mapping of Spinal Cord Growth and Repair in Living Zebrafish Larvae by Brillouin Imaging. *Biophys. J.* **115**, 911–923

- (2018).
146. Cardinali, M. A. *et al.* Mechano-chemistry of human femoral diaphysis revealed by correlative Brillouin–Raman microspectroscopy. *Sci. Rep.* **10**, 17341 (2020).
 147. Conrad, C., Gray, K. M., Stroka, K. M., Rizvi, I. & Scarcelli, G. Mechanical Characterization of 3D Ovarian Cancer Nodules Using Brillouin Confocal Microscopy. *Cell. Mol. Bioeng.* (2019) doi:10.1007/s12195-019-00570-7.
 148. Roberts, A. B. *et al.* Tumor cell nuclei soften during transendothelial migration. *J. Biomech.* **121**, 110400 (2021).
 149. Zhang, J., Nou, X. A., Kim, H. & Scarcelli, G. Brillouin flow cytometry for label-free mechanical phenotyping of the nucleus. *Lab Chip* **17**, 663–670 (2017).
 150. Zhang, J. & Scarcelli, G. Mapping mechanical properties of biological materials via an add-on Brillouin module to confocal microscopes. *Nat. Protoc.* **16**, 1251–1275 (2021).
 151. Barer, R. & Joseph, S. Refractometry of living cells: Part I. Basic principles. *J. Cell Sci.* **3**, 399–423 (1954).
 152. Adair, G. S. & Robinson, M. E. The specific refraction increments of serum-albumin and serum-globulin. *Biochem. J.* **24**, 993 (1930).
 153. Efremov, Y. M., Okajima, T. & Raman, A. Measuring viscoelasticity of soft biological samples using atomic force microscopy. *Soft Matter* **16**, 64–81 (2020).
 154. Nguyen, N., Shao, Y., Wineman, A., Fu, J. & Waas, A. Atomic force

- microscopy indentation and inverse analysis for non-linear viscoelastic identification of breast cancer cells. *Math. Biosci.* **277**, 77–88 (2016).
155. McGrail, D. J., Kieu, Q. M. N. & Dawson, M. R. The malignancy of metastatic ovarian cancer cells is increased on soft matrices through a mechanosensitive Rho–ROCK pathway. *J Cell Sci* **127**, 2621–2626 (2014).
156. Ahmed K., N. & Abubaker and M. Quinn, J. F. Epithelial Mesenchymal Transition and Cancer Stem Cell-Like Phenotypes Facilitate Chemoresistance in Recurrent Ovarian Cancer. *Curr. Cancer Drug Targets* **10**, 268–278 (2010).
157. Engler, A. J., Sen, S., Sweeney, H. L. & Discher, D. E. Matrix elasticity directs stem cell lineage specification. *Cell* **126**, 677–689 (2006).
158. Polacheck, W. J., German, A. E., Mammoto, A., Ingber, D. E. & Kamm, R. D. Mechanotransduction of fluid stresses governs 3D cell migration. *Proc. Natl. Acad. Sci. U. S. A.* **111**, 2447–2452 (2014).
159. McKenzie, A. J. *et al.* The mechanical microenvironment regulates ovarian cancer cell morphology, migration, and spheroid disaggregation. *Sci Rep* **8**, 7228 (2018).
160. Swartz, M. A. *et al.* Tumor Microenvironment Complexity: Emerging Roles in Cancer Therapy. **72**, 2473–2480 (2012).
161. Ingber, D. E. Cellular mechanotransduction: putting all the pieces together again. **20**, 811–827 (2006).
162. Wirtz, D., Konstantopoulos, K. & Searson, P. C. The physics of cancer: the role of physical interactions and mechanical forces in metastasis. *Nat. Rev. Cancer* **11**, 512 (2011).

163. Polacheck, W. J. *et al.* A non-canonical Notch complex regulates adherens junctions and vascular barrier function. *Nature* **552**, 258 (2017).
164. McGrail, D. J. *et al.* Osmotic Regulation Is Required for Cancer Cell Survival under Solid Stress. *Biophys. J.* **TA - TT - 109**, 1334–1337 (2015).
165. Zhou, E. H. *et al.* Universal behavior of the osmotically compressed cell and its analogy to the colloidal glass transition. *PNAS* **106**, 10632–10637 (2009).
166. Guo, M. *et al.* Cell volume change through water efflux impacts cell stiffness and stem cell fate. *PNAS* **114**, E8618-e8627 (2017).
167. Griffith, L. G. & Swartz, M. A. Capturing complex 3D tissue physiology in vitro. *Nat. Rev. Mol. Cell Biol.* **7**, 211 (2006).
168. Baker, B. M. & Chen, C. S. Deconstructing the third dimension – how 3D culture microenvironments alter cellular cues. **125**, 3015–3024 (2012).
169. Schindelin, J. *et al.* Fiji: an open-source platform for biological-image analysis. *Nat. Methods* **9**, 676 (2012).
170. Weiswald, L. B., Bellet, D. & Dangles-Marie, V. Spherical cancer models in tumor biology. *Neoplasia* **17**, 1–15 (2015).
171. Celli, J. P., Rizvi, I., Evans, C. L., Abu-Yousif, A. O. & Hasan, T. Quantitative imaging reveals heterogeneous growth dynamics and treatment-dependent residual tumor distributions in a three-dimensional ovarian cancer model. *J Biomed Opt* **15**, 51603 (2010).
172. Kim, K. S. *et al.* AFM-Detected Apoptotic Changes in Morphology and Biophysical Property Caused by Paclitaxel in Ishikawa and HeLa Cells. *PLoS One* **7**, e30066 (2012).

173. Margueritat, J. *et al.* High-Frequency Mechanical Properties of Tumors Measured by Brillouin Light Scattering. *Phys. Rev. Lett.* **TA - TT - 122**, (2019).
174. Xu, W. *et al.* Cell Stiffness Is a Biomarker of the Metastatic Potential of Ovarian Cancer Cells. *PLoS One* **7**, e46609 (2012).
175. Hyler, A. R. *et al.* Fluid shear stress impacts ovarian cancer cell viability, subcellular organization, and promotes genomic instability. *PLoS One* **13**, e0194170 (2018).
176. Däster, S. *et al.* Induction of hypoxia and necrosis in multicellular tumor spheroids is associated with resistance to chemotherapy treatment. *Oncotarget* **8**, 1725–1736 (2016).
177. Baraniak, P. R. *et al.* Stiffening of human mesenchymal stem cell spheroid microenvironments induced by incorporation of gelatin microparticles. *J Mech Behav Biomed Mater* **11**, 63–71 (2012).
178. Butcher, D. T., Alliston, T. & Weaver, V. M. A tense situation: forcing tumour progression. *Nat Rev Cancer* **9**, 108–122 (2009).
179. Wu, P.-J. *et al.* Water content, not stiffness, dominates Brillouin spectroscopy measurements in hydrated materials. *Nat. Methods* **15**, 561 (2018).
180. Scarcelli, G. & Yun, S. H. Reply to ‘Water content, not stiffness, dominates Brillouin spectroscopy measurements in hydrated materials’. *Nat. Methods* **15**, 561–565 (2018).
181. Kageyama, K., Onoyama, Y., Kogawa, H., Goto, E. & Tanabe, K. The maximum and minimum water content and cell volume of human erythrocytes

- in vitro. *Biophys Chem* **34**, 79–82 (1989).
182. Shen-Gunther, J. & Mannel, R. S. Ascites as a Predictor of Ovarian Malignancy. *Gynecol. Oncol.* **87**, 77–83 (2002).
 183. Lai, I. *et al.* Correlation of differential ascites volume with primary cytoreductive surgery outcome, lymph node involvement, and disease recurrence in advanced ovarian cancer. *Int. J. Gynecol. Cancer* **29**, 922 LP – 928 (2019).
 184. Stukan, M. Drainage of malignant ascites: patient selection and perspectives. *Cancer Manag. Res.* **9**, 115–130 (2017).
 185. Penet, M.-F. *et al.* Ascites Volumes and the Ovarian Cancer Microenvironment . *Frontiers in Oncology* vol. 8 595 (2018).
 186. Ross, G. J. *et al.* Sonographically guided paracentesis for palliation of symptomatic malignant ascites. *Am. J. Roentgenol.* **153**, 1309–1311 (1989).
 187. Zebrowski, B. K. *et al.* Markedly Elevated Levels of Vascular Endothelial Growth Factor in Malignant Ascites. *Ann. Surg. Oncol.* **6**, 373 (1999).
 188. Novak, C., Horst, E. & Mehta, G. Review: Mechanotransduction in ovarian cancer: Shearing into the unknown. *APL Bioeng.* **2**, 31701 (2018).
 189. Ketene, A. N., Schmelz, E. M., Roberts, P. C. & Agah, M. The effects of cancer progression on the viscoelasticity of ovarian cell cytoskeleton structures. *Nanomedicine* **8**, 93–102 (2012).
 190. Swaminathan, V. *et al.* Mechanical stiffness grades metastatic potential in patient tumor cells and in cancer cell lines. *Cancer Res* **71**, 5075–5080 (2011).
 191. Dong, C., Hu, X. & Dinu, C. Z. Current status and perspectives in atomic force

- microscopy-based identification of cellular transformation. *Int J Nanomedicine* **11**, 2107–2118 (2016).
192. Kapoor, A. *et al.* Soft drug-resistant ovarian cancer cells migrate via two distinct mechanisms utilizing myosin II-based contractility. *Biochim. Biophys. Acta - Mol. Cell Res.* **1865**, 392–405 (2018).
193. Avraham-Chakim, L. *et al.* Fluid-flow induced wall shear stress and epithelial ovarian cancer peritoneal spreading. *PLoS One* **8**, e60965–e60965 (2013).
194. Prevedel, R., Diz-Muñoz, A., Ruocco, G. & Antonacci, G. Brillouin microscopy: an emerging tool for mechanobiology. *Nat. Methods* **16**, 969–977 (2019).
195. Jeffrey, B., Udaykumar, H. S. & Schulze, K. S. Flow fields generated by peristaltic reflex in isolated guinea pig ileum: impact of contraction depth and shoulders. *Am. J. Physiol. Liver Physiol.* **285**, G907–G918 (2003).
196. Nikolić, M. & Scarcelli, G. Long-term Brillouin imaging of live cells with reduced absorption-mediated damage at 660 nm wavelength. *Biomed. Opt. Express* **10**, 1567–1580 (2019).
197. Antonacci, G. *et al.* Recent progress and current opinions in Brillouin microscopy for life science applications. *Biophys. Rev.* **12**, 615–624 (2020).
198. Keung, A. J., Kumar, S. & Schaffer, D. V. Presentation counts: microenvironmental regulation of stem cells by biophysical and material cues. *Annu. Rev. Cell Dev. Biol.* **26**, 533–556 (2010).
199. Tzima, E. *et al.* A Mechanosensory Complex That Mediates the Endothelial Cell Response to Fluid Shear Stress. *Nature* **437**, 426–431 (2005).

200. Dangaria, J. H. & Butler, P. J. Macrorheology and adaptive microrheology of endothelial cells subjected to fluid shear stress. *Am. J. Physiol. Cell Physiol.* **293**, C1568–C1575 (2007).
201. Arce, F. T. *et al.* Regulation of the Micromechanical Properties of Pulmonary Endothelium by S1P and Thrombin: Role of Cortactin. *Biophys. J.* **95**, 886–894 (2008).
202. Fels, J., Jeggle, P., Liashkovich, I., Peters, W. & Oberleithner, H. Nanomechanics of vascular endothelium. *Cell Tissue Res.* **355**, 727–737 (2014).
203. Han, Y. L. *et al.* Cell swelling, softening and invasion in a three-dimensional breast cancer model. *Nat. Phys.* (2019) doi:10.1038/s41567-019-0680-8.
204. Scarcelli, G., Kim, P. & Yun, S. H. In vivo measurement of age-related stiffening in the crystalline lens by Brillouin optical microscopy. *Biophys J* **101**, 1539–1545 (2011).
205. Gardel, M. L. *et al.* Elastic Behavior of Cross-Linked and Bundled Actin Networks. *Science (80-.).* **304**, 1301 LP – 1305 (2004).
206. Shao, P. *et al.* Effects of Corneal Hydration on Brillouin Microscopy in Vivo. *Invest. Ophthalmol. Vis. Sci.* **59**, 3020–3027 (2018).
207. Feldman, G. B., Knapp, R. C., Order, S. E. & Hellman, S. The Role of Lymphatic Obstruction in the Formation of Ascites in a Murine Ovarian Carcinoma. *Cancer Res.* **32**, 1663 LP – 1666 (1972).
208. Kipps, E., Tan, D. S. P. P. & Kaye, S. B. Meeting the challenge of ascites in ovarian cancer: New avenues for therapy and research. *Nat. Rev. Cancer* **13**,

- 273–282 (2013).
209. Martin, J. Y., Goff, B. A. & Urban, R. R. Preoperative hyponatremia in women with ovarian cancer: An additional cause for concern? *Gynecol. Oncol.* **142**, 471–476 (2016).
 210. Muhamed, I., Chowdhury, F. & Maruthamuthu, V. Biophysical tools to study cellular mechanotransduction. *Bioengineering* **4**, 12 (2017).
 211. Hassanpour, S. H. & Dehghani, M. Review of cancer from perspective of molecular. *J. Cancer Res. Pract.* **4**, 127–129 (2017).
 212. Iwatsuki, M. *et al.* Epithelial-mesenchymal transition in cancer development and its clinical significance. *Cancer Sci* **101**, 293–299 (2010).
 213. Ingber, D. E. Can cancer be reversed by engineering the tumor microenvironment? *Semin. Cancer Biol.* **18**, 356–364 (2008).
 214. Loret, N., Denys, H., Tummers, P. & Berx, G. The Role of Epithelial-to-Mesenchymal Plasticity in Ovarian Cancer Progression and Therapy Resistance. *Cancers (Basel)*. **11**, 838 (2019).
 215. Loh, C.-Y. *et al.* The E-Cadherin and N-Cadherin Switch in Epithelial-to-Mesenchymal Transition: Signaling, Therapeutic Implications, and Challenges. *Cells* **8**, 1118 (2019).
 216. Lamouille, S., Xu, J. & Derynck, R. Molecular mechanisms of epithelial-mesenchymal transition. *Nat. Rev. Mol. Cell Biol.* **15**, 178–196 (2014).
 217. Grosser, S. *et al.* Cell and Nucleus Shape as an Indicator of Tissue Fluidity in Carcinoma. *Phys. Rev. X* **11**, 11033 (2021).
 218. Meng, W. & Takeichi, M. Adherens junction: molecular architecture and

- regulation. *Cold Spring Harb. Perspect. Biol.* **1**, a002899–a002899 (2009).
219. Klymenko, Y. *et al.* Heterogeneous Cadherin Expression and Multicellular Aggregate Dynamics in Ovarian Cancer Dissemination. *Neoplasia* **19**, 549–563 (2017).
220. Bruner, H. C. & Derksen, P. W. B. Loss of E-Cadherin-Dependent Cell-Cell Adhesion and the Development and Progression of Cancer. *Cold Spring Harb. Perspect. Biol.* **10**, a029330 (2018).
221. Martin, T. A. & Jiang, W. G. Loss of tight junction barrier function and its role in cancer metastasis. *Biochim. Biophys. Acta - Biomembr.* **1788**, 872–891 (2009).
222. de Beco, S., Perney, J.-B., Coscoy, S. & Amblard, F. Mechanosensitive Adaptation of E-Cadherin Turnover across adherens Junctions. *PLoS One* **10**, e0128281 (2015).
223. Fullerton, G. D., Kanal, K. M. & Cameron, I. L. On the osmotically unresponsive water compartment in cells. *Cell Biol. Int.* **30**, 74–77 (2006).
224. Cameron, I. L. & Fullerton, G. D. Lack of appreciation of the role of osmotically unresponsive water in cell volume regulation. *Cell Biol. Int.* **38**, 610–614 (2014).
225. de Beco, S., Gueudry, C., Amblard, F. & Coscoy, S. Endocytosis is required for E-cadherin redistribution at mature adherens junctions. *Proc. Natl. Acad. Sci.* **106**, 7010 LP – 7015 (2009).
226. Indra, I. *et al.* Spatial and temporal organization of cadherin in punctate adherens junctions. *Proc. Natl. Acad. Sci.* **115**, E4406 LP-E4415 (2018).

227. Bordeleau, F. *et al.* Matrix stiffening promotes a tumor vasculature phenotype. *Proc. Natl. Acad. Sci.* **114**, 492–497 (2017).
228. Russell, H. & Pranjol, M. Z. I. Transcription factors controlling E-cadherin down-regulation in ovarian cancer. *Biosci. Horizons Int. J. Student Res.* **11**, (2018).
229. Chen, X., Zhou, C., Yan, C., Ma, J. & Zheng, W. Hyperosmotic stress induces cisplatin sensitivity in ovarian cancer cells by stimulating aquaporin-5 expression. *Exp. Ther. Med.* **10**, 2055–2062 (2015).
230. Zhou, B., Lu, X., Hao, Y. & Yang, P. Real-Time Monitoring of the Regulatory Volume Decrease of Cancer Cells: A Model for the Evaluation of Cell Migration. *Anal. Chem.* **91**, 8078–8084 (2019).
231. Stroka, K. M. *et al.* Water Permeation Drives Tumor Cell Migration in Confined Microenvironments. *Cell* **157**, 611–623 (2014).
232. Gupta, S., McMahon, G. M., Motwani, S. S., Mount, D. B. & Waikar, S. S. ‘Pleurex Desalination’ in Malignancy-related Ascites: A Novel Mechanism of Hyponatremia. *Am. J. Clin. Oncol.* **43**, 14–19 (2020).
233. Yokoyama, Y., Shigeto, T., Futagami, M. & Mizunuma, H. Syndrome of inappropriate secretion of anti-diuretic hormone following carboplatin-paclitaxel administration in a patient with recurrent ovarian cancer. *Eur. J. Gynaecol. Oncol.* **26**, 531–532 (2005).
234. Northcott, J. M., Dean, I. S., Mouw, J. K. & Weaver, V. M. Feeling Stress: The Mechanics of Cancer Progression and Aggression. *Front. cell Dev. Biol.* **6**, 17 (2018).

235. Lin, H.-H. *et al.* Mechanical phenotype of cancer cells: cell softening and loss of stiffness sensing. *Oncotarget* **6**, 20946–20958 (2015).
236. Hida, K., Ohga, N., Kurosu, T., Totsuka, Y. & Shindoh, M. Crosstalk between Blood Vessels and Tumor Microenvironment. *Oral Sci. Int.* **7**, 1–10 (2010).
237. Lintz, M., Muñoz, A. & Reinhart-King, C. A. The mechanics of single cell and collective migration of tumor cells. *J. Biomech. Eng.* **139**, (2017).
238. Guck, J. Some thoughts on the future of cell mechanics. *Biophys. Rev.* **11**, 667–670 (2019).
239. Brehm-Stecher, B. F. Flow Cytometry. in (eds. Batt, C. A. & Tortorello, M. L. B. T.-E. of F. M. (Second E.) 943–953 (Academic Press, 2014).
doi:<https://doi.org/10.1016/B978-0-12-384730-0.00127-0>.
240. Wyss, H. M. Cell Mechanics: Combining Speed with Precision. *Biophys. J.* **109**, 1997–1998 (2015).